

ALMA MATER STUDIORUM
UNIVERSITÀ DI BOLOGNA

SCUOLA DI SCIENZE
Dipartimento di Fisica e Astronomia
Corso di Laurea Magistrale in Fisica

**Studies of performance of pixel detectors
in BCD8 and TowerJazz technologies for
the ATLAS experiment at HL-LHC**

Relatore:
Chiar.mo Prof.
Antonio Zoccoli

Presentata da:
Marco Dalla

Correlatore:
Dott.ssa Carla Sbarra

Anno Accademico 2017 / 2018

Abstract

Durante i prossimi 5 anni il Large Hadron Collider (LHC) verrà aggiornato nell'High Luminosity LHC, il quale, secondo i piani odierni, inizierà a funzionare nel 2026 con una luminosità istantanea di circa cinque volte quella odierna, e una luminosità integrata aumentata di circa 10 ordini di grandezza. Per questo motivo è necessario un aggiornamento di tutti i rivelatori e i loro sistemi di acquisizione per far fronte al maggiore flusso di particelle ionizzanti e all'incremento di dati acquisiti.

In particolare l'Inner Detector di ATLAS verrà completamente ridisegnato e sono in corso numerosi studi per identificare le migliori tecnologie adatte a questo aggiornamento. In questo momento lo stato dell'arte dei rivelatori di tracciamento è composto da soluzioni ibride, che consistono in un sensore e in un dispositivo di lettura uniti insieme attraverso un processo dispendioso sia in termini di tempo che di costi, chiamato "bump-bonding".

Due tecnologie che hanno come obiettivo il superamento del modello ibrido sono BCD8 e TowerJazz, con le quali sia il sensore che il dispositivo di lettura sono integrati nel medesimo substrato di silicio. Queste soluzioni sono particolarmente adatte per lo strato più esterno del tracciatore di ATLAS, in quanto questo copre una superficie estremamente elevata, tuttavia non è stata ancora dimostrata la resistenza a radiazione ionizzante di queste tecnologie.

La tecnologia BCD8 consiste in una soluzione chiamata a "pixel

attivo”, in cui parte dell’elettronica di lettura di tipo CMOS, che solitamente funziona a basse tensioni, è integrata in un substrato di tipo DMOS che supporta alte tensioni. La tecnologia TowerJazz invece è già stata usata per produrre sensori monolitici di tipo CMOS per l’esperimento ALICE.

In questa tesi sono presentate le misure che ho personalmente effettuato su dei prototipi costruiti con queste tecnologie. Per il prototipo BCD8, chiamato KC53AB, ho misurato i parametri di corrente di buio e capacità su dei pixel passivi, in chip nuovi e irraggiati con dosi simili a quelle che avrebbero ricevuto durante il periodo di funzionamento di HL-LHC. Per il prototipo TowerJazz, chiamato Investigator, ho effettuato, al fascio di test del CERN, degli studi in termini di efficienza di rivelazione e tempo di raccolta delle cariche, su chip nuovi e irraggiati.

Questi studi permettono di verificare la fattibilità e l’affidabilità di queste tecnologie in ambiti di esperimenti che richiedono il tracciamento di particelle cariche in condizioni di alte dosi di radiazioni, come HL-LHC.

Abstract

In the next 5 years a substantial upgrade of the Large Hadron Collider (LHC) is scheduled: the High Luminosity LHC will start colliding beams around 2026 with an instantaneous luminosity five times larger than the current one, while the total integrated luminosity will exceed the previous one by one order of magnitude. Moreover, at the end of the current program the experiments at the LHC will be running with components which are 15-20 years old. As a consequence all detectors, as well as their data acquisition systems, must be upgraded too, so as to handle the increased flux of ionising particles and the larger data volume.

The Inner Detector of the ATLAS experiment, in particular, is being completely redesigned and several studies are in progress to identify the best technological solution for its upgrade. State-of-the-art trackers at hadron colliders rest on hybrid-module semiconductor solutions, where a sensor and a complex readout chip are located in two separated devices that are independently optimised. These two separated devices are then joined together by an extremely expensive and time-consuming process known as bump-bonding.

BCD8 and TowerJazz are among the technologies that are currently investigated to replace the hybrid solution with a monolithic one, where both the sensor and the readout electronics are built on the same substrate. This solution is particularly appealing for the outermost layer of the ATLAS tracker barrel, which is the larger-area one, but its ra-

diation hardness has yet to be proved.

The BCD8 technology is an active pixel solution, where the low voltage CMOS electronics is integrated in a DMOS structure that can support high voltages. TowerJazz is a high-voltage CMOS technology that has been used in the development of monolithic CMOS sensors for the ALICE experiment.

This thesis presents the results of measurements I performed on prototypes of both technologies. For the BCD8 prototype, called KC53A, dark current and capacitance studies of passive pixels have been carried out before and after irradiation campaigns mimicking the dose expected at HL-LHC. For the TowerJazz prototype, called Investigator, detailed characterisation of chip performance in terms of detector efficiency and timing of charge collection have been performed at a beam-test facility at CERN, both on new and radiation-aged devices.

These studies allowed to assess the suitability and reliability of the corresponding technologies for HL-LHC and, in general, for any other application requiring a large area pixel detector in presence of considerable radiation levels.

Contents

1	The Large Hadron Collider	7
1.1	Design parameters, structure and performance	7
1.2	Physics Goals	12
1.3	LHC upgrade: HL-LHC	12
2	The ATLAS Experiment	17
2.1	The ATLAS Detector	17
2.1.1	The Calorimeter System	18
2.1.2	The Muon Spectrometer	20
2.1.3	The Inner Detector	21
2.2	The Forward Detectors	24
2.3	The Trigger and Data Acquisition	24
2.4	The ATLAS Detector Upgrade	26
3	Semiconductor Detectors	29
3.1	PN-Junction	29
3.1.1	Depletion region	31
3.1.2	Reverse current	32
3.1.3	Capacitance	32
3.2	Silicon detectors	32
3.2.1	From space point to tracks	35
3.2.2	Radiation damage on silicon detectors	36
3.3	Hybrid and monolithic silicon detectors	39

4	The ATLAS Inner Tracker	43
4.1	Detector layout	43
4.2	Detector specifications	46
4.3	Pixel Modules for ITk	49
4.3.1	Front End Chip	49
4.3.2	Pixel Sensor Technologies	50
5	BCD8 and TowerJazz Technologies	55
5.1	BCD8 Technology	55
5.1.1	The KC53AB prototype	57
5.2	The TowerJazz Technology	59
5.2.1	TowerJazz Investigator	63
6	Tests on KC53AB passive pixels	65
6.1	Current as a function of voltage	65
6.2	Capacitance as a function voltage	68
6.3	Studies on radiation resistance	72
7	Tests on TowerJazz Investigator	79
7.1	Beam test setup	79
7.1.1	Telescope and DUT setup	80
7.2	Data reconstruction	85
7.2.1	Beam track reconstruction in the telescope	85
7.2.2	Signal reconstruction on the DUT	87
7.3	Data analysis and result	89
7.3.1	Cluster and charge	89
7.3.2	Signal rise time	95
7.3.3	Efficiency measurements	96
7.4	Measurements with radioactive sources	104
7.4.1	^{55}Fe source: charge calibration	104
7.4.2	^{90}Sr source	105
8	Conclusions	107

Chapter 1

The Large Hadron Collider

The Large Hadron Collider, [7] installed at the Conseil Européen pour la Recherche Nucléaire (CERN) laboratory nearby Geneva, is a circular accelerator which provides proton and heavy ion collisions up to center-of-mass energies $\sqrt{s} = 13$ TeV and $\sqrt{s} = 5.02$ TeV, respectively, with instantaneous luminosities greater than 10^{34} cm⁻²s⁻¹ in pp collisions. LHC started operation in November 2009 with a beam energy of 1.18 TeV and will end its first running phase in 2023. It has a circumference of 27 km and features 1232 superconducting dipole and 392 quadrupole, cooled down to 1.9 K by liquid helium. The dipoles generate a field of 8.3 T to keep the beam onto a circular trajectory, the quadrupoles a field of 6.8 T to focus it.

1.1 Design parameters, structure and performance

The design parameters of LHC are briefly summarised in table 1.1. The final kinetic energy is obtained with a chain of machines that accelerate particles to higher energies step by step, as shown in fig. 1.1. Primary protons are extracted from hydrogen gas using an electric field and injected into the Linac 2 linear accelerator, where they reach 50 MeV; the beam is then accumulated into the Proton Synchrotron Booster (PSB), a circular accelerator where the particle energy is risen to 1.4 GeV. It is here that the protons are packed in bunches, that are

Parameters	Value
Beam Energy [TeV]	6.5
Centre of Mass Energy [TeV]	13
Number of dipole magnets	1232
Dipole magnets field [T]	8.3
Number of quadrupole magnets	392
Quadrupole magnets field [T]	6.8
Magnet Temperature [K]	1.9
Peak Luminosity [$\text{cm}^{-2}\text{s}^{-1}$]	10^{34}
Proton per bunch	$1.05 \cdot 10^{11}$
Bunch Spacing	24.95

Table 1.1: LHC nominal parameters.

then injected into the Proton Synchrotron (PS) where they reach 25 GeV. They are then sent into the Super Proton Synchrotron (SPS) where they reach 450 GeV and finally injected into LHC, the last element of the chain. There, the two beams are accelerated in different pipes in opposite directions up to the energy of 6.5 TeV. The interaction points, where the two beam pipes merge into one, correspond to the positions of four detectors: ATLAS, CMS, LHCb and ALICE. ATLAS (A Toroidal Apparatus) and CMS (Compact Muon Solenoid) are two general purpose experiments. LHCb and ALICE (A Large Ion Collider Experiment) are focused on measurements of CP violation in rare phenomena involving hadrons containing the bottom quark, and the study of quark-gluon plasma predicted by Quantum Chromodynamics in heavy ion collisions, respectively.

An important parameter of any accelerator is its instantaneous luminosity \mathcal{L} , which relates the rate R_{event} of production of events of any process to its cross section σ_{event} :

$$R_{event} = \sigma_{event} \mathcal{L} \quad (1.1)$$

The cross section is specific to each process and is proportional to the probability that its final state is going to appear. It is measured in barn and is a function

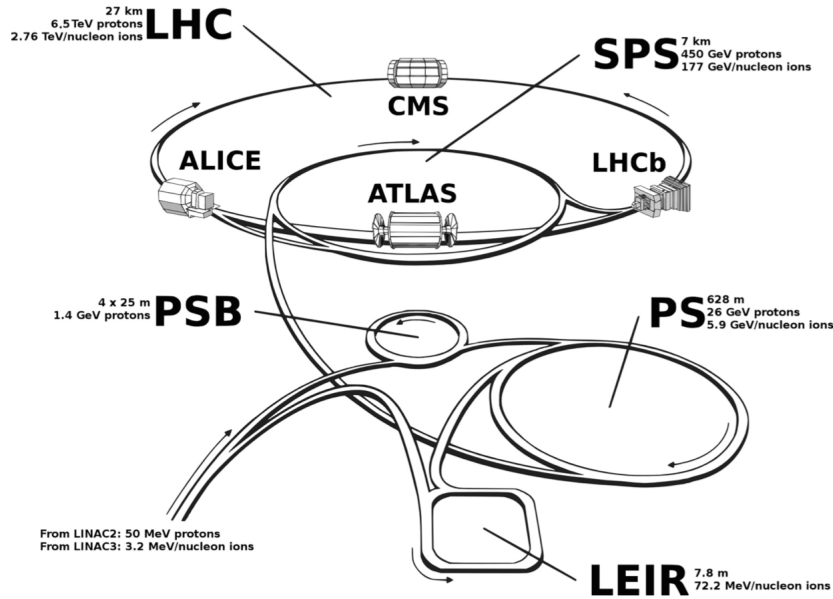


Figure 1.1: Schematics of the acceleration chain of LHC.

of energy: when energy increases, new phenomena may appear and even become dominant and, at the same time, others may be suppressed. Higher luminosity means larger amount of events: this is very important to study rare processes.

A peculiarity of LHC is that there is typically more than one proton-proton (pp) interaction taking place during every bunch crossing. Such number of interactions is known as pile-up (μ). The instantaneous luminosity can also be expressed as a function of the μ parameter, assuming it is the same for all bunch crossing, one can write

$$\mathcal{L} = \frac{\mu \cdot N_b \cdot f}{\sigma_{tot}} \quad (1.2)$$

with f the orbit frequency, N_b the number of bunches per beam and σ the total pp cross section.

In 2011 there were at most 20 pp-interactions per bunch crossing, then this number doubled in 2012 and again in LHC Run 2, where a detector-limited average μ of approximately 55 has been reached. This is shown in the second peak of fig. 1.2. During collisions, the instantaneous luminosity decreases until the beam are dumped.

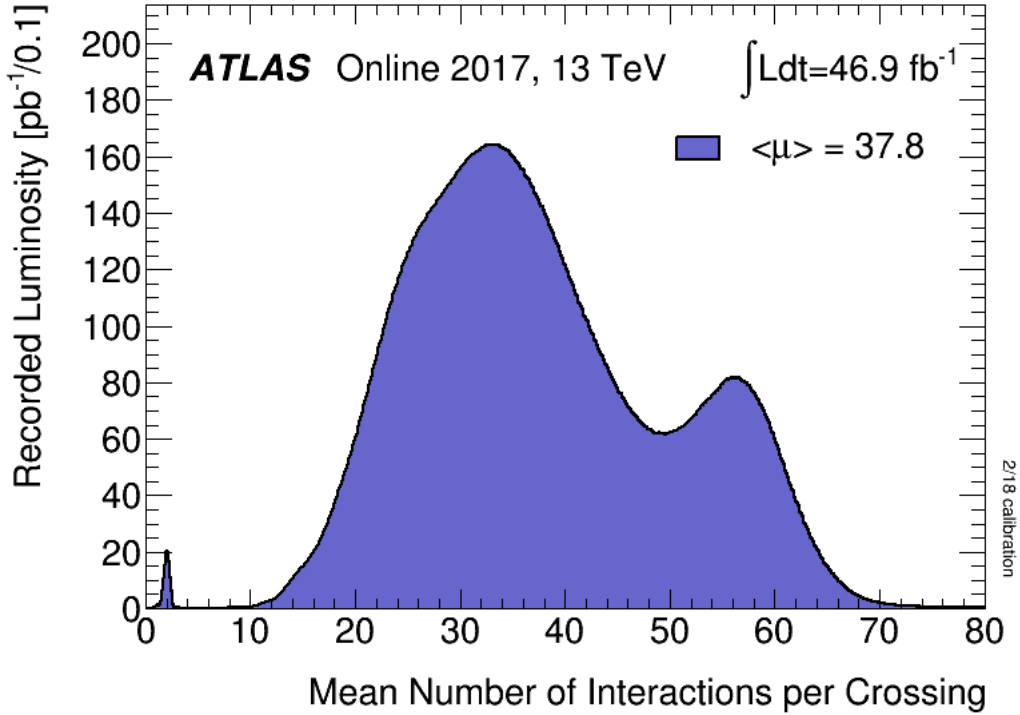


Figure 1.2: Luminosity-weighted distribution of the mean number of interactions per crossing for the 2017 pp collision data at 13 TeV centre-of-mass energy

The instantaneous luminosity can also be defined using the beam parameters. For a gaussian beam distribution it can be expressed as:

$$\mathcal{L} = \frac{f N_p^2 N_b \gamma_r}{4\pi \epsilon_n \beta^*} F \quad (1.3)$$

with f the orbit frequency, N_p the number of protons per bunch, N_b the number of bunches per beam, γ_r a relativistic correction and ϵ_n and β^* parameters that describe the size of the beam at the interaction point. The former, called normalised transverse beam emittance, depends on the preparation of the bunches (a low beam emittance means particles confined in a small distance with nearly the same momentum), while the latter, called amplitude function at beam point, is the distance after which the beam size is doubled and is determined by the accelerator magnet configuration at the interaction point. F is a geometric luminosity reduction factor which depends on the beam crossing angle and the bunch length.

As illustrated in fig. 1.3, the time-integrated Luminosity ($L = \int \mathcal{L}(t)dt$) delivered by LHC to the ATLAS experiment up to the end of 2017 is 92.9 fb⁻¹. The total luminosity expected by the end of Run 3 (2021-2023) is 300 fb⁻¹.

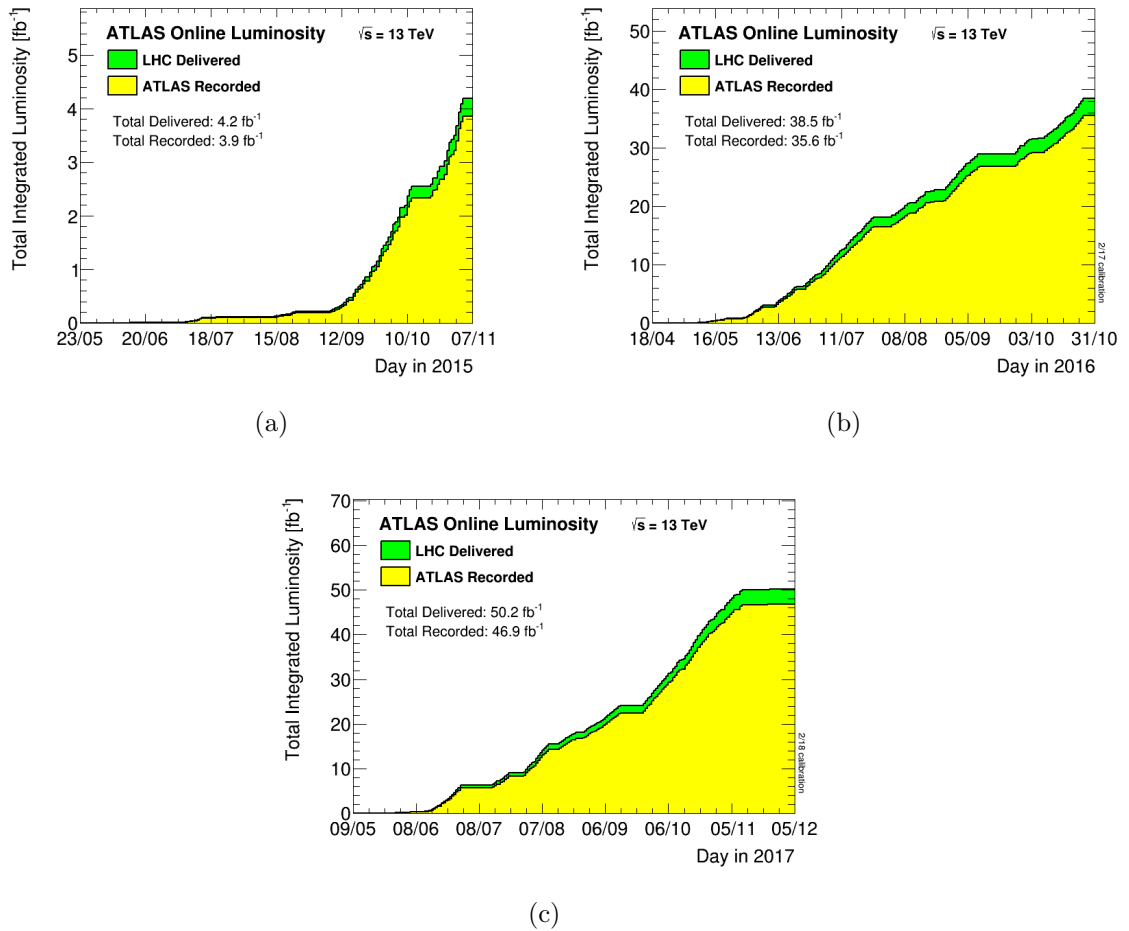


Figure 1.3: Cumulative luminosity versus time delivered to (green) and recorded by ATLAS (yellow) during stable beams for pp collisions at 13 TeV centre-of-mass energy in (a) 2015, (b) 2016, (c) 2017

1.2 Physics Goals

The main purpose of the experiments at the LHC is overtaking the limits of the standard model of elementary particles and their interactions. The fundamental discovery of the Higgs Boson ($m = 124.98 \pm 0.98 \text{ GeV}/c^2$) took place in 2012, and is currently deepened with the careful study of its decays and couplings. Another particle that may yield hints on new physics is the quark top: its large mass ($m = 172.44 \pm 0.60 \text{ GeV}/c^2$) implies a large energy must be available for its production, and this makes the LHC the ideal place for its study. In general hadron colliders allow to reach for the highest centre of mass energies and are thus used to open new energy frontiers, at variance with electron-positron colliders which are more suitable for precision studies of known processes.

The cross sections of the main processes occurring at LHC is shown in fig. 1.4. The total cross section is approximately 100 mb, while the most “interesting” ones have cross sections that are several orders of magnitude smaller. The largest part of pp interactions produce low-transverse-momentum particles, whereas the “interesting” processes involve hard interactions between proton constituents, e.g. quark and gluons. These interactions are characterised by jets and/or leptons of high transverse momentum, and can therefore be separated from the rest.

1.3 LHC upgrade: HL-LHC

In the next years LHC will be subjected to a series of upgrades aimed at increasing its design luminosity by a factor 5 (up to $5 \cdot 10^{34} \text{ cm}^{-2}\text{s}^{-1}$) and transforming the machine into the High-Luminosity LHC (HL-LHC) [4]. Schedule details are shown in fig. 1.5.

A higher luminosity corresponds to an extension of the energy scale that can be explored, and thus a better study of the ElectroWeak Symmetry Breaking (EWSB) mechanism, as well as more extensive searches for signatures of new physics at high energies: from Super SYmmetry (SUSY) models to models of extra dimensions.

With the larger data sample stemming from the increased rate of collisions, the precision of the measurements of the Higgs Boson properties will also improve:

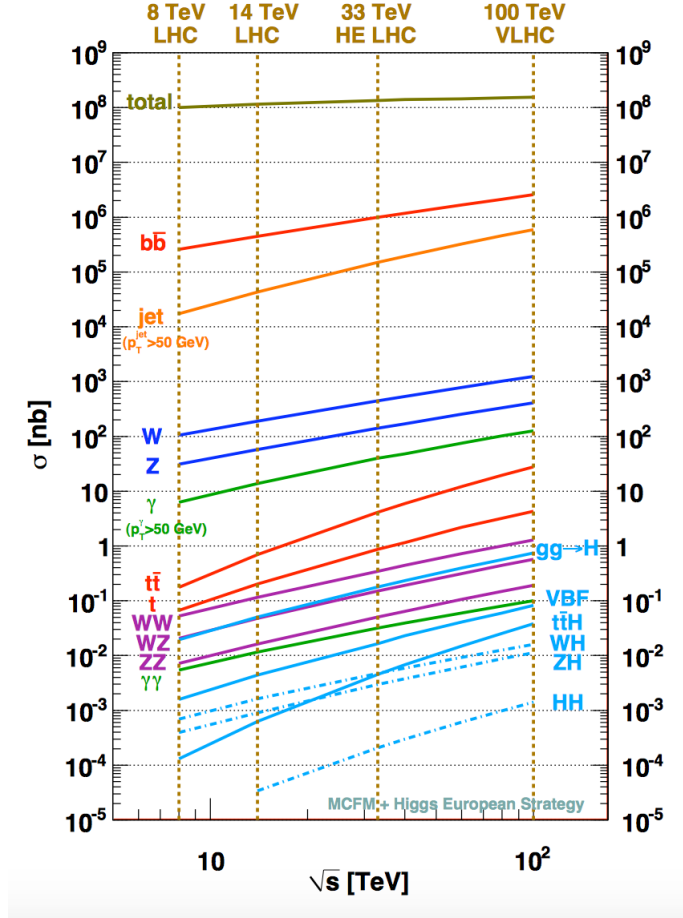


Figure 1.4: pp cross sections at energies around the one of LHC

the knowledge of its coupling with bosons and fermions and its rare decays and self-coupling (e.g. $HH \rightarrow \tau\tau bb$) is expected to reach precisions of 5% and 30% respectively.

The goal of the HL-LHC project is to increase the 14 TeV dataset from about 300 fb^{-1} , expected by the end of LHC run3 (2023) to 3000 fb^{-1} by 2035. The HL-LHC will begin collisions around 2026 and will deliver an additional 2500 fb^{-1} to LHC experiments over ten years. This increase in the luminosity is way beyond the design parameters with which LHC and its experiments were built. Therefore a significant upgrade of the detectors is also due.

HL-LHC will produce a number of pp interactions in each bunch crossing that

HL-LHC Parameters	Value
Beam energy in collision [TeV]	7
Particles per bunch, N [10^{11}]	2.2
Number of bunches per beam	2750
Virtual luminosity [$\text{cm}^{-2}\text{s}^{-1}$]	$2.4 \cdot 10^{34}$
Levelled luminosity [$\text{cm}^{-2}\text{s}^{-1}$]	$5 \cdot 10^{34}$
Levelled <pile-up>	140

Table 1.2: HL-LHC nominal parameters

is 10 times the current amount, with and expected maximum pile-up $\mu \approx 200$. Therefore the granularity of many of the detectors will have to be increased to cope with larger occupancies, and the detectors themselves will need to be able to withstand larger particle fluences and still work in a much harder environment as far as the radiation damage is pertained. In order to face this challenge, several R&D programs have started to study the characteristics of new detectors and the most suitable technologies to be implemented. Table 1.2 summarises the HL-LHC nominal parameters; however, to be safe, guideline parameters for detector R&D predict a maximum instantaneous luminosity of $7 \cdot 10^{34} \text{ cm}^{-2}\text{s}^{-1}$, a pile-up of $\mu \approx 200$ and an integrated luminosity of 3000 fb^{-1} over ten years.

As shown in fig. 1.5 the upgrade of LHC is planned in three phases that will happen during three machine shutdowns. The first phase happened during the 2013-2014 shutdown. The aim was to drive the machine to the nominal luminosity of $10^{34} \text{ cm}^{-2}\text{s}^{-1}$, which has been reached and surpassed ($1.5 \cdot 10^{34} \text{ cm}^{-2}\text{s}^{-1}$). The second long shutdown of LHC will happen in 2019. The purposed upgrades of LHC will be the improvement of LINAC2 and the increase of the the Proton Synchrotron Booster output energy. LHC will restart in 2021 with a luminosity of $2 \cdot 10^{34} \text{ cm}^{-2}\text{s}^{-1}$. The final shutdown is scheduled for 2024 to 2026. During this period, LHC with be upgraded with new inner triplets and crab cavities. The target instantaneous luminosity of $5 \cdot 10^{34} \text{ cm}^{-2}\text{s}^{-1}$ is expected to be reached. As previously mentioned the purpose of the upgrade is to accumulate 3000 fb^{-1} of

data by around 2035.

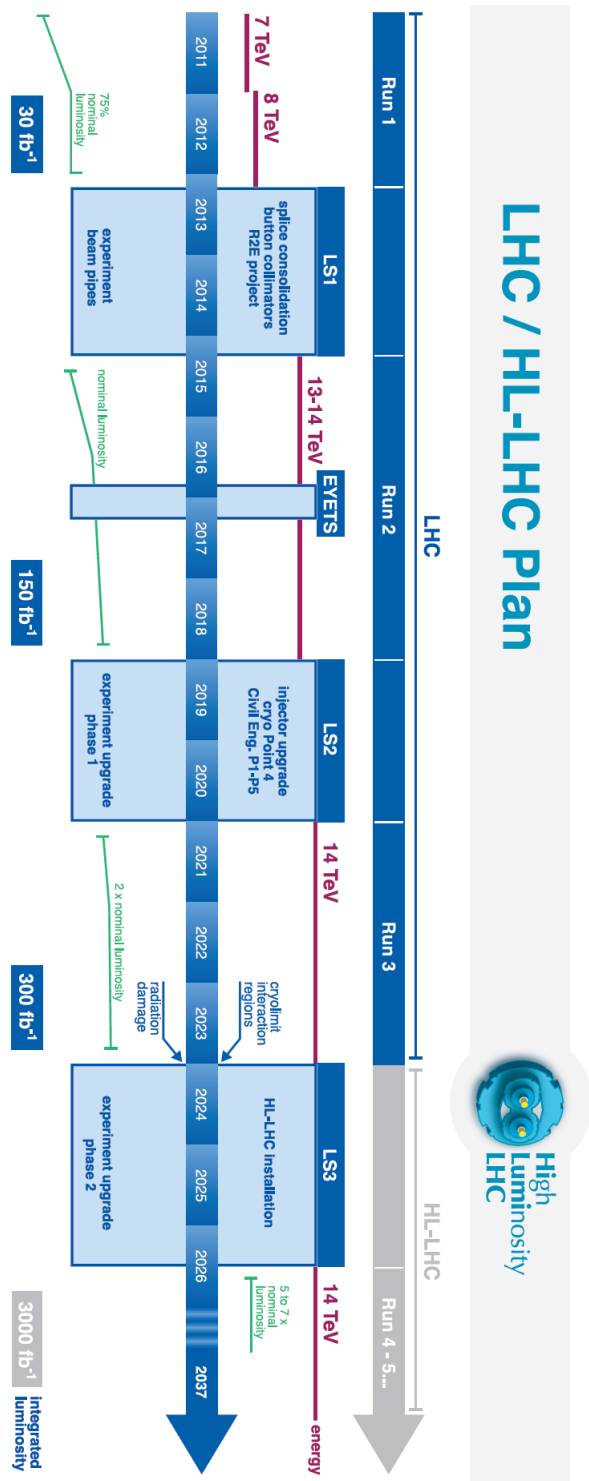


Figure 1.5: LHC and HL-LHC luminosity and energy schedule.

Chapter 2

The ATLAS Experiment

In this chapter the ATLAS [10] experiment and its main components are presented, focusing in particular on the sub-detectors that are relevant to my work. In addition, the main proposed modification to the ATLAS detector connected to the High Luminosity LHC upgrade are briefly introduced.

2.1 The ATLAS Detector

A representation of the ATLAS Detector [2] can be seen in fig. 2.1. It surrounds the proton-proton interaction point and has a cylindrical shape. This is necessary in order to cover the largest fraction of solid angle around the interaction point, thus capturing the largest amount of particles produced at the collision, or, in other words, to maximise the detector acceptance. The detector is 46 meters long, has a diameter of 25 meters and weighs 7000 tonnes. It is made of several different sub-detectors, all disposed concentrically around the cylinder axis. Each detector is designed for a specific purpose and its design has been optimised using specific benchmark measurements. Other characteristics that were taken into consideration are radiation hardness and performance stability.

Near the beam line the innermost sub-system is found: the inner tracker, which is immersed in a solenoidal magnetic field. Its purpose is to reconstruct the trajectory and measure the transverse momentum p_T of charged particles. Then there

Detector	Resolution	η coverage
Inner Tracker	$\sigma_{p_T}/p_T = 0.05\%p_T \oplus 1\%$	± 2.5
Electromagnetic Calorimeter	$\sigma_E/E = 10\%/\sqrt{E} \oplus 0.7\%$	± 3.2
Central Hadronic Calorimeter	$\sigma_E/E = 50\%/\sqrt{E} \oplus 3\%$	± 3.2
Forward Hadronic Calorimeter	$\sigma_E/E = 50\%/\sqrt{E} \oplus 10\%$	$3.1 < \eta < 4.9$
Muon System	$\sigma_{p_T}/p_T = 10\%$ at $p_T = 1TeV$	± 2.7

Table 2.1: Main goal performances of the sub-detectors in the ATLAS detector

is an electromagnetic calorimeter to absorb and measure the energy E of photons and electrons. It is surrounded by the hadronic calorimeter, which absorbs and measure the energy E of hadrons. Finally the chambers dedicated to the detection of muons, the only kind of primary particles able to escape the previous detectors, are found. The muon system is immersed in a toroidal magnetic field, which gives the name to ATLAS, allowing the measurement of the muon transverse momentum p_T . Near the beam line, located at 2 and 17 m on either side of the main ATLAS detector, the forward detectors are found: BCM and LUCID, whose main purposes are to protect the inner detector from excess radiation by issuing beam abort and measure luminosity, respectively.

The goal performances of ATLAS sub-detectors can be seen in the table 2.1. The pseudorapidity η is dened as: $\eta = -\ln[\tan(\theta/2)]$, with θ the polar angle with respect to the beam line. Pseudo-rapidity is a parameter commonly used due to the fact that only depends on the polar angle of the particles trajectory and not on the energy of the particle.

2.1.1 The Calorimeter System

The ATLAS calorimeter system covers a region of pseudorapidity $|\eta| < 4.9$ and has a complete symmetry around the beam axis in order to have a good missing transverse energy (E_T^{miss}) measurement. As mentioned before, it is composed of two parts: the electromagnetic calorimeter and the hadronic calorimeter. Both

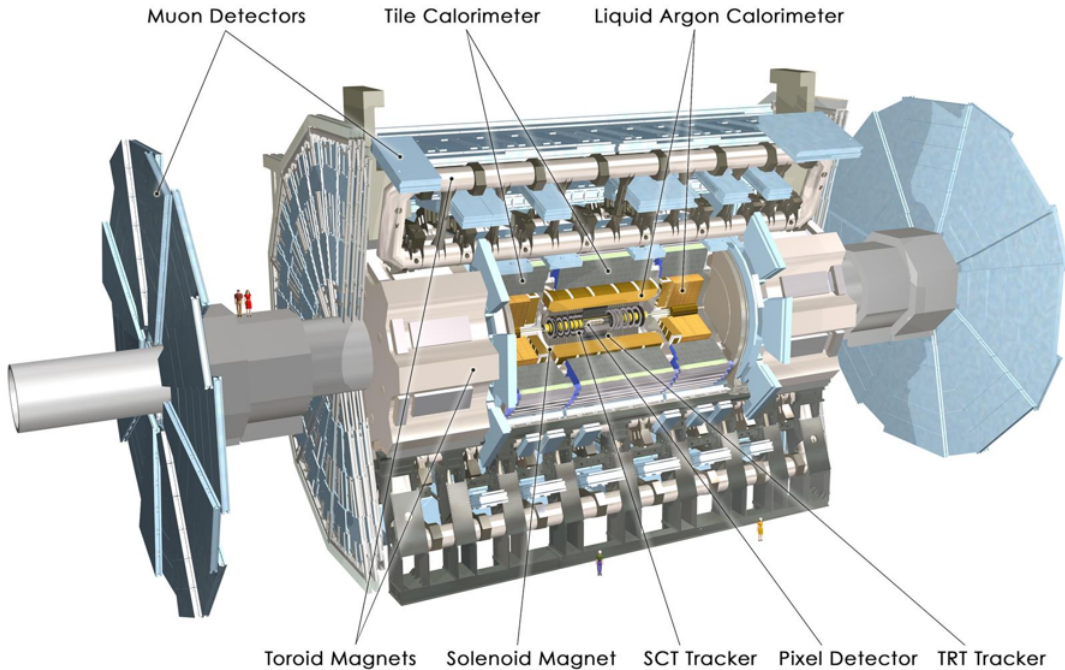


Figure 2.1: Schematics of the ATLAS experiment

are sampling detectors.

The electromagnetic calorimeter (EM) is made of steel cladded lead absorbers and liquid argon, with a structure of an accordion sunken in liquid argon. It is composed of a barrel and two end-caps with a total thickness of 22 radiation lengths (X_0) in the barrel part and more than 24 X_0 in the end-caps.

The hadronic calorimeter is composed by the following parts: the Tile Calorimeter (TileCal), the Hadronic End-cap Calorimeter (HEC) and the Forward Calorimeter (FCal). The TileCal is placed around the EM calorimeter envelopes and is made of steel plates as absorbers, and plastic scintillating tiles as active materials. The HEC consists of two independent wheels per end-cap, located behind the end-cap electromagnetic calorimeter. The FCal is another sampling calorimeter made of copper and tungsten as absorbers and liquid argon as active material. It is integrated into the end-cap cryostats.

The energy resolutions are different depending on the calorimeter and are summarised in table 2.1. A scheme of the calorimeter system is shown in fig. 2.2.

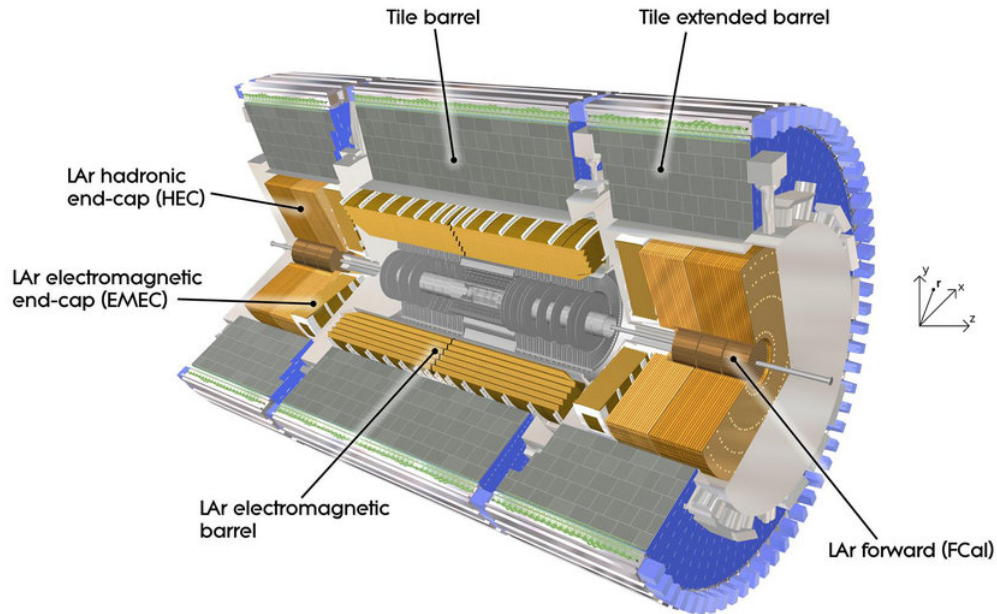


Figure 2.2: ATLAS Calorimeter

2.1.2 The Muon Spectrometer

The muon spectrometer is structured in a barrel plus two end-caps, each within a toroidal magnet, and is divided in four parts: two precision tracking detectors and two triggering chambers, each one using a different technology. They are:

- Monitor Drift Tubes(MDT): to measure the muon trajectory and momentum in the barrel and end-cap regions;
- Cathode Strip Chambers: with the same purpose as the MDT in the innermost layer of the end-cap;
- Resistive Plate Chambers to provide muon trigger in the barrel region;
- Thing Gap Chambers to provide muon trigger in the end-cap region.

The whole system covers pseudorapidity of $|\eta| < 2.7$ and can measure transverse momentum $p_T > 3$ GeV. The p_T resolution is 10% for $p_T = 1$ TeV and the

energy upper limit for momentum measurements is 3 TeV. A picture of the Muon Spectrometer is shown in fig. 2.3.

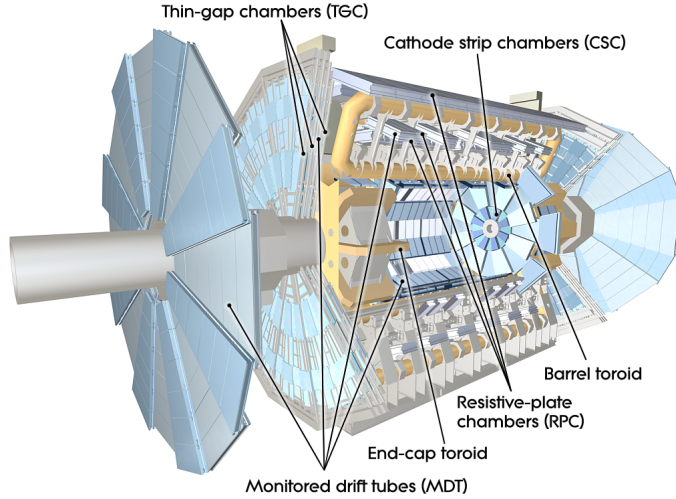


Figure 2.3: ATLAS Muon Spectrometer

2.1.3 The Inner Detector

The Inner Detector (ID) is the precision tracker of ATLAS. It is a 6.2 m long cylinder with a radius of 1.15 m. A picture of its layout is shown in fig. 2.5. As mentioned before, the main task of the ID is to reconstruct the trajectories of charged particles through the measurement of space points along their path. Being immersed in a solenoidal magnetic field, it allows the evaluation of charged particles momentum and the reconstruction of the primary interaction vertices as well as secondary vertices from decays of particles with short lifetime (hadrons containing quarks b and c, τ leptons, etc.). The Inner Detector covers a pseudorapidity range up to $|\eta| < 2.5$. Since it is the closest detector to the beam, it receives the greatest part of the radiation originating from the collision, and its materials must be as radiation hard as possible. It also has the finest granularity, and has to be made of as little material as possible to minimise multiple scattering. The Inner Detector is composed of the following parts:

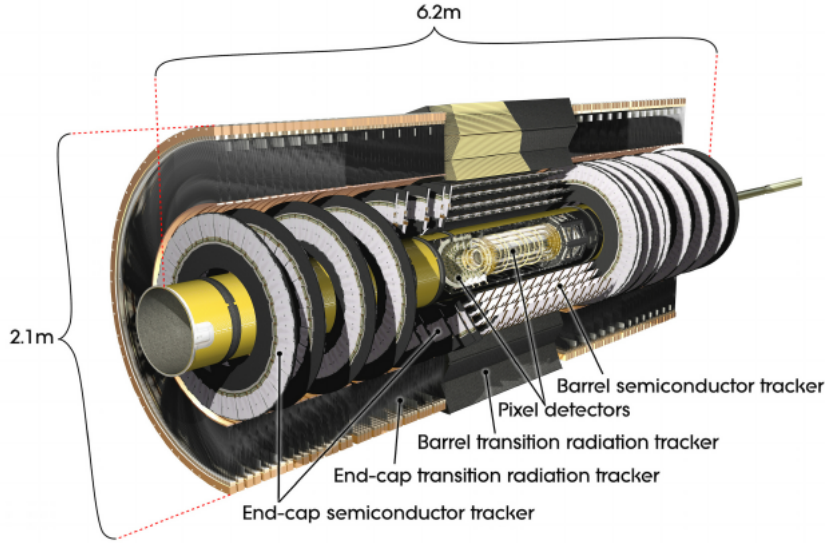


Figure 2.4: ATLAS Inner Detector

- Pixel detector: it is the closest to the beam pipe. It is a silicon-based detector with the highest granularity in ATLAS: it contains a total of 140 million pixels, each of dimension $50 \times 400 \mu\text{m}^2$, distributed over three barrels at the average radii of 4, 10 and 13 cm and five disks with radius between 11 and 20 cm, which complete the angular coverage. Each layer has a thickness of about 1.7% of a radiation length at normal incidence. This apparatus is able to measure the trajectories of charged particles, or tracks, for $p_T > 500\text{MeV}$. During the long shutdown which started in 2013 another layer, called Insertable B-Layer (IBL), was added in the innermost region. The IBL consists of a unique layer of pixel modules forming a cylindrical detector of radius 3.325 cm and pseudorapidity coverage $|\eta| < 2.58$. It features planar pixels of pitch $50 \times 250 \mu\text{m}^2$ in the barrel and 3D pixels at the edges. Details of these technologies are provided in chapter 4. The addition of the IBL improved the resolution on the track impact parameter by about 40% for tracks with $p_T > 1 \text{ GeV}$, thus improving b-tagging performance.
- SemiConductor Tracker: it is made of 8-layers of silicon microstrip detectors. Each silicon detector is $6.36 \times 6.60 \text{ cm}^2$ with 768 strips of $80 \mu\text{m}$ pitch. Each

module consists of four single-sided silicon detectors. On each side of the module, two detectors are wire-bonded together to form 12.8 cm long strips. Two of these structures are then glued together back to back with an angle of 40 mrad between each other. This structure provides precise position measurements in the z (parallel to the beam line) and ϕ (azimuthal) coordinates. In the barrel region the plane of the microstrip detector is parallel to the beam line, while in the end-cap region it is perpendicular.

- Transition Radiation Detector: it is the largest one and surrounds the other two. It consists of a large number ($\approx 5 \cdot 10^4$), of straw tubes, i.e. cylindrical tubes with a positive wire on the axis and the internal wall at negative voltage. The straws all together contribute to the measurement of the particle momentum thanks to the high number of space points they can measure. Each one is filled with a mixture of Xenon (70 %), CO_2 (27 %), and O_2 (3 %). In the barrel region the tubes are parallel to the beam line, while in the end-cap region are perpendicular. The TRT helps electron identification since these particles are the only ones that also produce radiation transition when traversing the detector material layers.

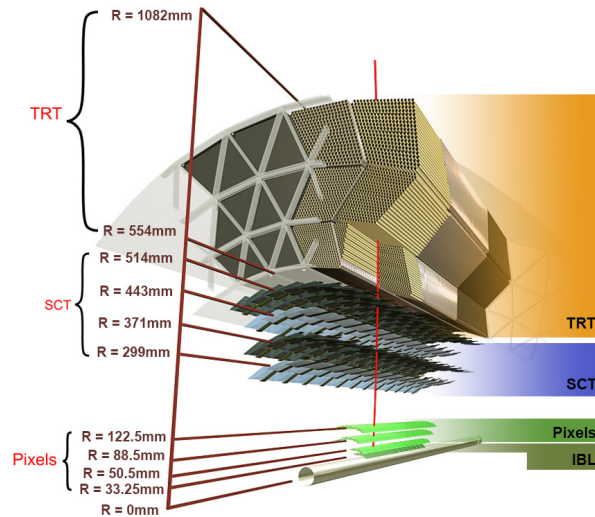


Figure 2.5: Scheme of the Inner Detector

2.2 The Forward Detectors

The BCM detector (Beam Condition Monitor) is composed of two set of four diamond sensors situated at 2 m from the interaction point and less than 6 cm radially from the beam pipe. It protects the inner system by issuing beam abort in case of losses and provides.

The LUCID detector (LUminosity Cherenkov Integrating Detector) is made of two modules, each fit with 16 photomultipliers, placed at 17 m from the interaction point around the beam-pipe on both forward ends of ATLAS. It is dedicated to monitoring and measuring luminosity both online and offline. Online luminosity is needed for beam optimisation and levelling, while the offline one is needed to measure the cross section of any observed process and put limits on hypothetical ones.

2.3 The Trigger and Data Acquisition

The ATLAS Trigger and Data AcQuisition (TDAQ) is a system created for the selection and storage of interesting events. It is made of three separate levels: level 1 trigger (LVL1), level 2 trigger (LVL2) and Event Filter (EF). For each level a finer selection is made through the application of particular selection criteria.

The trigger system must adapt the LHC proton-proton interaction rate of 40 MHz to a few hundred of Hz, which is the rate of events that ATLAS can handle. Therefore, the trigger system provides a reduction factor of 10^6 . The trigger system must make the selection between high p_T interesting events and minimum bias pp interactions with a high efficiency in a very short time.

The input frequency of LVL1 trigger is the same of the bunch crossing rate of 40 MHz (the bunch spacing is 25 ns). The selection algorithms use information about muon p_T muons, electrons, photons and jets energy as well as missing transverse energy. The decision is made in less than $2.5 \mu\text{s}$. After, the LVL1 the data rate is reduced to approximately 75 kHz.

In each event, the LVL1 trigger also defines one or more Region-of-Interest

(RoI), e.g. the coordinates η and ϕ of the regions which triggered the event. The RoI data include information on the identified type of feature and the passed criteria.

Then the selection goes through the LVL2 trigger which further discriminates events with information from the calorimeter and the inner detector. This level takes decisions in about ≈ 40 ns and in this case the latency, variable from event to event, ranges between 1 ns and 10 ns. The output rate of LVL2 trigger is about 3.5 kHz. After LVL2 and before event storage, a final selection is performed in the EF. All algorithms are executed offline. The EF, a farm of processors for parallel data reduction, takes information from all ATLAS detectors to create raw-data to be stored at a frequency of a few 100 Hz. The average event processing time of the EF is of the order of 4 s.

The scheme of the TDAQ is seen in fig. 2.6.

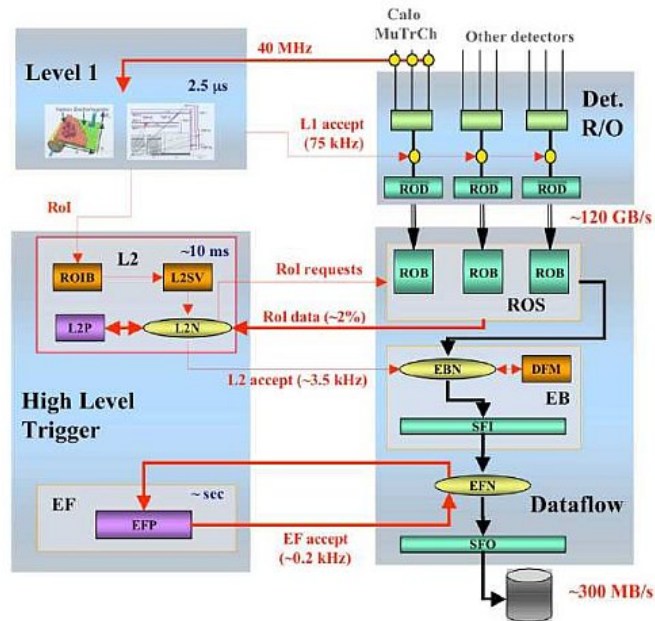


Figure 2.6: ATLAS TDAQ

2.4 The ATLAS Detector Upgrade

The environment expected at HL-LHC will require a radical change of most ATLAS systems, especially the ones at low radii and large pseudorapidity [5]. In particular, the Inner Detector, the forward calorimeter and the forward muon wheels will be affected by higher particle fluxes and radiation doses, and therefore will need to be upgraded, while the barrel calorimeters and muon chambers will essentially remain as they are now. The ATLAS upgrade is planned in three phases which correspond to the Long Shutdowns (LS) of LHC. In each shutdown some new improvements are gradually introduced into each subsystem while the luminosity is progressively increased.

The ATLAS detector upgrade is divided in the following steps:

- **LS1 (2013-2014):**

- an additional pixel layer (IBL) was installed to improve primary vertex resolution, secondary vertex finding and b-tagging;
- the cooling plant for the pixel and SCT was modified to an evaporative cooling system, while the IBL was equipped with a CO₂ based cooling;
- a new Diamond Beam Monitor (DBM) was installed;
- the coverage of the Muon Spectrometer between the barrel and the end-cap region was improved;
- the low voltage power supplies of all the calorimeters were changed.

- **LS2 (2019-2020):**

- new Muon Small Wheels will be installed to handle some degraded performance of the muon tracking chambers due to the expected increase of the cavern background. The new Muon Small Wheels are supposed to ensure efficient track reconstruction at high particle rates and large $|\eta|$ with position resolution of better than 100 μm ;
- new trigger schemes will be implemented to provide higher granularity, higher resolution and longitudinal shower information to the Level-1

trigger processors. This project is known as Fast Tracker (FTk), whose purpose is to find and fit the tracks directly at the level of the hardware, greatly reducing the time of processing. This will also imply a lower burden for the Level-2 trigger, which currently handles the track reconstruction, opening the possibility for more advanced selection algorithms, which ultimately could improve the b-tagging, lepton identification, etc. Suggestions are also in place for combining trigger objects at Level-1 (topological triggers) and for implementing full granularity readout of the calorimeter. The latter will strongly improve the triggering capabilities for electrons and photons at Level-1.

- **LS3 (2024-2026):**

- a new inner detector will be constructed and installed. It will be an all-silicon Inner Tracker (ITk). Further description of this particular sub-detector will be given in chapter 4, since it is particularly relevant for this thesis;
- two major improvements will be implemented for the calorimeters: first, the cold electronics inside the LAr Hadronic end-caps, as well as all on-detector readout electronics for all calorimeters, will be replaced; second, either the FCal will be fully replaced or a Mini-FCal will be installed in front of the current one in order to reduce the ionisation and heat loads on the FCal itself;
- a new trigger architecture will be implemented that at the same time respects the constraints imposed by the detectors and has the flexibility required by the new levels of luminosity.

Chapter 3

Semiconductor Detectors

Semiconductor detectors play a crucial role in particle physics and have a lot of applications in various other fields. In this chapter the main features of semiconductor detectors are presented. Firstly, the mode of operation and fundamental parameters of a pn-junction or diode operated in reverse biasing are described, then the current state of the art of silicon trackers is discussed and finally possible technology developments are presented.

3.1 PN-Junction

A pn-junction consists of two differently doped pieces of silicon, n-doped and p-doped, put together.

After they are put in contact, and before any voltage is applied to the pn-junction, the electrons in the n-doped region diffuse into the p-doped region and vice versa the holes diffuse from the p-doped region to the n-doped one. This continues until an equilibrium sets in, after which a potential difference (and consequently an electric field) is generated between the two zones, called built-in voltage V_0 , and a space region that is free of mobile charge carriers is created. In order to increase the depleted region thickness, the junction can be reversely biased with an external voltage V_B . A scheme of a pn-junction and its evolution into a radiation detector is shown in fig. 3.1. When a charged particle passes through

the depleted region, it sets free charge-carrier pairs (e^- - h^+) along its path, which can be collected then at the electrodes. In silicon, the number of electron-hole pairs produced by a Minimum Ionising Particle (MIP) in a volume of thickness $d = 100 \mu\text{m}$ can be evaluated by the following formula:

$$N_{e/h} = \frac{dE/dx \cdot d}{I_0} \approx 10^4 \quad (3.1)$$

where the mean ionisation energy $I_0 = 3.6 \text{ eV}$ and mean energy loss $\langle dE/dx \rangle = 3.87 \text{ MeV/cm}$ [13]. While drifting into the electric field, the charge carriers induce a signal at the electrodes that can be further processed by electronic circuits. The junction, whose behaviour is the same of a diode, can be fully depleted by applying the proper reverse biasing, leaving no free charge carriers in the whole bulk.

Generally a simple pixel detector is made of a sensor (a reversely biased

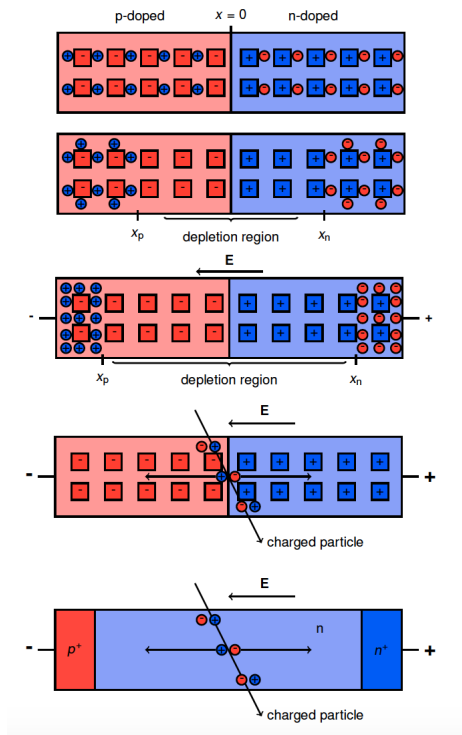


Figure 3.1: Schematics of a pn-junction and its evolution into a radiation detector.

diode) whose output is connected with the input of an analog/digital circuit which analyses the signal coming from the sensor. High reverse voltage bias is necessary

to have a large depleted zone where the electric field can drive the charges generated by particles crossing the depleted zone.

3.1.1 Depletion region

The width of the depletion region d is given by the sum of both depletion widths in the p- and n-region, x_p and x_n respectively, which in turn depend on the doping concentrations $N_{A,D}$ and the applied voltage V_B across the junction, as follows:

$$d = x_p + x_n = \sqrt{\frac{2\epsilon(-V_B + V_0)N_D}{eN_A(N_A + N_D)}} + \sqrt{\frac{2\epsilon(-V_B + V_0)N_A}{eN_D(N_A + N_D)}} \quad (3.2)$$

where e is the electron charge and ϵ is the permittivity of the material. Both widths x_p and x_n can be approximately of the same length regardless of the applied bias voltage. But this is not the general case in most applications, as for example in a typical semiconductor detector, where a highly doped p⁺-region interfaces with a normally n-doped region. Assuming $N_A \ll N_D$, the depletion region will extend in the p-zone ($x_p \gg x_n$) and its thickness will be:

$$d \simeq x_p \simeq \sqrt{\frac{2\epsilon(-V_B + V_0)}{eN_A}} \quad (3.3)$$

The depletion thickness can be more usefully expressed in terms of the resistivity of the silicon ρ_p and the mobility of the charge carriers (μ_h for the holes, μ_e for the electrons): in the case of p-type silicon, the following relation is valid:

$$\frac{1}{eN_A} = \rho_p \mu_h \quad (3.4)$$

Therefore, the depletion width becomes:

$$d \simeq \sqrt{2\epsilon\rho_p\mu_h(-V_B + V_0)} \quad (3.5)$$

This equation clearly shows the role of the bias voltage V_B and the bulk resistivity ρ_p in the depletion width. It is worth stressing that the depleted region is the pivotal part in particle detection.

3.1.2 Reverse current

An ideal diode when reversely biased has no current flowing through it. However, when a reverse voltage is applied to the junction, a small current induced on the electrodes can be observed flowing through the diode, producing noise and raising the baseline of the output signal. This current is mainly produced by electron-hole pairs thermally generated in the depleted zone, and also depends on the surface chemistry and the presence of contaminants. Of course, it is proportional to the area of the detector.

The reverse current depends exponentially on the temperature of the junction. It roughly triplicates for a $\Delta t = 10^\circ\text{C}$.

3.1.3 Capacitance

A diode is also characterised by an intrinsic capacitance which depends on the voltage applied to the junction. Considering a detector of area A with $N_A \ll N_D$, the depleted region is almost fully encapsulated in the p-type zone. The following equations can be written for charge and voltage:

$$\begin{cases} Q = eN_A A d \\ V = eN_A d^2 / 2\epsilon \end{cases} \quad (3.6)$$

with d the thickness of the depleted region, e the electron charge and N_A the number of acceptors. Assuming the detector is approximated as a parallel-plate capacitor, the capacitance is therefore given by:

$$C = \frac{Q}{V} = 2\epsilon \frac{A}{d} = \frac{1}{\sqrt{\frac{\mu\rho}{2\epsilon A^2}(-V_B + V_0)}} \quad (3.7)$$

with μ the mobility of the carriers, ρ the density, V_B the bias voltage.

3.2 Silicon detectors

The simplest silicon detector is just a semiconductor pn-junction under reverse bias. As mentioned before, the passage of a particle in the depleted silicon volume

generates a charge cloud. In order to obtain information about the position of a traversing particle, one side of the diode can be realised as a combination of micro strips or pixels. Different options are available for the realisation of the pn-junction. Often p+ implants in an n-type bulk are chosen, but also other options as n+-in-n silicon with a single p-type layer at the backside of the detector are possible. The readout can be performed either in DC or AC mode. In DC mode, the pixels are directly connected to the amplifier in the readout. In AC mode, the coupling is performed via a capacitor. Furthermore, the readout chain has to be grounded via a resistor. In DC-coupled detectors the whole leakage current is collected by the amplifier. Since the leakage current increases with irradiation, DC-coupling is disfavoured in detectors which are exposed to a demanding radiation environment, and the AC-coupled readout via a capacitor can be more suitable.

Silicon pixel detectors are mainly used for measuring the trajectory of particles. To do this, multiple planes of detectors are used to measure space points. To reduce the amount of material, and consequently reduce the multiple scattering of a particle in the detector planes, mostly built-in electronics are used. This can be realised in the following way: the readout chip is formed from a highly doped p+ material. This is covered with an insulating layer of SiO₂. An aluminium layer is placed on top which can be easily connected to the readout electronics. The resistor that is used for the connection to the ground potential can be realised. A guard ring is placed around the active detector region to isolate it from the sensor edge where high fields are present. A schematic cross-section of a silicon diode with an n-type bulk and p+ implants is shown in fig. 3.2.

The generated charge cloud is characterised by spatial and temporal structure that depends on incident particle type and trajectory as well as existing electric and magnetic fields in the silicon. Silicon detectors have a segmentation (granularity) in space and time that is approximately of the size of charge cloud deposits. This results in a 3-D space point for each particle crossing the sensors with a specific timestamp that, at accelerators, allows to associate the point with a given collision event. The magnitude of the collected charge can also be measured by pixel

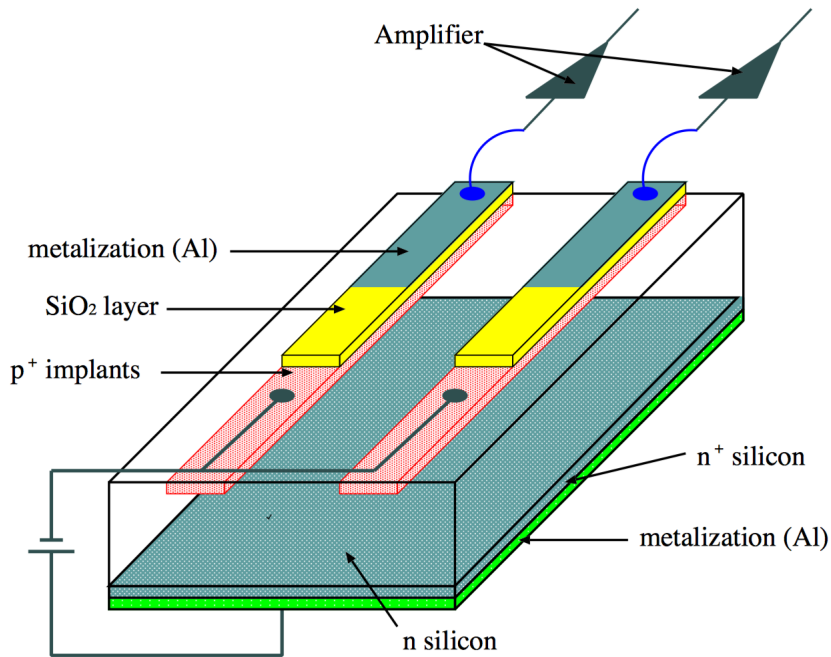


Figure 3.2: Schematics of a segmented silicon pixel.

detectors to improve the 3-D space point precision through interpolation as well as for particle identification through specific ionisation measurement. In current detector advancements an increased space and time granularity is being searched for, in order to measure and make use of the structure of charge deposits.

A pixel tracker must perform the following tasks:

- pattern recognition and identification of particle trajectories in presence of background and multiple tracks (high occupancy);
- measurement of primary and secondary vertices;
- multi-track separation and vertex identification;
- momentum measurement of particles in presence of a known magnetic field B (measurements of tracks curvature);

- measurement of specific ionisation.

To cope with possibly large background and track density the occupancy of the pixels must be kept low even at high particle rates, therefore the size of the pixel must be small. This also leads to good hit resolution. Space point resolutions in the order of $10\ \mu\text{m}$ or less have been routinely achieved at least in one dimension. To fulfil the previous tasks it is also important to have a good time resolution, which so far has reached the order of $10\ \text{ns}$.

3.2.1 From space point to tracks

In fig. 3.3 two situations of a particle hitting a pixel detector are represented. In (1) a particle hits the pixel module perpendicularly, leading to hit a cluster of typically one or two pixels. In (2) the particle hits the layer with a steep angle, thus producing a larger hit cluster with some directional information when properly treated by reconstruction algorithms, in particular when such clusters appear in several detector layers along a track.

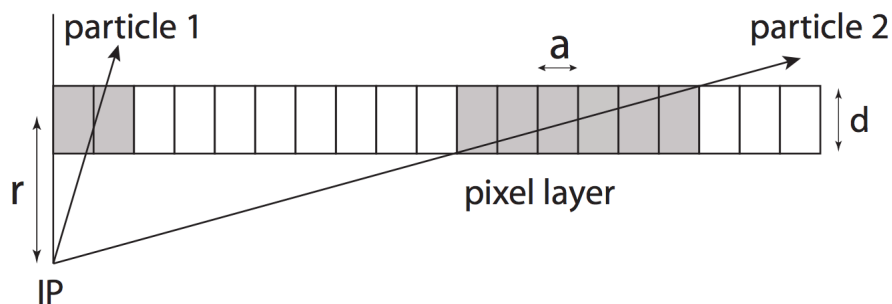


Figure 3.3: Pixel hit clusters for tracks under different incident angles.

The precision of a space-point measurement is essential to calculate resolution on the transverse momentum, as stated by the following equation, in a track

measurement with N detector layers:

$$\frac{\sigma_{p_T}}{p_T} = \left(\frac{p_T}{0.3|z|} \frac{\sigma_{point}}{L^2 B} \sqrt{\frac{720}{N+4}} \right) \oplus \left(\frac{\sigma_{p_T}}{p_T} \right)_{MS} \quad (3.8)$$

where p_T is transverse momentum in GeV/c, L is the radial length in meters, B is the magnetic field in Tesla, z is the particle electric charge in elementary units, σ_{point} is the space point resolution of the detectors in m, and N is assumed to be large in this approximation. Important for a precise momentum measurement is the point resolution, but also (quadratically) the total length L of the tracker and the bending field B . The multiple scattering (MS) contribution for a number of detector layers N can be written as:

$$\left(\frac{\sigma_{p_T}}{p_T} \right)_{MS} = \frac{0.0136}{0.3\beta BL} \sqrt{\frac{(N-1)x/\sin\theta}{X_0}} \sqrt{C_N} \quad (3.9)$$

where L is the tracker length projected onto the plane perpendicular to the magnetic field, and $x/\sin\theta/X_0$ is the total material thickness traversed by a particle incident with polar angle θ with respect to the beam, in units of the radiation length. C_N is a factor depending on the number of layers N : it starts at a value of 2.5 for a minimum of three layers and approaches 1.33 for $N \rightarrow \infty$ (continuous scattering).

Another parameter which is important to consider is the amount of shared charge between pixels. While this phenomenon allows for better spatial resolution by charge interpolation, signal decrease caused by irradiation during the detectors lifetime demands minimal charge sharing, since the fact a collected charge causes a hit also depends on the pixel threshold. Noise deteriorates the precision of reconstruction and causes spurious hits.

3.2.2 Radiation damage on silicon detectors

Silicon detectors, particularly those employed at hadron colliders, have to withstand large radiation doses, as they are often situated near the beam line. This is a pivotal problem when using silicon detectors, and their lifetime is reduced to a

few years.

Radiation damage in silicon can be grouped into two major groups: surface and bulk damage, depending on the part of the detector in which they occur:

- Surface damage is the damage occurring in the SiO_2 layer. It is mostly caused by ionising energy loss in the layer, where a gradual buildup of positive charge takes place. This is due to the fact that the holes generated in this region have a very low mobility, as opposite to the electrons and thus are captured in the layer. The charge buildup changes the capacitance of the detector and increases the surface current which adds to the leakage current.
- Bulk damage refers to the damage happening in the substrate bulk. It is mostly caused by the non-ionising energy loss (NIEL). Hadronic interactions dislocate silicon atoms from their original positions. The unoccupied lattice position is referred to as vacancy, the evicted atom, which most often will afterwards be placed at a non-lattice position is called interstitial. Single vacancies and interstitials are examples of point defects. Primary dislocated atoms can also collide with other atoms and create whole cluster defects. The probability of creation for cluster defects depends on the particle type and its energy. The NIEL hypothesis states that this effect can be normalised to the effect of neutrons with an energy of 1 MeV.

Electrical Properties of Defects

The radiation damage causes modifications in the characteristics of the material depending on where its situated in the band structure. If the defect happens near the centre of the band gap it acts as a generation or recombination centre. This effect can increase the leakage current by generating new electron-hole pairs. These defects can also trap the generated electrons and holes and re-emit them at a later times, resulting in a diminished charge collection efficiency. Defects that have a non-zero charge state at the operation temperature of the detector effectively contribute

to the change of the doping of the material. This change in the effective doping will result in a type inversion of the material after sufficiently large irradiation doses. The increase in the leakage current is another effect of the damage cause by radiation, and depends linearly on the fluence ϕ :

$$\Delta I_{leak} \propto \alpha V_{bias} \phi \quad (3.10)$$

where $\alpha = 10^{17}$ A/cm for detectors after long-term annealing which will be explained below.

The “Hamburg Model”

A simplified model that describes how the doping of the semiconductor evolves after being irradiated is called the “Hamburg Model”. The so-called annealing process describes how the defects reacts inside the detector of the material, effectively modifying the original doping of the semiconductor. These irregularities can travel inside the material and interact with lattice atoms or other defects. The evolution of defects depends on the environment temperature. The annealing process almost completely stops at temperatures below -10 °C. Above this temperature, the change in effective doping can be characterised by three distinct contributions [8].

1. **Short-term annealing:** it is the first type of contribution and is short term effect in the annealing of irradiated detector materials. After an increase of temperature the doping of the semiconductor is reduced compared to the state directly after irradiation. In case of type-inverted materials, this leads to a reduction of the depletion voltage, while for materials before type inversion, the depletion voltage is increased. In both cases, this is a positive effect for the for detector operation, and therefore is referred to as beneficial annealing. Beneficial annealing happens mostly at room temperature or above.

2. **Stable damage:** it is the second type of and main contribution to the change in effective doping of the semiconductor. It is time-independent and gives a lower limit for the change in the effective doping due to annealing. The stable damage contribution increases linearly with the absorbed dose.

3. **Reverse Annealing:** it is third type of contribution. This process happens with time-frames considerably longer with respect to the short-term annealing and has the opposite effect. After long periods at room temperature, the change in effective doping will instead increase, soon reaching levels higher than those directly after irradiation. This leads to unwanted changes in the operation parameters such as the depletion voltage. To avoid reverse annealing, maintenance periods with a warm-up of the detector to room temperature are kept as short as possible once the detector has received large amounts of radiation. Thus, the effects of short-term annealing should be maximised while keeping the contribution from reverse annealing small. The evolution of the effective doping for a 25 k Ω cm detector material after an irradiation of $1.4 \cdot 10^{13}$ MeV n_{eq}/cm^2 as function of the annealing time is shown in figure 3.4 [17].

3.3 Hybrid and monolithic silicon detectors

Hybrid pixel detectors are devices which consist of a sensor and a readout chip that are put together through a technique known as bump-bonding. Each part is optimised independently and work at very different voltages: the former requires tens or hundreds of volts to achieve a thick depletion layer (150-300 μm for standard sensors); the latter operates at about 2 V. The advantages of hybrid pixel detectors are that they are quite radiation tolerant and fast. Signals in all channels are in fact quickly processed in parallel. In addition, it is possible to use different technologies for the sensor and the readout chip, which allows for different combinations of those in order to further improve the radiation hardness of the

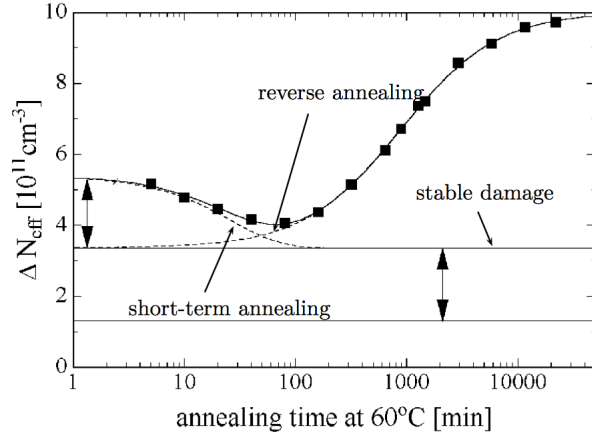


Figure 3.4: Evolution of the effective doping concentration ΔN_{eff} for a 25 k Ω cm material after a fluence of $1.4 \cdot 10^{13}$ MeV n_{eq}/cm^2 . The three components of short term annealing, stable damage and reverse annealing are shown separately.

whole device. Some disadvantages, however, are the high power consumption, the material budget and the large amount of time and cost that is needed to realise the bonding.

A goal in high energy physics is to make the trackers as thin as possible such that particles loose as little energy as possible and their multiple scattering is reduced. Therefore, efforts are made to keep both parts, the sensor and the readout chip, very thin. Another approach is to have a single device where sensor and readout electronics are built on the same silicon wafer. These sensors are called monolithic detectors: some of these, built with technologies called MAPS and INMAPS, are already employed in experiments with low-radiation environments (such as e^+e^- accelerators, Mu3e, ALICE Inner Tracking System, etc.). These sensors have a depletion region which is one order of magnitude smaller than the hybrid one ($\approx 30 \mu\text{m}$) and have specific protections that manage to insulate the readout electronic from the sensor region. The charges that the particles create when they cross the depletion region is mainly collected by diffusion. In high-radiation environments a significant number of charge trappings is produced as the sensor is subjected to radiation, which makes these devices not suitable for

environments like the one of ATLAS.

In order to use monolithic devices in high-radiation environments, an electric field must be present in the depleted region so that the charges can be collected by drift. Hence, the main challenge to the use of monolithic sensors in HL-LHC-like experiments is the need to improve their radiation hardness.

Chapter 4

The ATLAS Inner Tracker

An in depth analysis of the purposed design of the ATLAS Inner Tracker (ITk) to be installed at HL-LHC is carried out in this chapter, since the latter part of this thesis is aimed at this particular detector and in particular its outer layer.

4.1 Detector layout

The new Inner Tracker is going to replace the current Inner Detector and is planned to be an all-silicon tracker. Among different layouts that have been proposed, the most likely is called “Inclined Layout” [9]. It combines precision central tracking for an average $\mu \approx 200$ with the ability to extend the tracking coverage to a pseudorapidity $|\eta| = 4$ while maintaining excellent efficiency and performance. This layout is composed of two systems: a pixel detector and a strip detector surrounding it.

The pixel detector is divided in 5 layers assembled with a design called “Inclined Duals” layout, shown in fig. 4.1. The flat barrel layers are prolonged with a section of inclined modules that minimise the material budget in the barrel to end-cap transition region as well as the amount of silicon needed (inclined modules have a larger angular coverage in this region). The end-caps are made up of layers of pixel rings which extend the coverage in the z-coordinate (parallel to the beam line) and allow routing of the services separately along each ring. Both the

inclined module section and ring section can be individually translated to optimise the coverage.

The Strip Detector has four barrel layers and six end-cap petal-design disks,

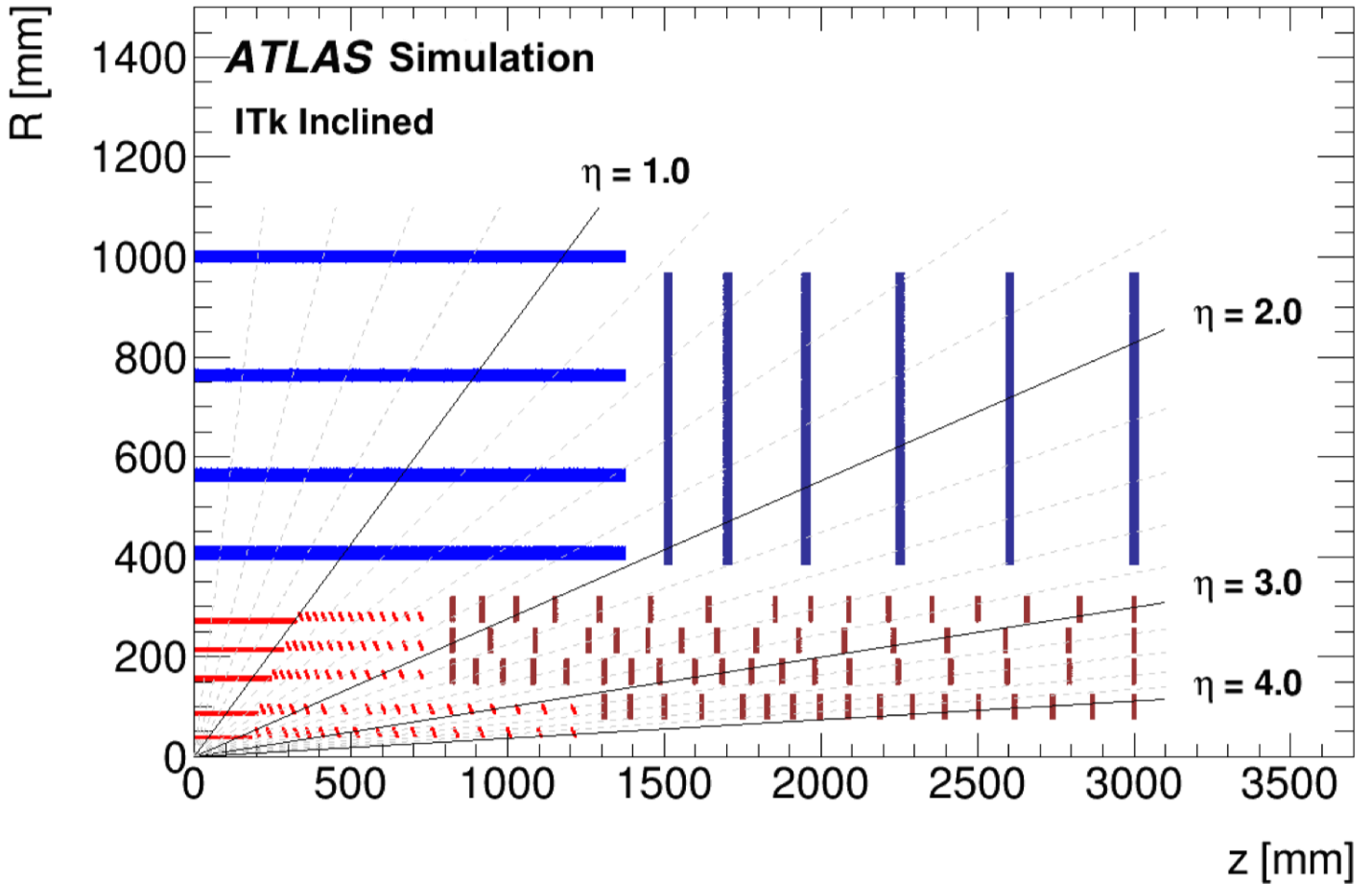


Figure 4.1: Layout of the Inner Tracker for the HL-LHC.

both hosting double modules with a small stereo angle to add z -resolution in the barrel and radial resolution in the end-caps (perpendicular to z). The Strip Detector covers a pseudorapidity $|\eta| < 2.7$.

The pixel and strip detectors are separated by a Pixel Support Tube (PST). In addition the two innermost layers of the Pixel Detector are replaceable, since they

are not expected to survive the full HL-LHC operation time. The two innermost pixel layers are separated from the outer three layers by an Inner Support Tube (IST), that facilitates replacement of the inner layers. The combined Strip plus Pixel Detectors provide a total of 13 space points for tracks in the region $|\eta| < 2.6$, with the exception of the barrel/end-cap transition region of the Strip Detector, where the tracks can be at most made of 11 space points. The pixel end-cap system is designed to supply a minimum of 9 space points from the end of the strip coverage in pseudorapidity to $|\eta| = 4$. The expected channel occupancy is $< 1\%$ for $\mu \approx 200$ and the material budget is reduced of a factor five for $|\eta| < 1$ with respect to the current inner detector. The expected channel occupancies for $\mu \approx 200$ are shown in fig. 4.2 .

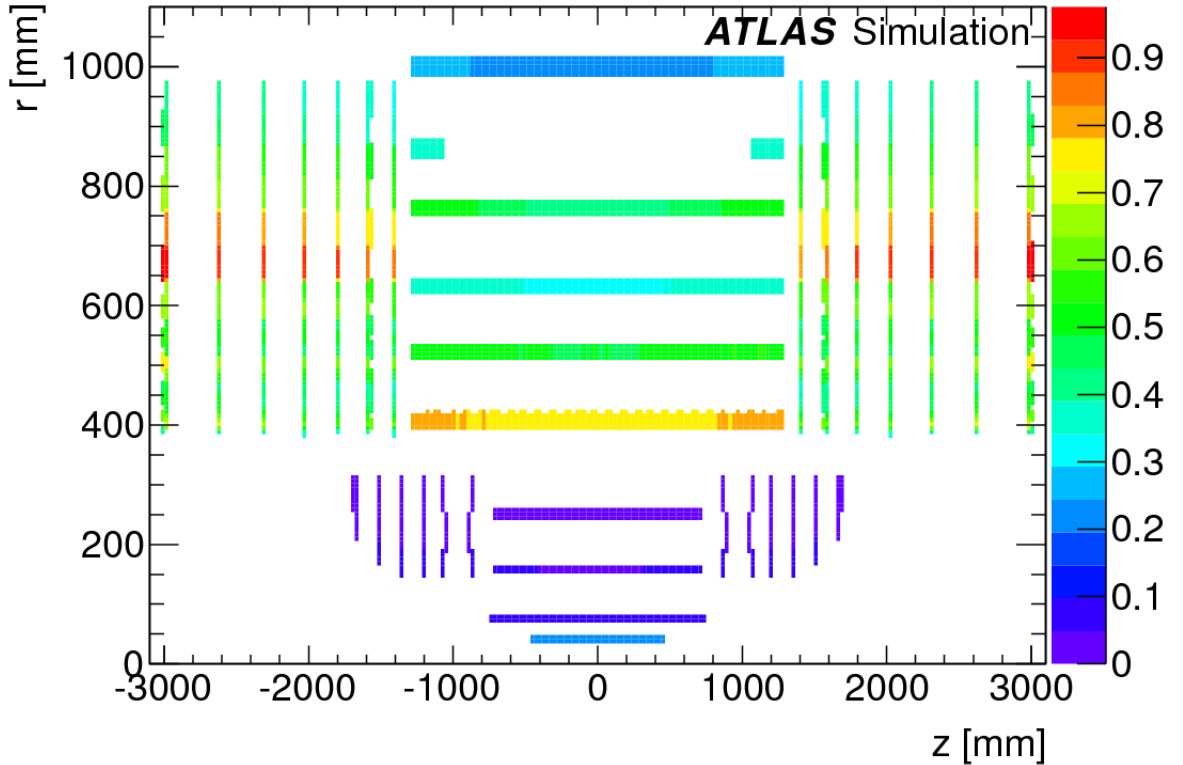


Figure 4.2: Expected Inner Tracker channel occupancies (in percent) for 200 pile-up events

4.2 Detector specifications

- **Radiation Hardness:** the sensor and its readout electronics must tolerate a radiation of 10^{16} n_{eq}/cm^2 in the innermost region. Here, the radiation background is dominated by particles coming directly from the proton-proton collisions. Moving to larger radii the background is dominated by neutrons that originate from high energy hadron cascades in the calorimeter material. Fig. 4.3 shows the expected 1 MeV- n_{eq} fluences, normalised to 3000 fb^{-1} of integrated luminosity. The radiation background simulation has been performed using FLUKA [11]. The maximum fluence and ionising dose in the different systems goes from $2.9 \cdot 10^{14} \text{ cm}^{-2}$ in the outer layer to $1.4 \cdot 10^{16} \text{ cm}^{-2}$ in the innermost one.

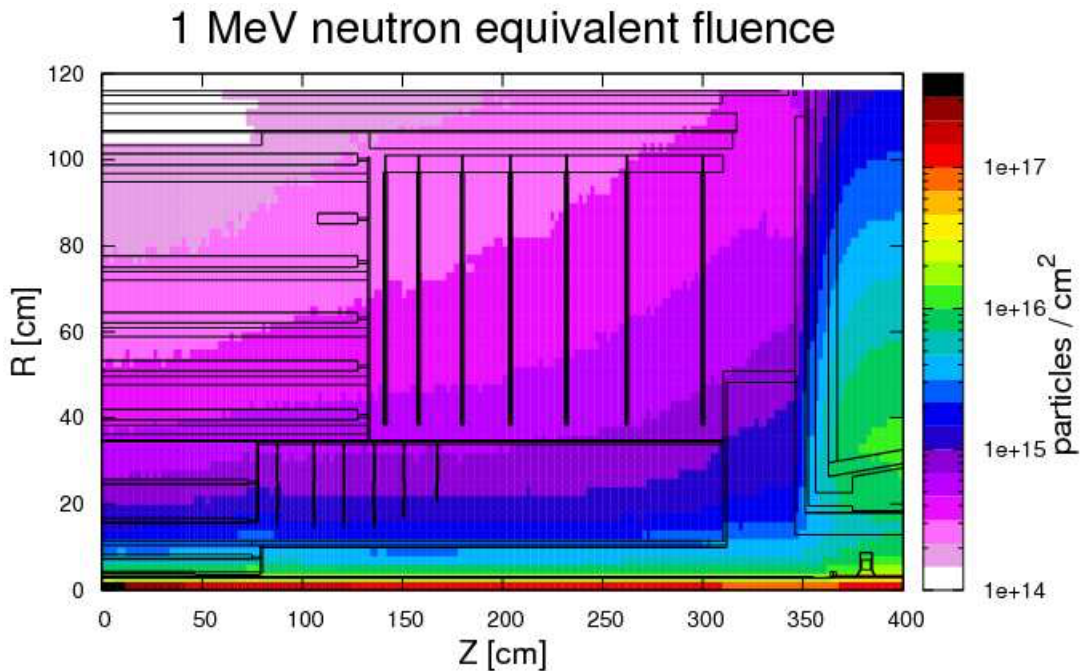


Figure 4.3: Expected 1 MeV neutron equivalent fluence in the ATLAS ITk region, normalised to 3000 fb^{-1} of pp interactions generated using PYTHIA8. For the outer pixel layer region, in the barrel, the maximum fluence is $1.7 \cdot 10^{15} \text{ cm}^{-2}$. The radiation background simulation has been performed using FLUKA.

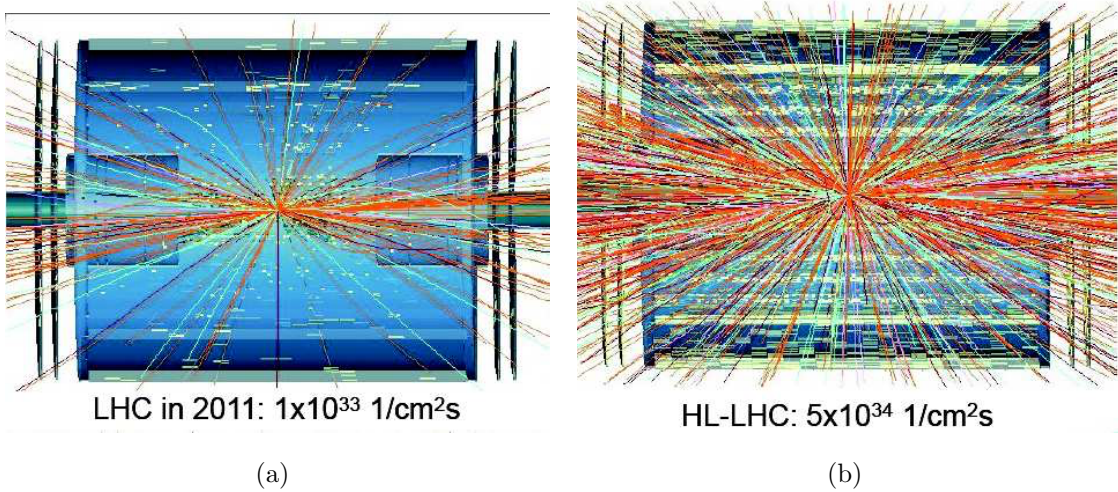


Figure 4.4: Simulation of tracks expected in the Inner Tracker region for the LHC (a) and the HL-LHC (b) scenarios.

- Occupancy:** In case of 200 pile-up events, a multiplicity of more than 1000 tracks per unit of pseudorapidity is expected in the tracker acceptance. Fig. 4.4 shows a simulation of pile-up events for the current level of luminosity in LHC as well as the predicted one in HL-LHC. In both the SCT and the TRT regions the occupancy will reach a level preventing them from resolving particle tracks. Some degradation in the TRT performance has actually already been observed in the most central heavy-ion collisions. Therefore the TRT is going to be replaced with strips with finer granularity than the existing ones. This is achieved by using a smaller pitch and thickness. The dimension of the outermost pixel radius is chosen to be 250 mm to obtain a good particle separation for highly dense jets and at the same time minimise gaps in the η coverage.
- Interactions with the material:** The interactions between hadronic particles and the detector material, as well as the Bremsstrahlung radiation of electrons, reduce the efficiency of tracking, therefore the amount of material with which the detector is built must be minimised. Reducing the material budget reduces multiple scattering, leading to a more precise measurement

of particle momentum, minimise photon conversions and track confusion, and leads to a better isolation of real photons. The number of secondary interactions is also decreased, leading to lower detector occupancy. Fig. 4.5 shows the material distribution in the proposed tracker system. It is a significant improvement with respect to the current ID, which contributes for more than $1.2 \cdot X_0$ in regions with $|\eta| > 1$, whereas the new tracker only adds $0.7 \cdot X_0$ in areas of $|\eta| < 2.7$.

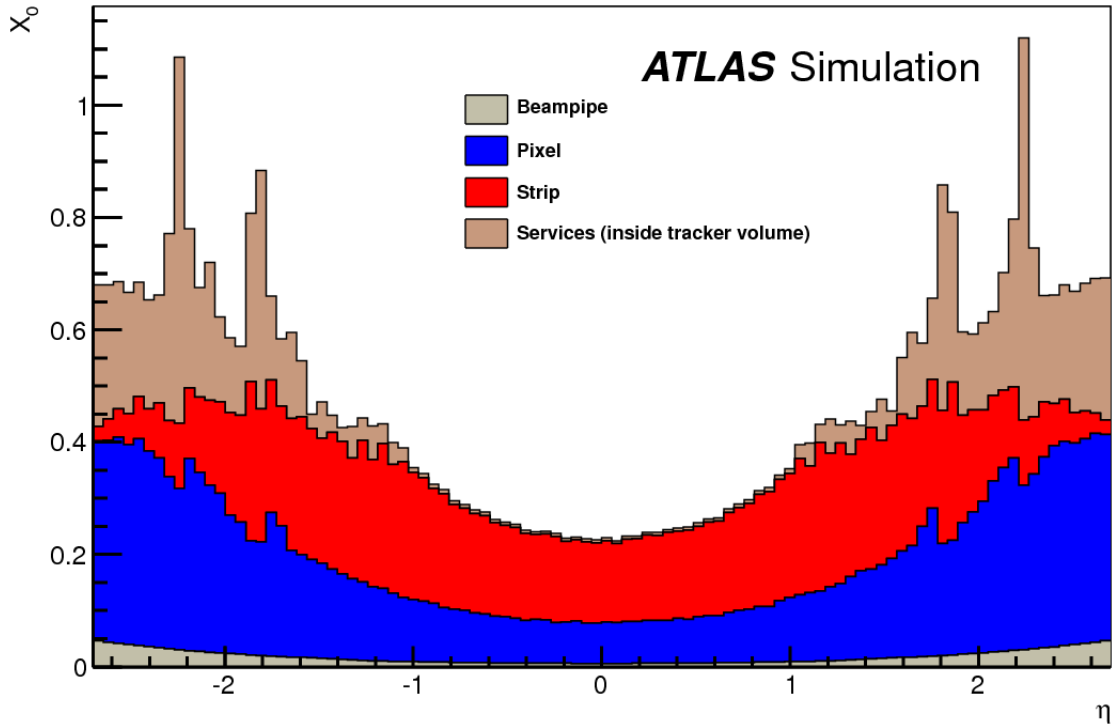


Figure 4.5: Silicon radiation length X_0 as a function of pseudorapidity η in the new ITk

- **Space:** the new tracker must fit in the space currently occupied by the Inner Detector. Also the current gaps between the sub-detectors must be preserved for cables and supports. Therefore the Pixel Detector must have a total area of 8.2 m^2 with at most 683 million of cables, while the Strip Detector must cover 19.2 m^2 with 74 of million cables.

A further requirement is a modular approach in view of the current silicon technologies and further developments (active and monolithic pixels) to be eventually implemented. Considerations of cost and energy consumption play of course an important additional role.

A comparison between some performance of the current Inner Detector versus the new Inner Tracker can be seen in table 4.1.

Track Parameters $ \eta < 0.5$	ID with IBL and no pile-up	ITk with 200 events pile-up
Inverse transverse momentum (q/p_T)[TeV]	0.3	0.2
Transverse impact parameter (d_0)[μm]	8	8
Longitudinal impact parameter (z_0)[μm]	65	50

Table 4.1: Performance the ID with IBL and the ITk of HL-LHC for transverse momentum and impact parameter resolution.

4.3 Pixel Modules for ITk

Different pixel detector technologies are currently being studied to cope with the different radiation levels in relation with the distance from the beam line, as well as the module assembly and production costs for the area to be covered in the different layers. The pixel size needs to be small, in particular close to the interaction point, in order to fulfil the larger detector occupancy [18].

4.3.1 Front End Chip

A new Front End (FE) chip for the hybrid pixel modules of ITk is being developed and produced to tolerate the harsh radiation fluence and the high particle multiplicity at HL-LHC. The RD53 collaboration at CERN already built a prototype of the final ITK chip with a 65 nm CMOS process. The collaboration is a joint venture between the ATLAS and CMS experiments. This new chip has dimensions of approximately $2 \times 2 \text{ cm}^2$ and its main characteristics will include a

smaller pixel size of $50 \times 50 \mu\text{m}^2$, which will result in a larger number of readout channels with respect to the present chips, and a radiation hardness tolerance of 500 MRad. It will also be able to reach thresholds lower than 1000 electrons, therefore allowing to work with smaller signals and thus reducing the thickness of the substrate. The first version of the RD53 chip, the RD53-A, has been developed and the distribution of the first modules has just started. Meanwhile, a first small prototype developed to test the analog FE part of this chip, called FE65-P2, has been characterised demonstrating the possibility to achieve thresholds as low as 500 electrons to detect particles within 25 ns with general good performance even after ageing.

4.3.2 Pixel Sensor Technologies

The future ITk chip will be composed of both $50 \times 50 \mu\text{m}^2$ and $25 \times 100 \mu\text{m}^2$ sensor pixel sizes. The reduced pixel dimension will improve position resolution and in the case of 3D sensors also result in an increased radiation hardness.

- **3D sensors:** the 3D sensor technology is already used in the IBL of the present ID. It consists of an active bulk of p-type silicon into which a lattice of n-doped and p-doped column-shaped electrodes are implanted perpendicularly to the sensor surface. While in the usual planar sensor design the electrodes are situated on the opposite surfaces of the active bulk, in 3D sensors the charge collection distance is separated from the active substrate depth and thus the number of electron-hole pairs generated by MIP passing through the active bulk remains unaffected. This results in a reduced electrode distance that does not diminish the amount of charge created by MIPs, therefore the sensor is operated with a low voltage and is less prone to charge trapping after high irradiation fluences. As shown in fig. 4.6 for the case of the IBL design, 3D sensors, after irradiation up to $9 \times 10^{15} \text{ n}_{eq}/\text{cm}^2$, need less than 180 V to reach a hit efficiency similar to the one before irradiation. At these operational voltages the power dissipation is normally less than $15 \text{ mW}/\text{cm}^2$. By reducing the pixel size of the 3D detectors for ITK, and therefore the electrode distance, the performance is expected to

increase. The production of 3D devices is extremely complicated, and thus impinge upon the yield, the production time and the costs which scale with the number of column electrodes. 3D sensors are thus optimal candidates for the innermost layers where the radiation hardness requirements are more severe but the area to be covered is relatively small.

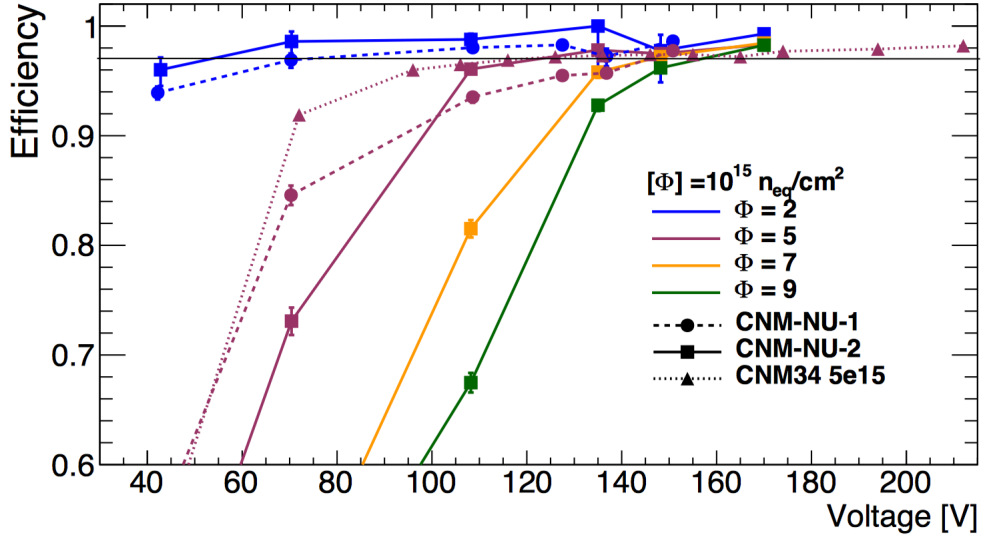


Figure 4.6: Hit efficiency as a function of the bias voltage of 3D pixel sensors produced by CNM, irradiated with protons up to a fluence of $9 \times 10^{15} \text{ n}_{eq} \text{ cm}^{-2}$

- **Planar sensors:** the n-in-p technology has been chosen as the default for planar sensors in the ITk since the single side processing needed is potentially cost-reducing as opposite to the present n-in-n sensor technology employed in the ATLAS pixel detector. The active sensor region can be adjusted in relation with the required radiation hardness, while still reducing the operational voltage necessary to optimise both hit efficiency and power dissipation. A thickness of $150 \mu\text{m}$ is expected for the outer barrel layers and the end caps, whereas, for the innermost layers, studies have shown that a thickness of $100 \mu\text{m}$ for n-in-p planar pixel sensor produces the best performance in terms of charge collection, hit efficiency and power dissipation after irradiation to

the HL-LHC fluences. Since in the innermost layers of ITK the limited overlap space requires the minimisation of inactive areas at the periphery of the modules, planar sensor with active edges are also being considered. Such devices are obtained extending the backside implantation to the edge of the sensor allowing to reduce the guard ring structure. This technology allows to produce slim edge planar sensors with an inactive area as small as $50\ \mu\text{m}$ at the periphery of the sensor, as shown in fig. 4.7, and even fully active edge sensors, depending on the active thickness, if no bias ring nor floating guard rings are used.

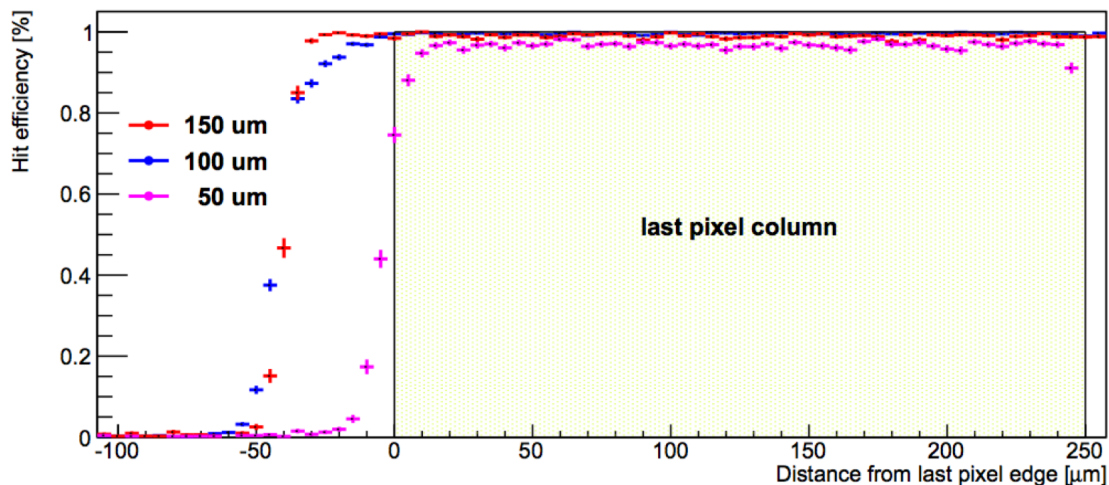


Figure 4.7: Hit efficiency as a function of the distance from the end of the last pixel implant for n-in-p active edge pixel sensors without bias ring and with floating guard ring structures

- **HV/HR CMOS sensors:** High Resistivity and High Voltage CMOS devices are investigated as an option for the large area to be covered in the fifth barrel layer of the ITk, due to the cost benefits coming from the industrial process. This technology can be employed to produce cost-effective passive sensors to be interconnected to ITk readout chips with the usual bump bonding techniques or active pixel sensor embedding a first amplification

stage which would allow for potentially cheaper capacitive interconnection via thin glue layers. The most effective solution would be obtained with fully monolithic module, with both analog and digital electronic implemented on the sensor substrate, which would completely remove the interconnection costs. First CMOS detector prototypes investigating these three options are presently investigated to prove their radiation hardness and their capability of fulfilling all ITK requirements, in particular the 25 ns time resolution and the power consumption.

Chapter 5

BCD8 and TowerJazz Technologies

In this chapter two technologies for high-resistivity, high-voltage CMOS detectors for the external layer of the ATLAS Inner Tracker are presented: BCD8 and TowerJazz. In particular two prototypes, the KC53AB and the TowerJazz Investigator, are presented: the former has been developed by STMicroelectronics and the latter by Tower Semiconductor Ltd. I personally measured the characteristics of these two prototypes, which are required to qualify them as tracking devices.

5.1 BCD8 Technology

The Bipolar-CMOS-DMOS (BCD8) is a 160 nm high voltage CMOS technology produced by STMicroelectronics. This technology has been developed for the automotive industry, which features components that work at low voltage, but must also tolerate high voltage spikes (some tens of volts) generated by the turning on and off of inductive loads, such as electrical motors. It is an appealing technology because it will be maintained for several years, due to the large volume production for industrial applications. This technology combines Bipolar, CMOS and DMOS technologies, therefore low-voltage devices (CMOS) and high-voltage devices (Bipolar and DMOS) coexist in the same substrate. The developments



Figure 5.1: Cross section of BCD8 sensor technology

needed to use it as a radiation detector are the result of a collaboration between STMicroelectronics and R&D project funded by INFN-2.

The sensor structure is composed by an epitaxial silicon layer on which multiple digital or analog CMOS circuits can be built, as they are completely surrounded by an n-doped zone which isolate the internal epitaxial layer from the substrate. The voltage drop between the n-doped isolation zone and the substrate is called “External Voltage” and the voltage drop between n-doped the isolation zone and the internal epitaxial layer is called “Internal Voltage” [15].

The components of this technology are shown in fig. 5.1. Starting from the bottom one can find:

- an n-doped zone in the wafer called “Buried Layer”;
- two n-doped isolations called “Niso” and “Nwell”, built on the buried layer;
- a p-doped zone, called “Pwell”.

Pn-junctions are formed between the three N-doped zones (Buried layer, Niso and Nwell) and the substrate which surrounds the previously mentioned components (lightly p-doped). The isolation of the internal epitaxial layer is done by biasing the substrate with the lowest voltage (-50 V) and the n-doped isolation zone with the highest voltage (1.8 V). In this way, the corresponding pn-junctions are reversely biased. The depleted region is in the substrate, since the isolation zone has

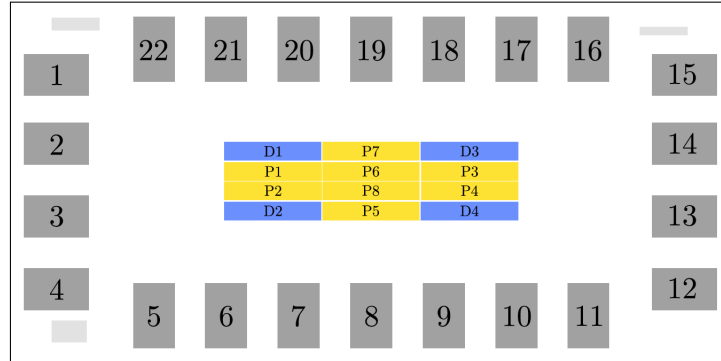


Figure 5.2: KC53AB chip scheme: D1-D4 are passive diodes, P1-P8 are active pixels, 1-22 are connector pads (VDD/GND and I/O)

a bigger doping than the substrate. This structure allows the insulation between the internal epitaxial layer and the substrate for any external voltage. The insulation from any internal voltage is done through the Nwell isolation ring, which surrounds laterally the epitaxial layer, and the Niso ring. The Buried Layer is used to isolate vertically the internal epitaxial layer. Thus, the BCD8 technology allows to transfer part of the front-end circuitry on the sensor wafer and to reduce sensor dimensions.

5.1.1 The KC53AB prototype

The first prototype built in bcd8 technology and known as KC53AB consists in a chip hosting 12 pixels of $250 \times 50 \mu\text{m}^2$ built on a $125 \Omega\text{-cm}$ resistivity substrate. Electronic circuitry including an amplifier and a buffer is implemented in 8 of the pixels, together with a single charge inspection system, and can be coupled capacitively to the FE readout chip, therefore eliminating the need of bump bondings. The actual area of each pixel is about $240 \times 40 \mu\text{m}^2$. Four pixels are simple passive sensors and occupy the corner of the chip (see fig. 5.2 for details), their cathode is connected directly to a pad. In the active pixels the buffer output is connected to a pad. As explained before, the pixel is a pn-junction between the substrate of the chip (anode) and the Buried Layer inside it (cathode), which is connected to the

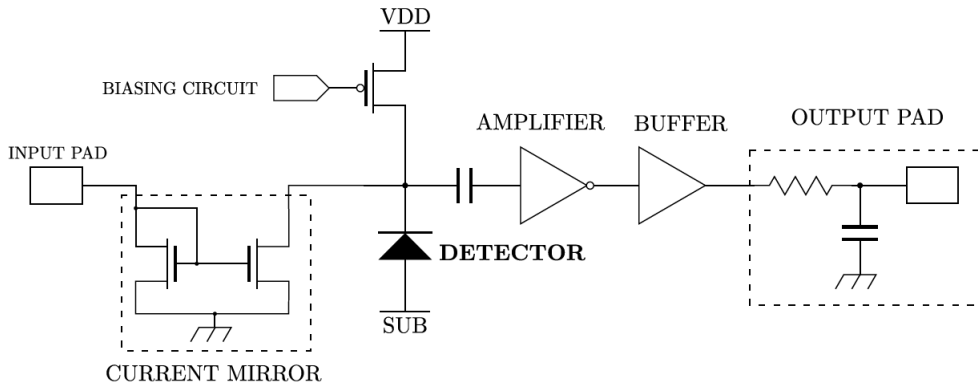


Figure 5.3: Scheme of the electronic chain of the active pixels.

pad through the Niso and the Nwell. For the passive pixels the Nwell is directly bonded the pad, while for the active pixels the pad is connected to a circuitry above the Buried Layer, which consists of:

- a PMOS transistor (which acts as a resistor) to bias the Nwell;
- a capacitor to decouple the n-well from the rest of the circuitry;
- an amplifier and a buffer.

The complete electronic chain of an active pixel is shown in fig. 5.3. The PMOS transistor is $10\ \mu\text{m}$ long and $500\ \text{nm}$ wide and its gate is connected to a dedicated biasing circuit in order to make it act as a high value resistor. The transistor is connected to the amplifier through a $500\ \text{fF}$ Metal-Oxide-Metal (MOM) capacitor. The amplifier, in turn, is connected to a buffer and then to the output pad.

The pads consist of $160 \times 100\ \mu\text{m}^2$ metallic surfaces which allow connections to the power supply and other external circuitry. All the pads are insulated from the substrate (except for the SUB pad, described hereafter) with a structure similar to the one of the pixel (Nwell, Niso, and Buried Layer). There are four types of pad:

- **VDD (high voltage) and GND (ground) pads:** pads through which the electronics on the active pixels is powered. They are built with one protection diode (VDD pad towards GND and vice versa) and no resistors.

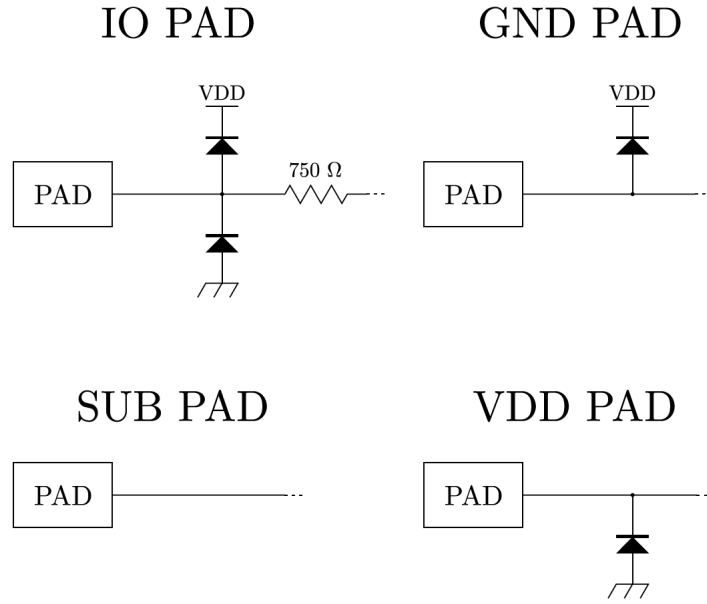


Figure 5.4: Scheme of the different types of pads.

- **SUB pad:** pad connected to the substrate, without protection diode or resistor. It also lacks the Nwell and is therefore directly on top of the substrate. This is where the V_{bias} is connected to deplete the region in the substrate.
- **IO pads:** pads through which it is possible to inject a test current in the active pixels and read the output of the amplifier. They feature two protection diodes each (one towards VDD and one towards GND) and are connected to the chip interior through a 750Ω polysilicon resistor.

The schematics of the pads are shown in fig. 5.4. The diodes and resistors they feature are for protection against voltage spikes, like in the case of an electrostatic discharge.

5.2 The TowerJazz Technology

The TowerJazz 180 nm CMOS imager process is a high-voltage CMOS technology that has already been used in the development of the monolithic CMOS

sensors for the ALICE experiment [6]. It is developed by Texas based industry Tower Semiconductor Ltd. In order to correctly function at the radiation level of HL-LHC, the standard process has been modified as explained later. The cross-section and top-view of a pixel in the standard process are shown respectively in fig. 5.5 and 5.6, and the feature of the TowerJazz imaging process are listed in table 5.1. The main components of the pixel in the standard process are as

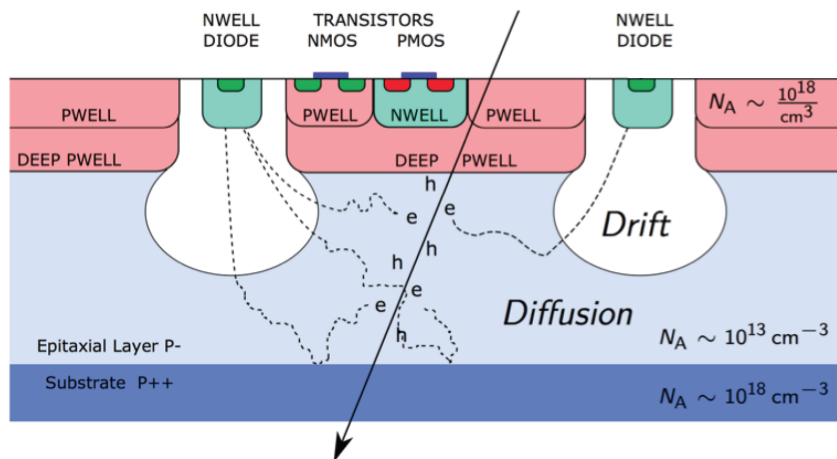


Figure 5.5: Cross section of TowerJazz sensor technology in the standard process.

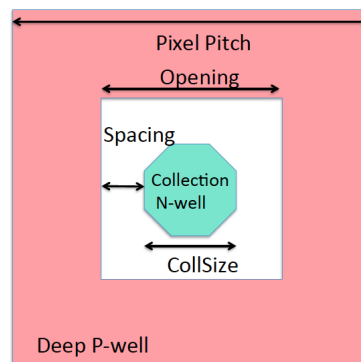


Figure 5.6: Top view of TowerJazz sensor technology in the standard process.

follows:

- three p-doped layers with different doping concentrations used to guide the electrons towards the collection n-well: the p^+ doped Pwell, the P^- high

resistivity epitaxial layer which hosts the depletion zone and the P⁺⁺ highly p-doped substrate. At the P⁻-P⁺⁽⁺⁾ junctions, electric fields are generated that act as reflective barriers for the electrons;

- an n-doped collection Nwell diode;
- a deep Pwell (a specific feature of the technology) whose role is to shield the Nwell of the PMOS transistors from the high voltage in the substrate, allowing for full implementation of CMOS circuitry within the pixel while retaining full charge collection;
- the readout circuit, which outputs the signal generated by the charge collected in the collection Nwell diode.

By applying a negative voltage to the deep Pwell and P⁺⁺ substrate with respect to the collection electrode, a region in the epitaxial layer gets depleted as indicated in white in fig 5.5. In this zone ionisation charge is directed to the Nwell diode (electrode) by drift in the electric field. Outside this region charge motion is dominated by diffusion, the induced signal is slower and the charge itself is more prone to trapping. Parts of the electrons generated in this space between the depletion volumes may migrate towards different collection n-wells, and thus be detected by different pixels. This phenomenon is known as charge sharing, and generates pixel clusters.

When an n-well collects charge, the output signal drops proportionally to the collected charge. Each pixel behaves as a capacitor, and thus the voltage drop can be expressed as

$$\Delta V_{IN} = \frac{Q_{col}}{C_p} \quad (5.1)$$

where ΔV_{IN} is the voltage drop recorded at the sensing node, Q_{col} is the collected charge and C_p is the pixel input capacitance. The signal can thus be increased either by collecting more charge or by decreasing the pixel input capacitance. ΔV_{IN} is also the voltage applied to a source follower transistor which is used to uncouple the impedance, and thus the output voltage can be expressed as:

$$\Delta V_{OUT} = g\Delta V_{IN} \quad (5.2)$$

where g is the gain of the further buffering and amplifying stages.

The size of the charge collection electrode and other pixel dimensions are

Feature	Property
MOS channel length	180nm
Metals	6 layers, Aluminum
Supply rail	1.8V (up to -6V on substrate)
MOS transistor types	full CMOS
Wafer type	epi p-type $25\mu\text{m}$ ($>1\text{kW-cm}$) thickness on p-type substrate
Backside implant	none

Table 5.1: Features of the TowerJazz imaging process.

listed in tab. 5.2 and correspond to the picture shown in fig. 5.6.

The extent and shape of the depleted zone depend on geometrical parameters

Pitch	Collection n-well size	Spacing
$25 \times 25 \mu\text{m}^2$	$3\mu\text{m}$	$3\mu\text{m}$
$30 \times 30 \mu\text{m}^2$	$3\mu\text{m}$	$3\mu\text{m}$
$50 \times 50 \mu\text{m}^2$	$3\mu\text{m}$	$18.5\mu\text{m}$

Table 5.2: Pixel cell characteristics of some of the pixel matrices in the TowerJazz Investigator.

like the diameter of the n-type collection well and the spacing between the collection n-well and the deep p-well, as well as the epitaxial layer thickness. Details of pitch and spacing play a significant role in the signal response as they influence the detector capacitance and signal amplification.

The depletion zone and charge collection is further influenced by the epi-resistivity and applied substrate voltage. The optimal choice should minimise the capacitance, maximise the signal amplitude and allow to achieve circuit designs optimised for low power and full charge collection efficiency after radiation.

For application in high radiation environments like the ATLAS ITk of HL-LHC,

the standard TowerJazz process had to be modified to minimise the non-depleted area in the epitaxial layer at the edges of the pixel, where significant charge loss might occur [1]. The best way to obtain fast charge collection by drift is a fully depleted epi-layer: the process modification consists in a planar deep n^- -p junction as shown in fig. 5.7. Such modification isn't a significant change in the layout, thus the same design can be used in both standard and modified process.

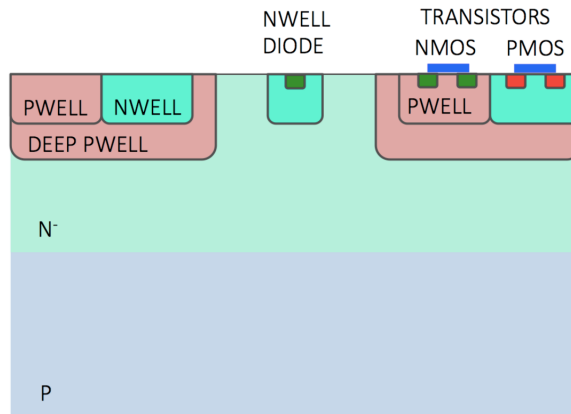


Figure 5.7: Cross section of TowerJazz sensor technology in the modified process with the addition of a deep n^- -p, extending the depleted area into the epi-layer.

5.2.1 TowerJazz Investigator

The Investigator chip is one out of a series of test chips designed to get a deep understanding of the pixel geometry influence on the analog behaviour of the chip itself. The chip doesn't contain any digital circuitry and allows the study of the signal shape, its size, as well as the charge collection timing and cluster behaviour. In total 134 different pixel matrices are available in the chip with pixel sizes from 20×20 to $50 \times 50 \mu\text{m}^2$. In fact, the aim of the Investigator is to find the geometry most suitable with radiation detection in ITK, as well as different pixel reset implementations (active transistor reset or continuous diode reset). Each matrix contains 8×8 active pixels surrounded by one line of inactive dummy pixels to separate it from the others, reducing edge effects. An example is shown in

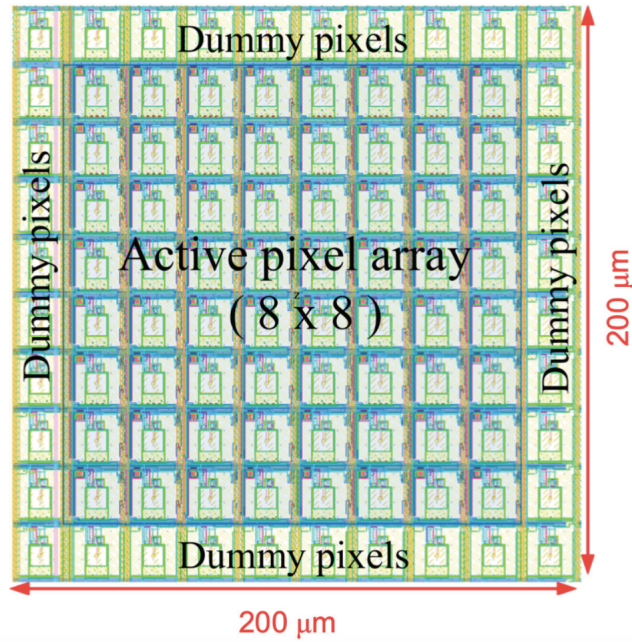


Figure 5.8: Pixel matrix of 8x8 pixels surrounded by dummy pixels

fig. 5.8. All the pixels in the same matrix are biased in the same way but are not further connected. Each pixel is connected to a signal input transistor and a reset transistor. Each input transistor is in turn connected via two signal buffers to the chip periphery. The Investigator allows simultaneous measurements of the analog signals of 64 pixels, e.g. a full matrix. The amplitude of the output signal is proportional to the ionisation charge collected by the input transistor, while the rise-time of the signal is limited between 10ns and 15ns by the front-end and output circuit.

Chapter 6

Tests on KC53AB passive pixels

In this chapter the measurements I performed on the KC53AB prototype, to characterise its passive pixels, are presented. Measurements of un-irradiated samples were performed in Bologna, while samples subjected to a dose of 10^{15} n_{eq}/cm^2 at the Laboratori Nazionali del Sud in Catania were measured during and immediately after the irradiation campaign. The reverse current and the capacitance of the four passive diodes have been measured as a function of the bias voltage. Capacitance measurements are used to evaluate the depletion depth of the sensor and compare it to expectations.

6.1 Current as a function of voltage

Current vs. voltage (IV) measurements are carried out to estimate the reverse current flowing into each passive pixel in the prototype when no radiation hits the detector and to evaluate the break-down voltage.

To perform the measurements the chip is glued and wire-bonded to a PCB (fig. 6.2) designed at Politecnico of Milano. The four passive-diode pads are connected to Lemo connectors. When performing IV scans, the protection diodes inside the KC53AB must be taken into account, because they may contribute to the reverse current. The schematic of the diodes inside the chip is shown in fig. 6.1. The PCB

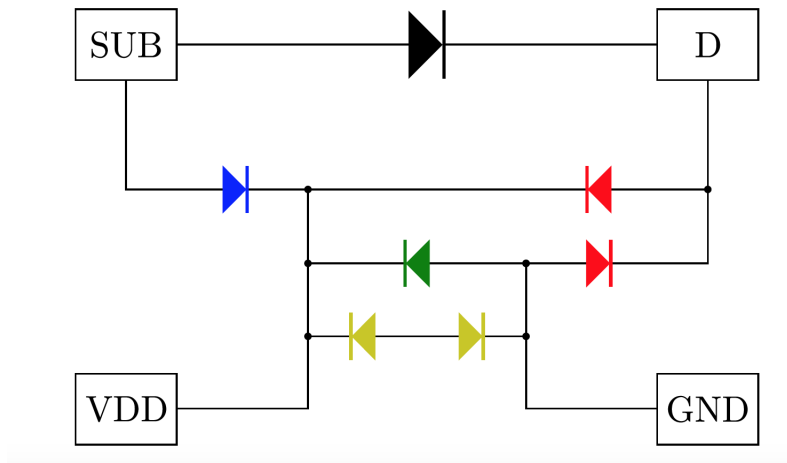


Figure 6.1: Schematic of protection diodes inside the chip

features a filter on the power supply on the substrate pad, in order to slow down the voltage rise and prevent damages to the chip [19].

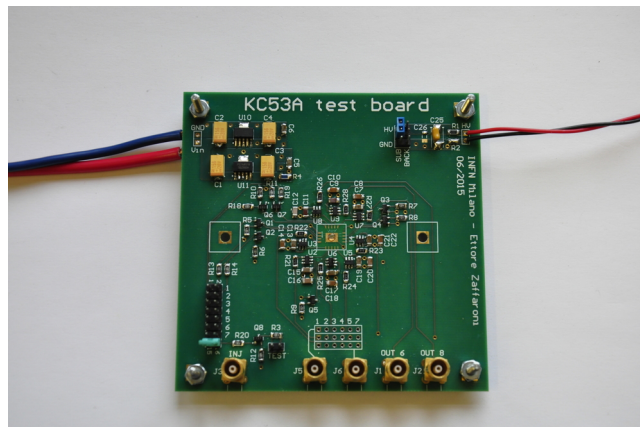


Figure 6.2: PCB board to host the KC53AB and allow for his testing.

The measurements have been performed by using two instruments: a Keithley 6485 picoammeter and a Keithley 2410 source meter. The picoammeter has a precision of 20 fA, which is needed because the reverse currents that are measured are very small (< 20 pA). For each value of voltage 100 current measurement are taken, then the mean value and the standard deviation are extracted. The source

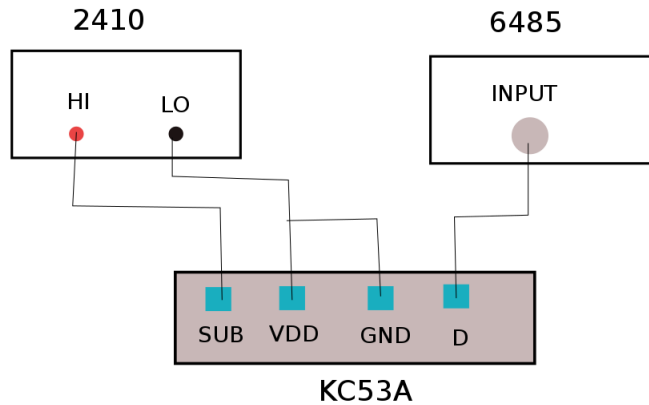


Figure 6.3: Diagram of the connections between the PCB hosting the KC53AB chip and the Keithley 2410 source meter and the 6485 picoammeter.

meter, covering the range from 0 V to +1000 V, is used to bias the chip. A diagram showing how the picoammeter and the source meter were connected to the PCB is shown in fig. 6.3. Both GND and VDD pads are connected to the ground of the source meter in order to switch off the protection diodes and measure only the current flowing through the sensors diodes. IV scans were performed in a dark environment to avoid the parasitic current generated by the light photons. In addition, the temperature of the room was controlled with air conditioning, to limit fluctuations. Scans were automatised to limit the human presence around the chip, via a computer running a python script handling the source meter and the picoammeter via a GPIB interface. Scans were performed in steps of 5 V from 0 to the breakdown, and vice-versa. The mean value is calculated for the currents corresponding to the same voltage, and the results are shown in fig. 6.4. The reverse current is a few orders of magnitude smaller than the expected size of the signal generated by a minimum ionising particle (MIP) which is around $1.5 \mu\text{A}$, as detailed in the following section. Figure also shows that the junction breakdown voltage is at about -70V, value which is expected from simulations. Therefore the

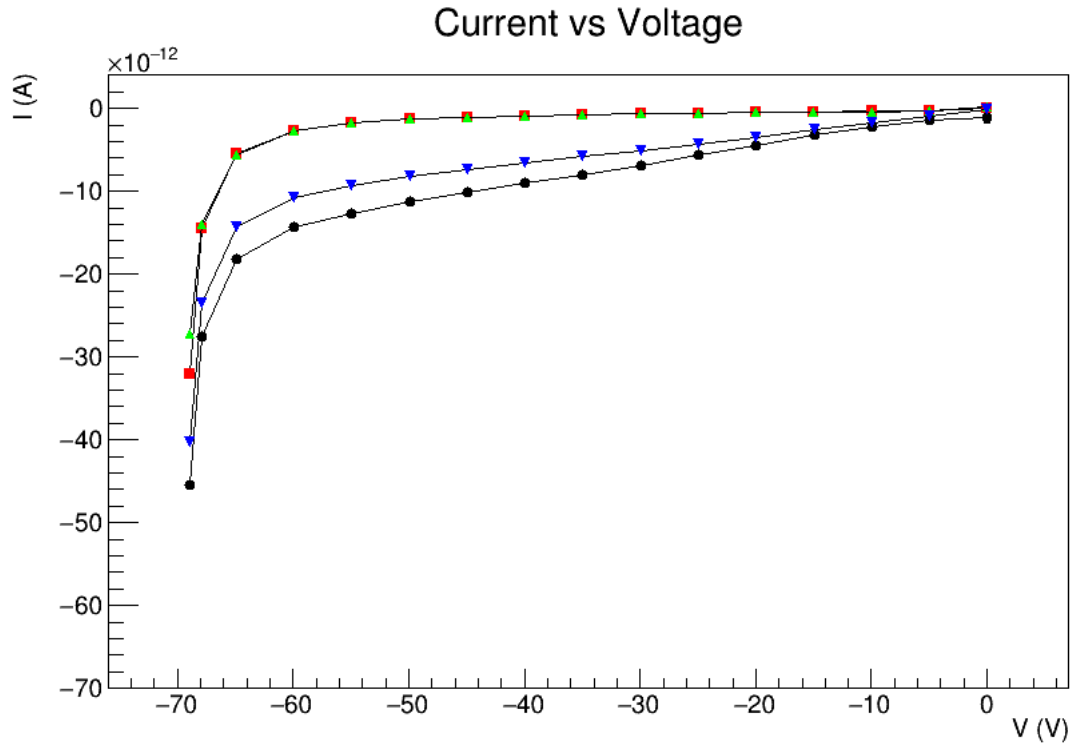


Figure 6.4: Current vs Voltage measurements for the 4 passive diodes in the KC53AB chip.

sensor behaves as expected and is compatible with the sensor technology used.

6.2 Capacitance as a function voltage

The capacitance characteristic of the passive diodes has also been measured through capacitance vs. voltage (CV) scans. The setup is similar to the one used for the IV measurements, though only one instrument has been used: a Keithley 3330 LCZ meter. This instrument allows to measure the capacitance at a fixed voltage with a precision of about 1 fF. The functioning is as follows: while the DUT is subjected to a 1 MHz, 10 mV RMS test signal, the meter measures the voltage across and the current through the DUT. From the ratio of these, the me-

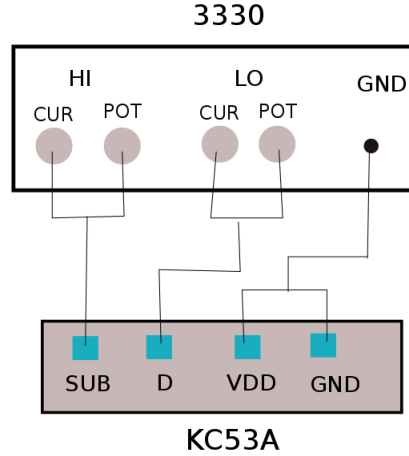


Figure 6.5: Diagram of the connections between the PCB hosting the KC53AB chip and the Keithley 3330 LCZ meter.

ter can determine the magnitude of the impedance and the phase angle between the voltage and current. Through the impedance and the phase the capacitance of the DUT can be evaluated.

A diagram showing how the LCZ meter was connected to the PCB is shown in fig. 6.5. As for the previous measurements, the procedure has been automatized using a computer running a python script that commands the LCZ meter to set the voltage and read the corresponding capacitance.

Capacitance (C) vs applied bias voltage (V_B) measurements are shown in fig. 6.6. They have been fitted with the following equation:

$$C(V_B) = C_P + \frac{1}{\sqrt{k(-V_B + V_0)}} \quad \text{with} \quad k = \frac{\mu\rho}{2\epsilon A^2} \quad (6.1)$$

where C_P represents a voltage-independent parasitic capacitance, V_0 is the built-in voltage of the diode, μ is the holes mobility, ρ is the substrate resistivity, ϵ is the silicon dielectric constant and A is the area of a pixel.

The expected value of k can be estimated using the following design parameters

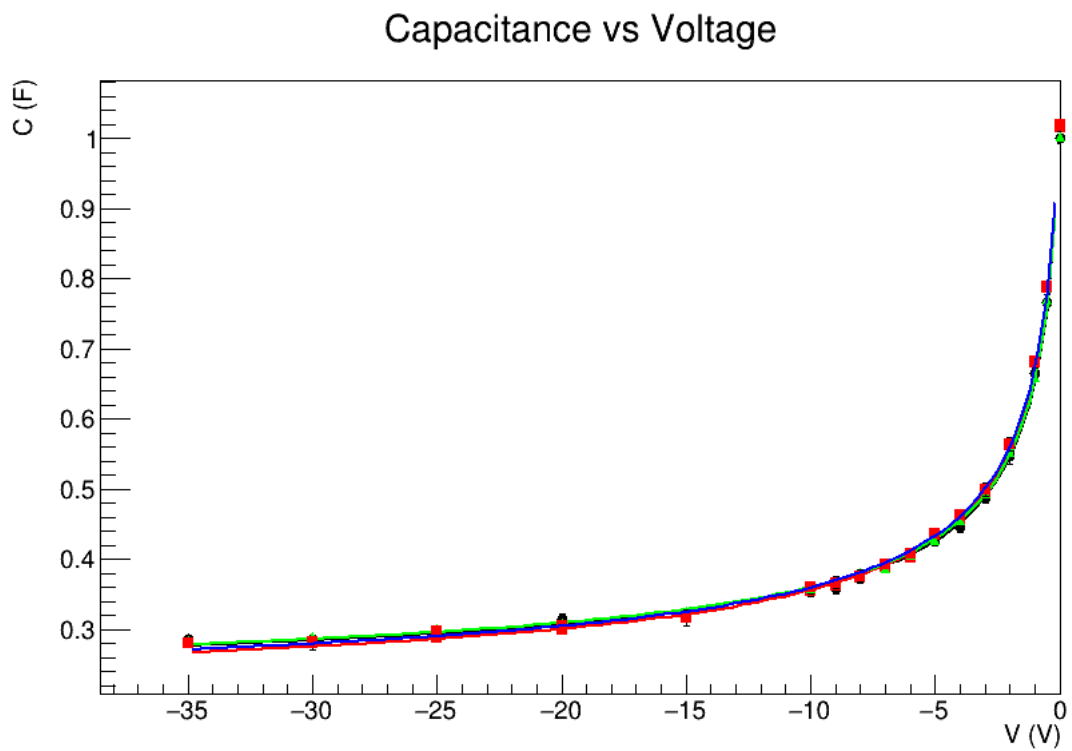


Figure 6.6: Capacitance vs Voltage measurements for the 4 passive diodes in the KC53AB chip.

	D1	D2	D3	D4
C_P (pF)	(0.192 ± 0.007)	(0.169 ± 0.007)	(0.186 ± 0.007)	(0.172 ± 0.007)
k ($V^{-1}pF^{-2}$)	(3.6 ± 0.3)	(2.8 ± 0.2)	(3.1 ± 0.2)	(2.7 ± 0.2)
V_0 (V)	(0.30 ± 0.16)	(0.42 ± 0.11)	(0.42 ± 0.10)	(0.45 ± 0.10)

Table 6.1: Passive diodes parameters extracted from the fits to the CV measured curves.

of the substrate, where only the error on the resistivity is mentioned since it is the dominant one:

- $\epsilon = 1$ pF/cm,
- $\rho = (125 \pm 25)$ Ω cm (BCD8 technology specifications),
- $\mu = 450$ $\text{cm}^2\text{V}^{-1}\text{s}^{-1}$,
- $A = 240 \times 40$ μm^2 (actual area of the diode, as mentioned in the previous chapter)

and corresponds to:

$$k = (3.05 \pm 0.6)V^{-1}pF^{-2} \quad (6.2)$$

Fits were done leaving C_P , k and V_0 as free parameters. The results of the fits are reported in table 6.1.

The values of k obtained from the fits are in accordance with the expected one considering the experimental precision, therefore the values of the real characteristics of the substrate can be regarded as close to the design ones. Also the values of parasitic capacitance and built in voltage are coherent with each other and the expected values.

The depletion depth of the chip at a given bias voltage V_B can be evaluated by

the following equation, as long as the sensor is approximated to a parallel-plated capacitor

$$d = 2\epsilon \frac{A}{C(V_B) - C_P} \quad (6.3)$$

The values of the depletion depth of the different passive diodes at operating bias $V_B = 50$ V are reported in tab 6.2.

	D1	D2	D3	D4
d (μm)	(24 ± 1)	(22 ± 1)	(23 ± 1)	(22 ± 1)

Table 6.2: Measured depletion depth of the different passive diodes at $V_B = 50$ V.

These values can be compared with the value expected from the design characteristics of the substrate:

$$d \simeq \sqrt{2\epsilon\rho\mu(-V_B + V_0)} = (23 \pm 1)\mu\text{m} \quad (6.4)$$

The values are in agreement with the experimental precision, therefore this is an ulterior confirmation that the sensor behaves as expected.

The expected signal of a MIP can be evaluated from the depletion depth, given that the mean energy loss in silicon is about 3.87 MeV/cm and the generated number of electron/hole pairs in a 23 μm layer is $N_{e/h} = 2500$ (eq (3.1)). The collection time can be estimated from the holes speed ($v = \mu E = \mu V_B/d$):

$$t_{coll} = \frac{d}{v} = \frac{d^2}{\mu V_B} \simeq 0.24\text{ns} \quad (6.5)$$

The current intensity is then calculated using the following equation:

$$I = \frac{Q}{t_{coll}} \simeq 1.7\mu\text{A} \quad (6.6)$$

Therefore, the expected signal of a MIP is a 1.7 μA current pulse 0.24 ns long.

6.3 Studies on radiation resistance

IV and CV scans were also carried out on a different chip that was subjected to 4 rounds of irradiation at Laboratori Nazionali del Sud in Catania. These measure-

ments were actually performed before the ones mentioned in the previous section, due to the laboratory allotted time. These analyses were carried out to evaluate the chip behaviour after increasing doses of absorbed radiation. The KC53AB chips to be tested were positioned in front of the cyclotron test beam called “Cyclope” which accelerates and drives protons to 62 MeV. The beam shape, spread and alignment were evaluated by means of a gafchromich EBT film placed in front of the chip to be tested at the beginning of the irradiation campaign (fig. 6.7). Gafchromich films, widely used in medical dosimetry, are colourless and transparent before radiation exposure, and change progressively to darker colour with exposure. They can be read with a film scanner: the optical density has a known logarithmic dependence on the absorbed dose, so that the beam profile can be reliably extracted. Total dose cannot be evaluated in our case because it is far beyond the film saturation.

In order to evaluate the actual dose received by the chip two kinds of information were used: beam-current values measured at regular intervals by the cyclotron team by deviating the beam into a Faraday cup, and monitoring-data based on beam effects on a 15 μm tantalum foil placed before the beam exit in air.

The measurements by the cyclotron team are used to perform a calibration of the tantalum data. The absorbed dose is then calculated through the following formula:

$$DOSE[Rad] = \varphi \left(- \frac{dE}{\rho dx} \right) \quad (6.7)$$

where φ is the fluence rate of protons, ρ the sensor density and $-dE/dx$ the mean energy loss per distance travelled of protons in silicon. The fluence φ can be measured through the beam-current data, given by the tantalum monitor, and the profile of the beam onto the chip, given by the gafchromich film. The precision on the estimation of the total dose is about 20%, mainly due to the calibration of the tantalum data.

The increasing values of dose absorbed by the chip where 10, 44, 90 and 119 Mrad. To confront these values with the requirement for the ATLAS tracker of HL-LHC, the equivalent 1 MeV n_{eq}/cm^2 fluences ϕ can be evaluated with the

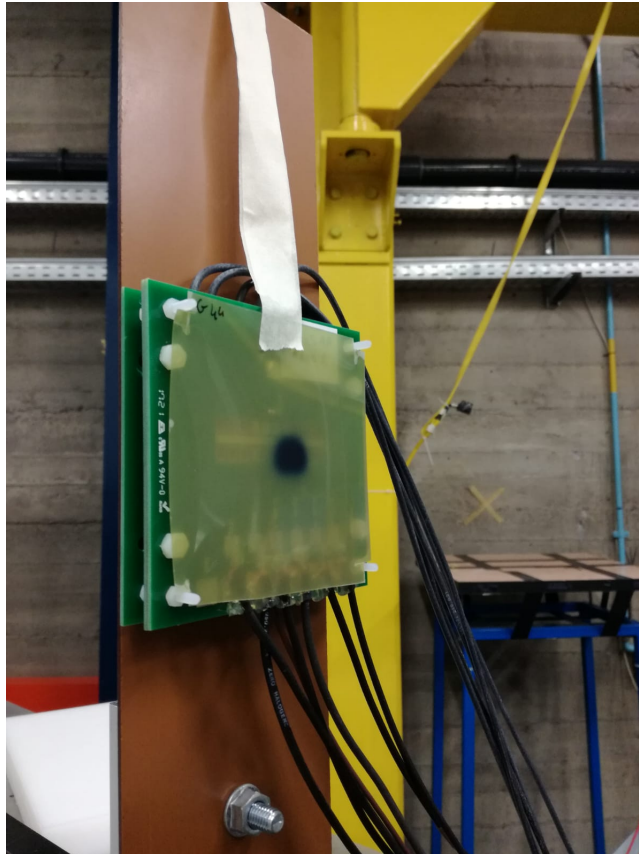


Figure 6.7: PCB hosting the KC53AB chip with a gafchromich film in front. The spot indicates the position, dimension and intensity profile of the beam.

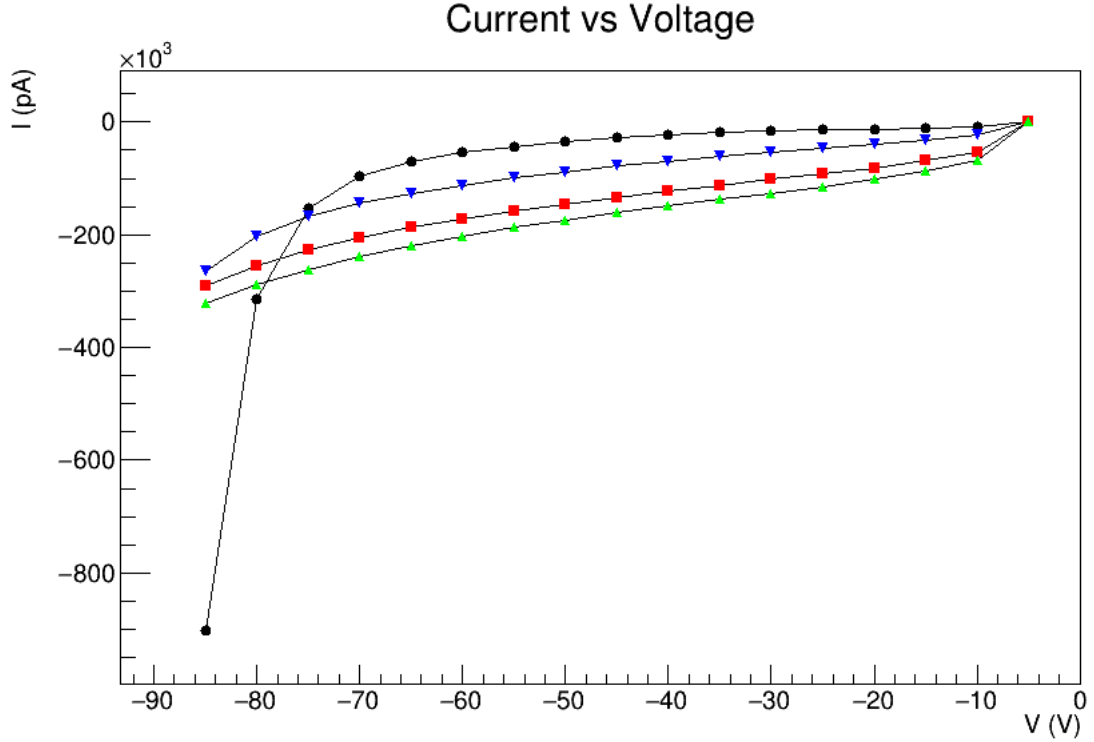


Figure 6.8: IV curves for one of the passive diodes, after doses of: **black** 10 Mrad, **green** 44 Mrad, **red** 90 Mrad, **blue** 119 Mrad.

following equation:

$$\phi = \frac{DOSE[Rad]}{1.6 \cdot 10^{-8} \cdot NIEL} \quad (6.8)$$

where the NIEL for 1 MeV neutron = $2.037 \text{ keV} \cdot \text{cm}^2/\text{g}$. A total value of $\approx 3 \cdot 10^{15} \text{ n}_{eq}/\text{cm}^2$ is obtained for 119 Mrad of dose, which is in excess of the amount of irradiation expected in the outer layer of ATLAS ITK during HL-LHC operations.

A Keithley 6517A electrometer and a HP 4280A CV meter were used to perform IV and CV scans between the irradiation periods. They were connected to the PCB with diagrams similar to the ones illustrated before. The measurements were performed only on one of the passive diodes since the allotted time was limited and it was expected that the passive pixels behave similarly.

Run	1	2	3	4
C_P (pF)	(0.413 ± 0.002)	(0.440 ± 0.003)	(0.603 ± 0.003)	(0.608 ± 0.003)
k ($V^{-1}pF^{-2}$)	(0.55 ± 0.01)	(14.0 ± 1.2)	(45 ± 8)	(65 ± 13)
V_0 (V)	(0.803 ± 0.08)	(0.84 ± 0.07)	(0.8 ± 0.2)	(0.8 ± 0.2)

Table 6.3: Diode parameters as extracted from fits to CV curves after absorbed doses of: 10 Mrad (run 1), 44 Mrad (run 2), 90 Mrad (run 3) and 119 Mrad (run 4).

IV curves after absorbed doses of 10, 44, 90, and 119 Mrad are shown in fig. 6.8. A clear increase of breakdown voltage with respect to the pre-irradiation measurement is observed after the first value of absorbed dose. The breakdown is not reached after the other irradiation periods since it is beyond the range of the instrument (-80 V). An increase of the reverse current is observed as well. These effects are expected as radiation removes acceptors, modifies the doping of the silicon and therefore the resistivity of the substrate, as was explained in chapter 3.

CV curves after absorbed doses of 10, 44, 90, and 119 Mrad are shown in fig. 6.9, and are fitted using the formula (6.1) described in the previous section. Fit results are collected in table 6.3. The parasitic capacitance increase in the last two runs can be explained with a change in the cable connections which was done during the pause between irradiation runs, while the built-in voltage roughly remains the same. A reduction of junction capacitance can be also observed in fig. 6.9, expected with irradiation which causes the removal of the acceptors. The parameter k is observed to largely increase with respect to the values obtained before irradiation. This result calls for further investigations, since the values of the parameter k may imply some degradation of the depletion region. Having being measured on just one pixels, strong conclusions cannot be drawn yet.

Capacity vs Voltage

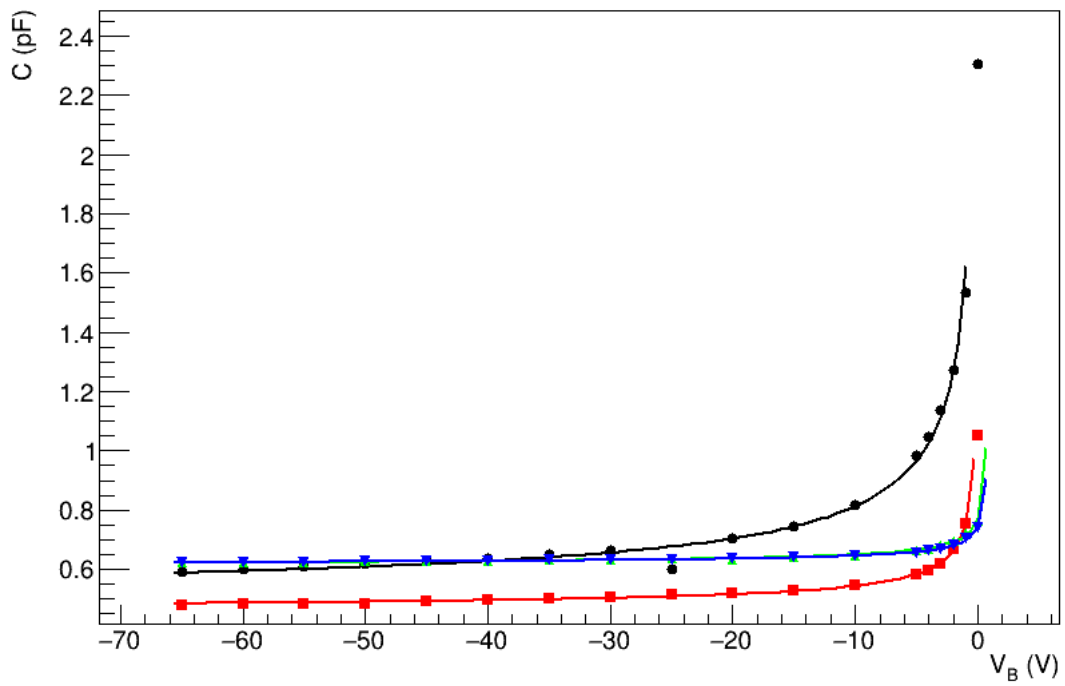


Figure 6.9: CV curves for one of the passive diodes, after absorbed doses of: **black** 10 Mrad, **green** 44 Mrad, **blue** 90 Mrad, **red** 119 Mrad.

Chapter 7

Tests on TowerJazz Investigator

In this chapter a characterisation of the TowerJazz investigator is presented. I personally carried out all the measurements included here, both at the CERN Testbeam facility and in the ATLAS Pixel Laboratory under the supervision of professor Heinz Pernegger. Measurements of efficiency, collected charge, cluster size and timing have been performed, before and after the investigator was irradiated. The main purpose of these measurements was to certify that TowerJazz technology can be reliably deployed for the outermost layer of the ATLAS Inner Tracker that will be used at HL-LHC.

7.1 Beam test setup

A TowerJazz Investigator (device under testing, DUT), together with a silicon pixel reference telescope, was positioned in front of the CERN SPS test beam line H8. The beam is made of 180 GeV pions, whose trajectories are recorded and reconstructed in the reference telescope and extrapolated to the DUT. Data have been taken in runs (periods of time of uninterrupted acquisition) of approximately 8 hours each. Before each run an alignment was performed, to adjust the positions of the telescope and the DUT with respect to the centre of the beam so as to select a specific Region of Interest containing the pixels to be tested.

7.1.1 Telescope and DUT setup

The Silicon Beam Monitor (SMB) telescope, shown in figure 7.1, consists of two arms each formed by three detector planes. Each detector plane consist in a $200\ \mu\text{m}$ thick n^+ -in-n planar pixel silicon sensor, of the size of $2\times 2\ \text{cm}^2$ segmented into 320 passive pixels, each one with pitch of $50\times 250\ \mu\text{m}^2$. In order to ensure a good spatial resolution in the X and Y directions the planes can be rotated around the beam axis (the beam is parallel to the Z-coordinate). A baseplate holds the two telescope arms as well as the DUT. Each of the three telescope planes in each arm can be positioned freely along the 40 cm long basement and tilted around the short pixel direction. The DUT is positioned inside a box with a slot in which dry ice can be stored, in order keep the device at a temperature of $-30^\circ\ \text{C}$ during runs.

The telescope readout chip consists of FE-I4 [12] chips bump-bonded to the silicon sensors. Following a trigger signal, the detected hits and a timestamp are stored in memory cells shared by four pixels. Each memory cell stores up to 5 events which are retained for a certain latency period and erased when a further hit is detected. The maximum hit rate that can be sustained is $400\text{MHz}/\text{cm}^2$.

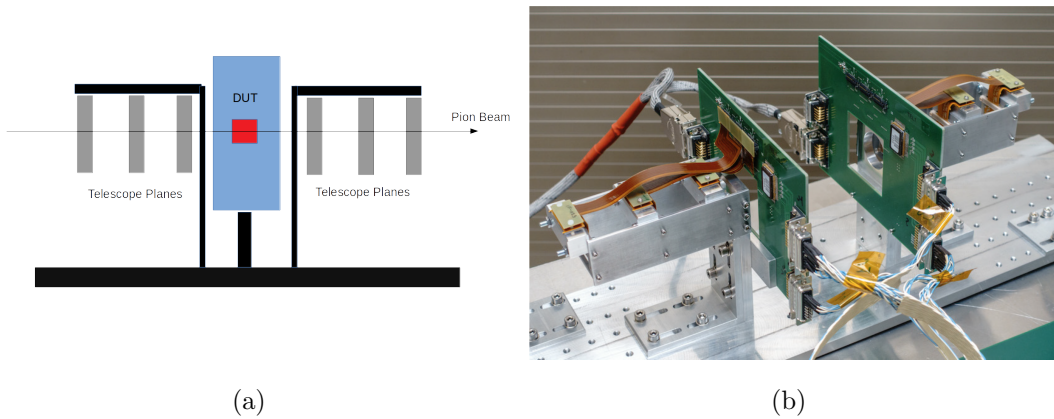


Figure 7.1: (a) Diagram and (b) photo of the SMB telescope. It is formed by two arms, each with three sensor planes, bump-bonded to FE-I4 chips, which in turn are connected to the HSIOs boards.

The Telescope Data Acquisition (DAQ) system consist in three parts: a High

Speed I/O (HSIO) board, a Reconfigurable Cluster Elements (RCEs), and a PC running a custom data acquisition framework.

The HSIO is a custom-made general-purpose readout board based on a Xilinx Virtex-4 FPGA. It has a large number of I/O channels that can both send and receive data to and from the higher level processing RCEs. It implements the command and data protocols of the FE-I4, relays commands from the RCE and buffers data from the front-end. It also generates the clock, that is distributed to all the modules. The HSIO permits to define regions of interest (ROI, fig.7.2) any size on the plane, which is especially useful for DUTs smaller than the acceptance of the telescope. The logical OR of the hits in the pixels that belong to the ROI (HitOR functionality of the FE-I4) is evaluated, and the global trigger is given when a minimum number of planes (in our case 2) records at least one hit in its ROI. The global trigger is directly fed into the FPGA and then to the DUT. The event data are sent via optical fibres to the RCE. RCE is a generic computational

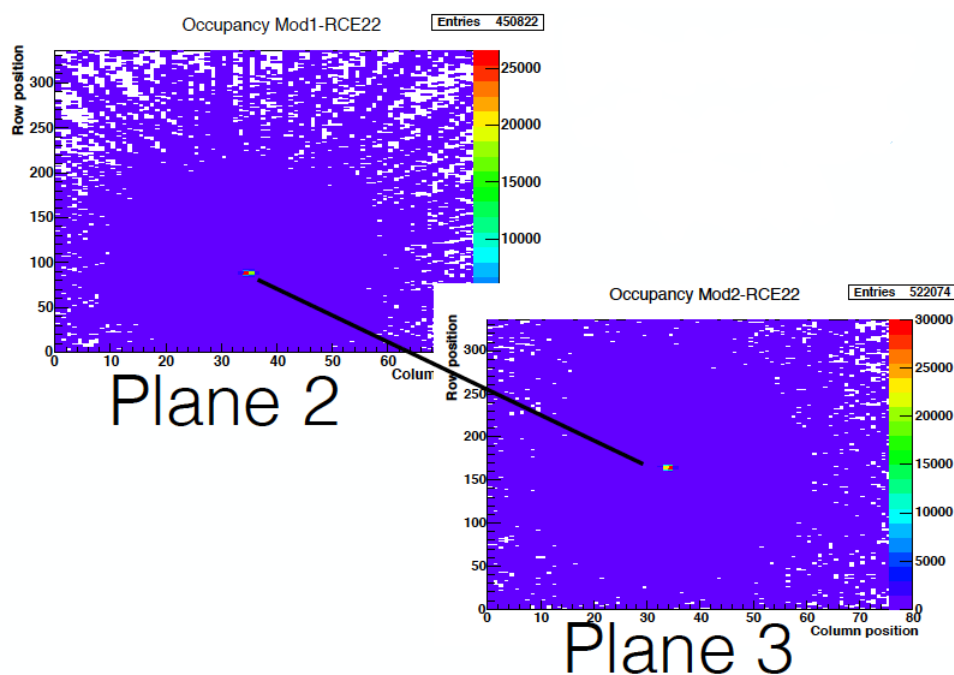


Figure 7.2: Region of Interest. The picture shows the occupancy of the two selected pixels subsets inside the plane of the telescope.

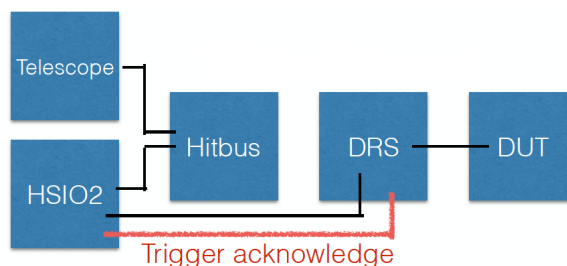


Figure 7.3: Simple trigger scheme for DUT data taking.

unit based on a System-On-Chip (SOC) which can handle up to 24 lines of high-speed serial I/O at lane speeds in excess of 40 Gb/s. The core is a 350MHz PowerPC processor running an RTEMS Real-Time kernel. The RCE configures the HSIO and sends commands to the interfaced front-ends.

The DAQ PC runs two acquisition software, one for the telescope and one for the DUT. The telescope software allows to set configurations for each plane as well as global parameters like trigger mode and delays. During data taking an online monitor provides real-time hit maps, correlation plots between the hit positions of neighbouring planes, and timing and charge information. In addition the monitoring software for the DUT shows the waveforms as recorded for each channel. It also allows to change channel parameters like delays and thresholds.

The trigger scheme to synchronise the telescope and the DUT can be seen in fig. 7.3. The trigger signal generated by the telescope is delivered directly to the DUT DAQ system (DRS). If this system is ready for data taking and accepts the trigger it sends a signal to the RCE to read out the telescope.

The telescope can reach a trigger rate of approximately 100 kHz. The positions of the hits in the six planes of the telescope are then fitted using the Judith [14] software which will be explained later. The spacial resolution of the telescope is estimated by the error of the track fit parameters projected to the position of the DUT. If a digital hit information is available on the DUT, the resolution only depends on the position of the planes and the telescope pixel granularity, and has been estimated to be approximately $\sigma \simeq 9\mu m$ for the X and Y directions.

The TowerJazz Investigator is glued and wire-bonded to a carrier board de-

signed by the ALICE group. All inputs and outputs except for the HV supply are routed to a PCIe connector. The bias voltage is applied using a separate LEMO connector in the range of 0V to -6V to stay below the diode's breakdown region. In addition to a supply voltage of 1.8V for the active part of the pixels, other inputs have to be provided for the operation of the Investigator: an active transistor reset, a reset voltage of 1 V and a logical reset pulse to operate the transistor are needed. Furthermore, four constant currents are needed by source followers (voltage buffers) in the analog pixel circuit.

In order to provide all needed supply voltages and signals, a combination of a Multi-IO (MIO) board and a General Purpose Analog Card (GPAC) is used. A custom-made adapter board has been designed to connect the investigator carrier board and the GPAC. All inputs except the HV supply are generated on the GPAC card. In addition a logical reset veto is generated by the FPGA of the MIO board. This signal defines a time window around the reset pulse, during which triggers are vetoed. The adapter board can be equipped with up to 25 LEMO connectors. Each connector can be used to access the analog signal given by one of the pixels in the selected matrix. A matrix is composed by a grid 8×8 pixel, however the connectors form only a 5×5 grid resembling the position of the pixels. The analog output signals of the pixels are connected to a fast DRS4 Evaluation Board. The DRS4 is a USB oscilloscope equipped with four channels and capable of 2GS/s. One channel is used for the reset veto created by the FPGA on the MIO board in order to prevent triggering on the reset response itself as shown in figure 7.4: here, the red curve is the waveform recorded by the oscilloscope. The reset veto in black indicates two time frames with open reset transistor. The pixel responds to resets with very deep spikes. Vetoing intervals around resets enables to trigger only on hits, which appear as steps proportional to the collected charge as seen between reset intervals.

The remaining three channels can be used for signals. The signals are amplified using inverting CIVIDEC C1 broadband amplifiers. By doing so, resolution and signal/noise separation can be improved, since the amplification occurs only on a finite band, while our noise is equally present on all frequencies. For our mea-

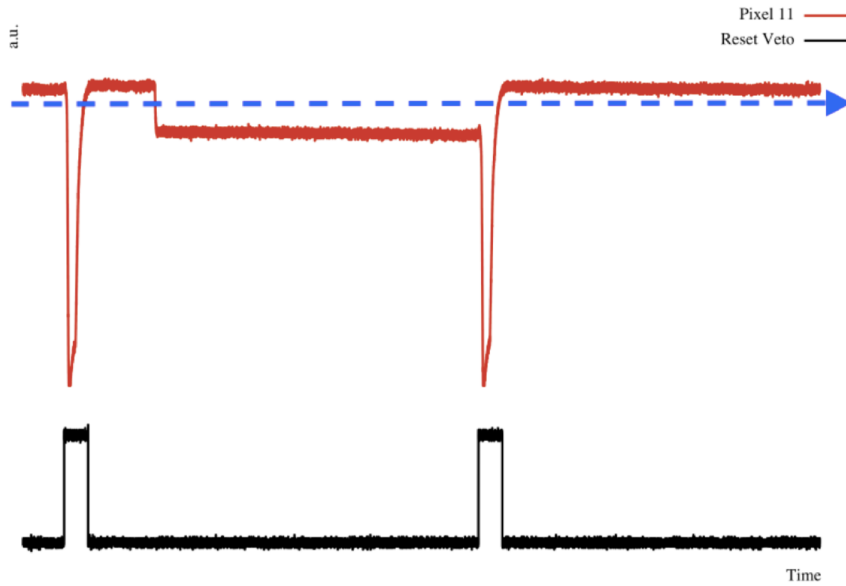


Figure 7.4: Pixel response (univerted, red) and reset veto (black).

surements, 4 DRS were available, therefore the number of pixels that was possible to read is 15. However only 4 CIVIDEC C1 amplifiers were usable, thus only the signal of 4 pixels were amplified. It was apparent during the analysis that only the signals from the amplified pixels could be proficiently separated from the noise, and in the end only these pixel were considered.

The waveforms, recorded by the DRS4 in binary format, are first analysed using an in-house software framework known as *tbConveter*. The analysis includes:

- reading in the binary format of the DRS4 waveforms;
- using Fourier transform and rough cuts to separate hits from noise;
- fitting the waveform with a function that will be described later, to extract the signal charge, its duration (time-over-threshold, ToT) and the signal time with respect to the trigger.

The fit parameters are then analysed together with the telescope data using the *Judith* software.

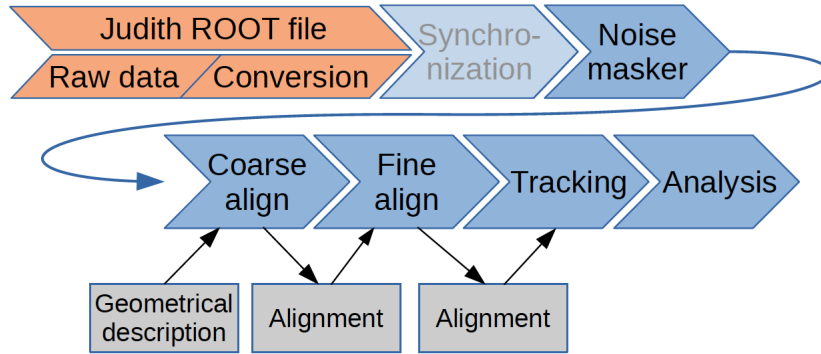


Figure 7.5: Scheme of Judith reconstruction process.

7.2 Data reconstruction

7.2.1 Beam track reconstruction in the telescope

Telescope raw data are analysed using the reconstruction software Judith. Judith is a framework written in C++, which consists in multiple algorithms for data handling, synchronisation, setup description, reconstruction and analysis. In order to be ready for analysis, the raw data have in fact to undergo several processing steps. Raw data are stored in a file in ROOT format, with geometry description and framework parameters given in text configuration files. The full process can be seen in figure 7.5.

Preprocessing and clustering The first step is producing a noise mask that calculates per-pixel occupancies and excludes from further analysis the pixels that exceed a certain counting threshold. Next, a synchronisation algorithm joins telescope and DUT events based on their timestamps. If more than one pixel is above threshold when a particle hits the DUT, a cluster of pixels is formed. Judith converts hits into clusters before further processing. Beginning with random seed hits, a recursive algorithm groups all neighbouring hits. Overlapping clusters cannot be detected and are considered as one. The actual position of the hit is then calculated as the geometric mean of the pixel positions in the cluster.

Alignment There are two main processes in the alignment package and both are performed for the telescope data. The relative position of the telescope planes of the test beam setup are entered in a configuration file, as well as their rotation.

A first coarse alignment calculates 2D inter-plane hit correlation distributions, which has to be a straight line in case electric or magnetic fields aren't present. Given a perfect alignment the line would cross the origin (center of each pixel) with a slope equal to the ratio of the pixel pitches. Shifts between the planes are therefore deduced from the offset of the line from the origin and rotations from the deviation of the measured to the calculated slope. The first plane is fixed as point of reference and planes are only aligned to their direct neighbours to minimise the influence of scattering.

Then, a fine alignment calculates track residuals for precise positioning of the planes, as the distance between the projected track position and the position of the associated cluster on a plane. The correction to the position of the plane is then calculated from the residual and the hit position on that plane. As the track position is directly influenced by the current alignment of the telescope, the plane under investigation is always excluded from track fitting, forming unbiased tracks.

Track reconstruction This procedure is done event by event. Starting from a seed cluster, the track reconstruction algorithm searches for clusters on consecutive planes within an user-defined cone angle. The angle is chosen taking into consideration scattering effects on the planes themselves. The algorithm initially assumes that the track is parallel to the telescope's longitudinal direction, but this is modified as clusters are added to the track. If multiple candidate clusters are found on a plane, the track bifurcates and further searches continue for each cluster.

Candidate tracks with the largest number of clusters are kept, straight-line fits are performed and the one with the smallest χ^2 is selected. Clusters that have been assigned to the selected track are excluded from further searches.

The algorithm copes well with large scattering angles in case of low track density (and thus a large enough separation between tracks), so these clusters are

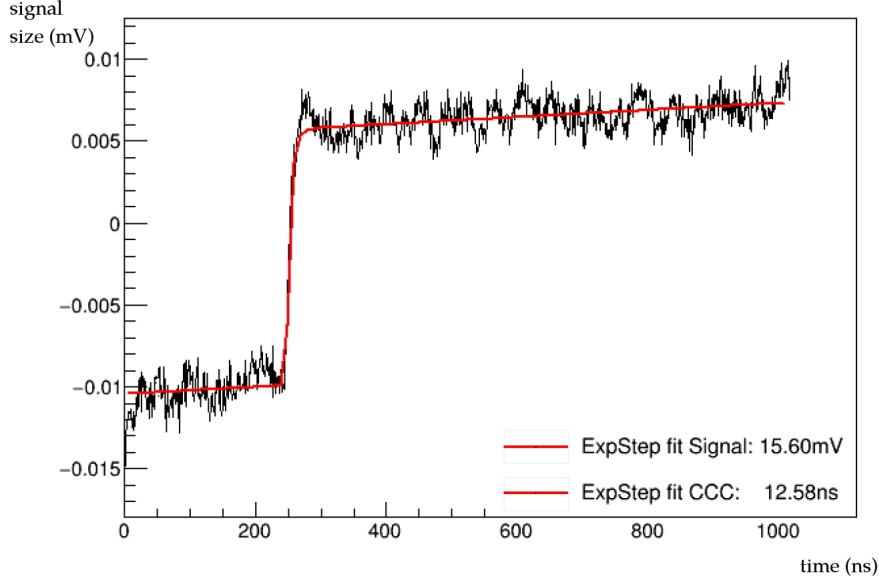


Figure 7.6: Waveform recorded and fitted with the equations (7.1a) and (7.1b).

correctly assigned to their corresponding track.

The χ^2 fit is then used to filter events where beam particles are largely deviated by multiple scattering or nuclear interactions with the telescope planes.

7.2.2 Signal reconstruction on the DUT

For each hit in the telescope the full waveform in the DUT is recorded ($1 \mu\text{s}$) and then fitted. An example waveform with the applied fit is shown in figure 7.6. The fitted function is given in the equations (7.1a) and (7.1b):

$$t \leq t_0 \quad f = a + m \cdot (t - t_0) \quad (7.1a)$$

$$t \geq t_0 \quad f = a + m \cdot (t - t_0) - b \cdot \left(e^{-\frac{t-t_0}{c}} - 1 \right) \quad (7.1b)$$

where a and m are the offset and the slope of the line used to fit the leakage current, t_0 is the time between the trigger and the signal rise, b is the signal size or amplitude (mV) proportional to the deposited charge and c is the rise time (ns), i.e. the time between 10% and 90% of the signal amplitude. Therefore the hit is

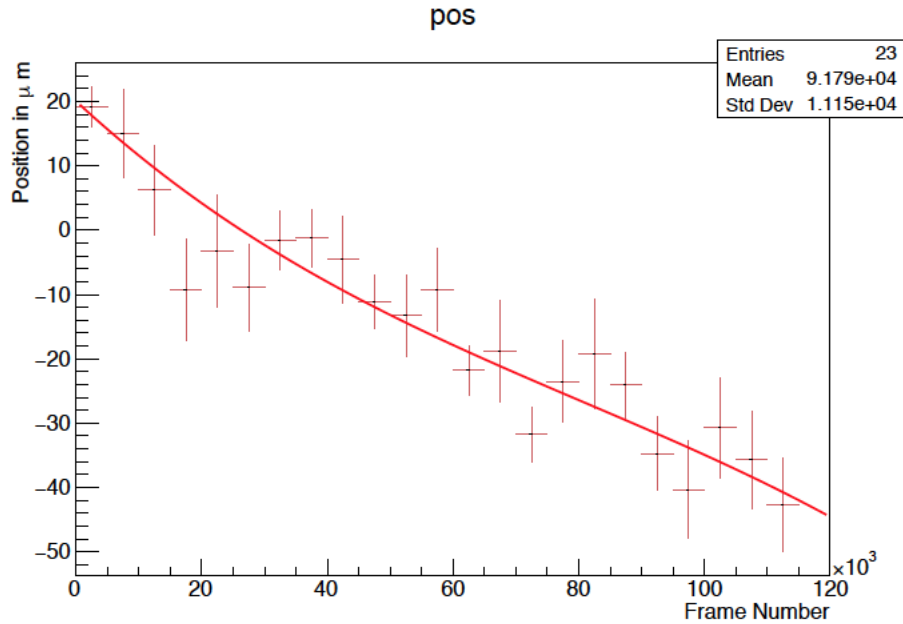


Figure 7.7: Position of the DUT (X coordinate) with respect to the telescope, during a run. The observed variation is due to the evaporation of the dry ice.

described by adding an exponential function for $t > t_0$ to the straight line used to fit the leakage current.

The results of the fit are stored in flat ROOT [3] Ntuples. The hits on the DUT are correlated to the reconstructed tracks with processes similar to the ones explained before. Each run is individually aligned to correct for movements between the telescope planes and the DUT due to the fact that the DUT box is cooled with dry ice to -30°C and changes in its x and y position over the course of 12h runs are observed. They are likely to come from thermal expansion and are corrected by the offline analysis. The mean hit residuals for the x and y positions are fit in bins of framenumbers and/or timestamps, the DUT position is then corrected by the fitted function. An example of the movement of the DUT in the X-direction with respect to the telescope planes is shown in fig. 7.7.

Three main cuts are operated on the hits to remove the noise: the first requires that the hit occurs within $\pm 60\text{ns}$ around the telescope trigger time; the

second disposes of all the hits that are below the threshold amplitude of 4mV; finally the charge collection time is required to be lower than 250ns.

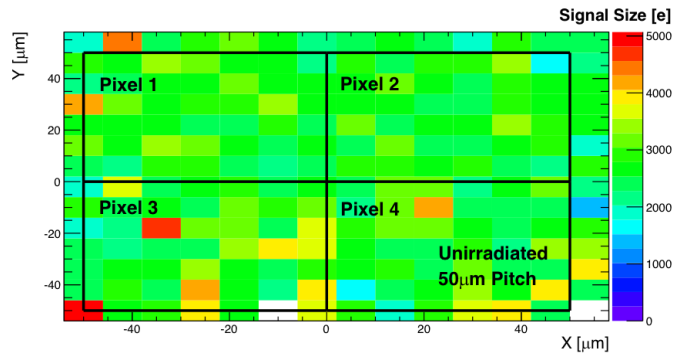
7.3 Data analysis and result

The measurements at the Test Beam facility were carried out on two Investigator samples, one unirradiated and the other one irradiated at $10^{15}n_{eq}/cm^2$ [16]. The sample was irradiated with 1MeV neutron in Ljubljana (TRIGA). Only 2x2-pixel subsets in the centre of the considered matrices were measured, since only the signals coming from four pixels were amplified. The measurements of the unirradiated sample were carried out only on the matrix with $50 \times 50 \mu m^2$ pixel pitch, while for the irradiated one, matrices with $50 \times 50 \mu m^2$, $30 \times 30 \mu m^2$ and $25 \times 25 \mu m^2$ pixel sizes were studied.

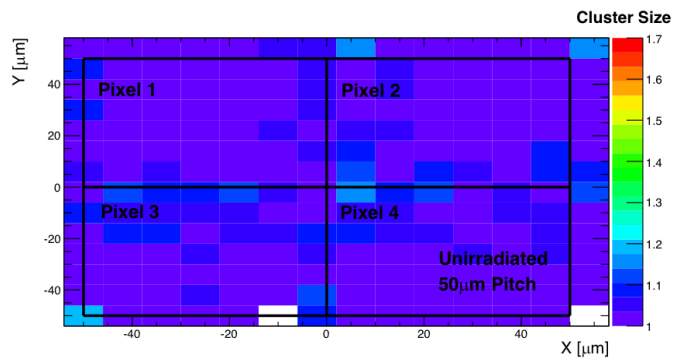
7.3.1 Cluster and charge

Pixel clusters are defined as the combination of nearby pixels that register a signal. This is due to the charge sharing phenomenon. The extrapolated hit position on the DUT from the telescope track reconstruction was used to measure clusters and their charge. The cluster charge is calculated as the sum of amplitudes for all its pixels. The signal to noise ratio (SNR) is calculated as the ratio between the standard deviation of the noise distribution, i.e. the offset of the fitted leakage current curves, which follows a normal distribution, and the most probable values (MPV) of the Landau distribution governing the amplitude of the signals. Plots 7.9, 7.8, 7.10, 7.11 show the cluster charge converted to number of generated electrons, which was done with a calibration explained later, clusters size, i.e the mean number of pixels which form the clusters and the signal to noise ratio for the matrices mentioned above. Plots (a) show the clusters charge as a function of the hit position. Figures (b) portray the clusters size in units of number of pixels above threshold. Charge sharing along the pixel edge is visible through an increased cluster size the X/Y axis. Figures (c) show the amplitude distribution of the signals, as well as the electronic noise distribution. The Signal-to-Noise

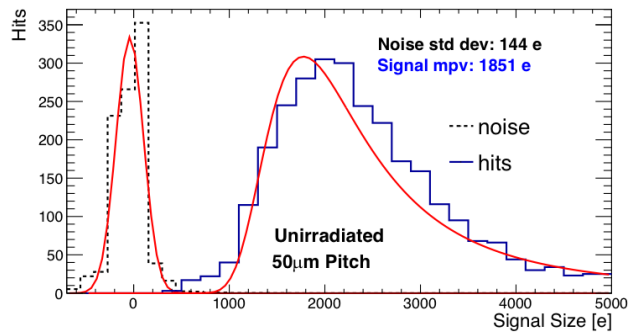
Ratio is 13:1 for the unirradiated $50 \times 50 \mu m^2$, and is 5:1 for the irradiated one of the same size. For smaller pixel pitch matrices, which also have smaller spacing between the n-well and the p-well, the SNR is larger: 39:1 (25x25, $3 \mu m$ spacing) and 33:1 (30x30, $3 \mu m$ spacing).



(a)

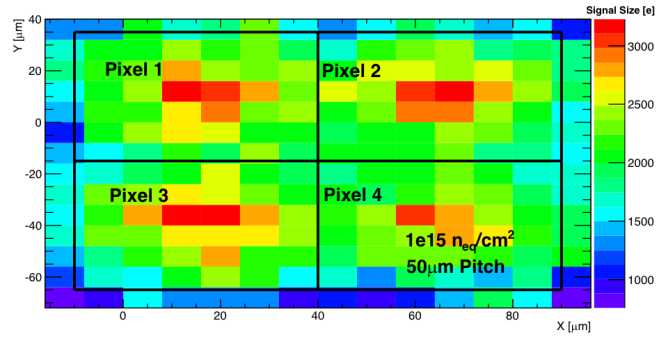


(b)

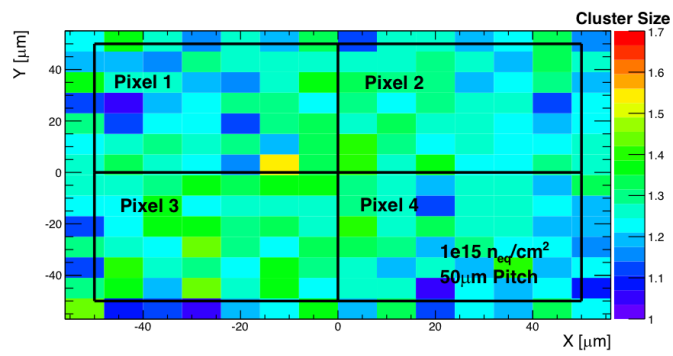


(c)

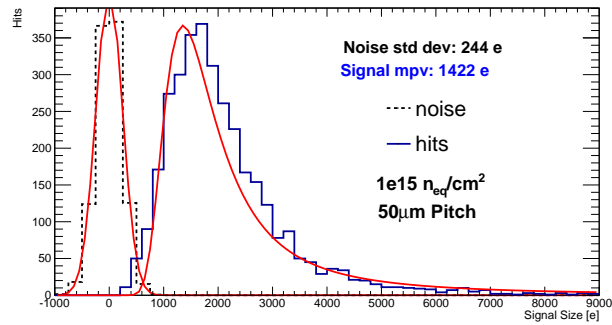
Figure 7.8: (a) Charge (in number of electrons), (b) cluster size and (c) S/R ratio of the pixels measured on the $50 \times 50 \mu m^2$ sub-matrix of an unirradiated Investigator sample.



(a)

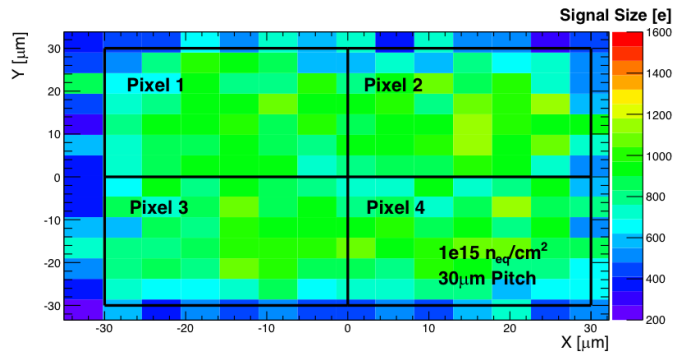


(b)

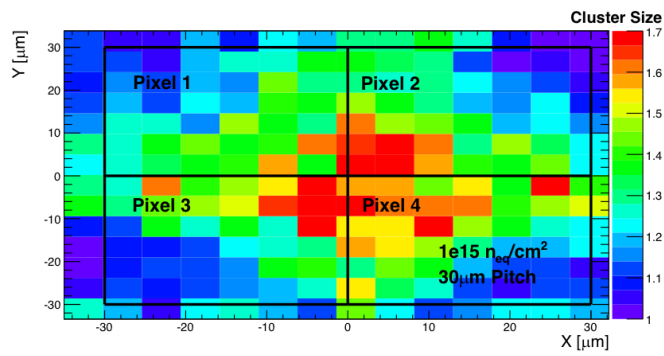


(c)

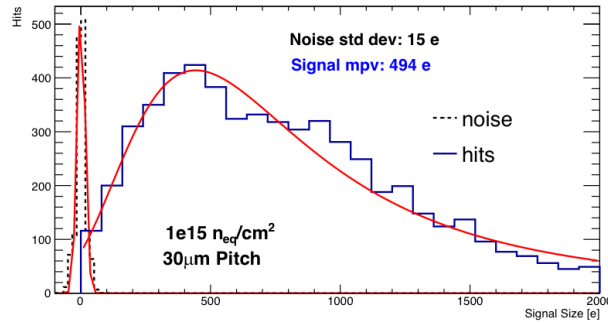
Figure 7.9: (a) Charge (in number of electrons), (b) cluster size and (c) S/R ratio of the pixels measured on the $50 \times 50 \mu m^2$ sub-matrix of an irradiated Investigator sample.



(a)

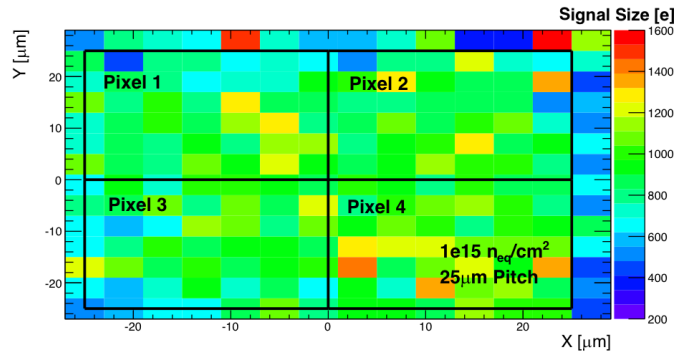


(b)

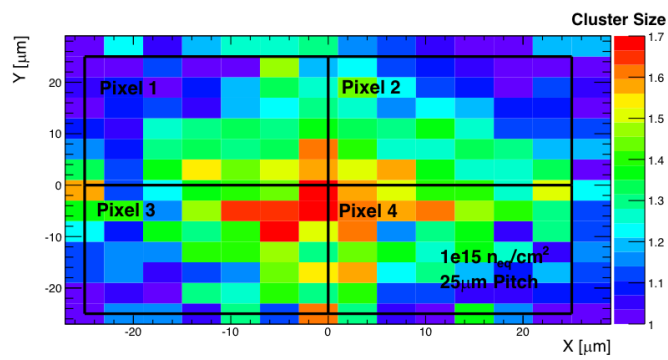


(c)

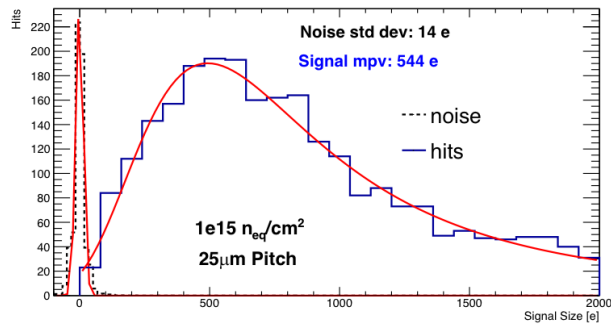
Figure 7.10: (a) Charge (in number of electrons), (b) cluster size and (c) S/R ratio of the pixels measured on the $30 \times 30 \mu m^2$ sub-matrix of an irradiated Investigator sample.



(a)



(b)



(c)

Figure 7.11: (a) Charge (in number of electrons), (b) cluster size and (c) S/R ratio of the pixels measured on the $25 \times 25 \mu m^2$ sub-matrix of an irradiated Investigator sample.

Figure 7.12 shows the cluster size for the unirradiated $50 \times 50 \mu m^2$ pixel matrix

(blue), for the $25 \times 25 \mu m^2$ pixel matrix after $10^{15} n_{eq}/cm^2$ (red) and for the $35 \times 35 \mu m^2$ pixel sensors after $10^{15} n_{eq}/cm^2$ (green). While single-pixel clusters dominate the response of the $50 \times 50 \mu m^2$ pixel sensors (mean 1.06), we find approximately 30% of 2-pixel clusters on the $25 \times 25 \mu m^2$ or $30 \times 30 \mu m^2$ pixel matrices (mean 1.35 and 1.37 respectively). In addition to the pixel pitch, the cluster width is influenced by the spacing between n-well and p-well, which is $3 \mu m$ for the $30 \times 30 \mu m^2$ and $25 \times 25 \mu m^2$ pixels, while it is $18.5 \mu m$ for $50 \times 50 \mu m^2$ pixels.

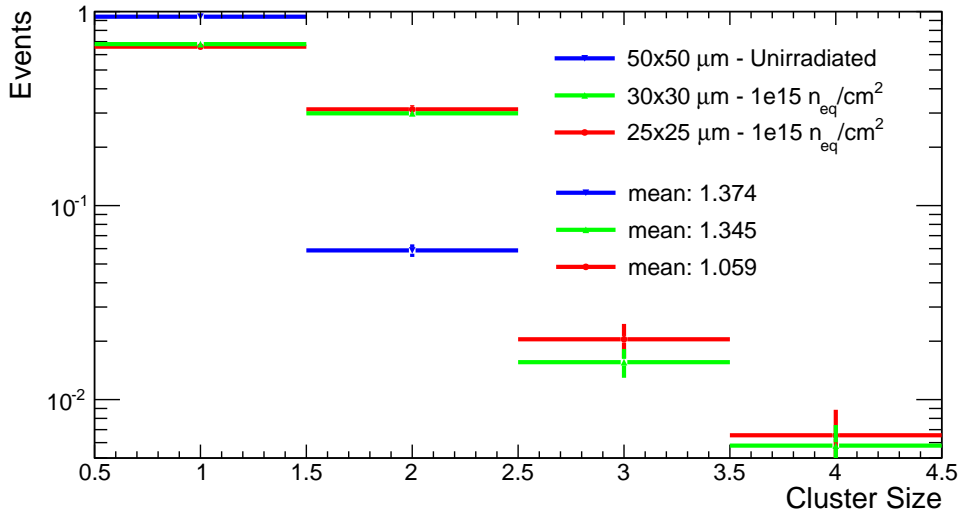


Figure 7.12: 1-D plot of the cluster size of the different sub-matrices of an irradiated and an unirradiated Investigator sample

7.3.2 Signal rise time

Figure 7.13 shows the signal rise time as extracted with the fit in eq. 7.1, for the four pixel matrices we analysed. The MPV of the distribution is around 40 ns for the unirradiated $50 \times 50 \mu m^2$ pixel matrix, and it is significantly smaller (15-20 ns) for the irradiated $25 \times 25 \mu m^2$ and $30 \times 30 \mu m^2$ pixel sensors, which have also a smaller spacing ($3 \mu m$). The rising time for the irradiated $50 \times 50 \mu m^2$ pixel sensor is longer than the other ones, with the consequence that some of the slower hits at the edges of the pixels might have been cut by the analysis. This for sure

decreased the detection efficiency, as will be shown in the following section. Such an effect is specific of the sample under study, since all measurements done with this particular one are affected in the same way, while other samples did not show this characteristic.

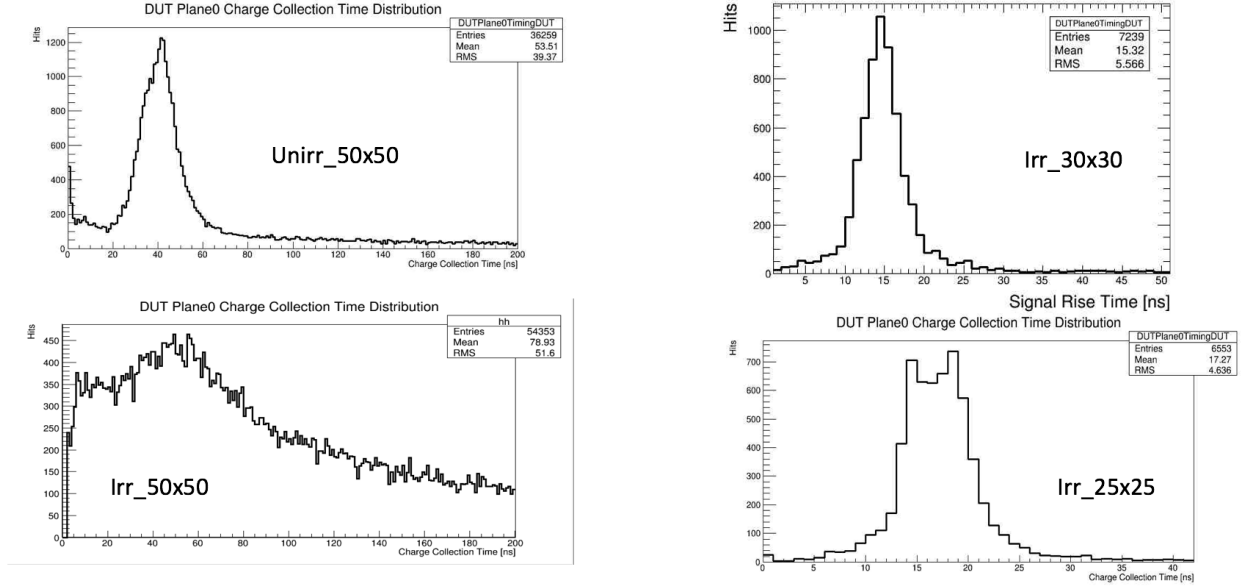


Figure 7.13: Signal rise time in the different matrices that have been studied.

7.3.3 Efficiency measurements

Since in each event only 4 pixels are read, corresponding to an acceptance of $50 \times 50 \mu m^2$ and $100 \times 100 \mu m^2$ for $25 \mu m$ and $50 \mu m$ pixel pitches respectively, edge effects due to the telescope resolution ($9 \mu m$) influence the calculation of the detection efficiency. The positions of the hits are smeared out by the telescope resolution, therefore there's the need to apply a correction. The correction is obtained by simulating what the sub-matrix efficiency would look like in this setup if the sensor was 100% efficient. This is shown in fig. 7.14. Figure 7.14a shows the probability that a track actually crossed the sensor in the 4-pixel area with $50 \times 50 \mu m^2$ pixel pitch if the hit is predicted on the sensor surface with an accu-

racy of $9 \mu\text{m}$. Folding this probability with the measured efficiency as a function of the track hit position allows to correct acceptance edge effects in our efficiency measurements. From this calculation the systematic uncertainty of the efficiency calculation is also extracted, which is shown in figure 7.14b. The uncertainty is estimated by varying the telescope resolution up and down by $1 \mu\text{m}$. The error in the efficiency measurement due to the telescope resolution and alignment accuracy is minimised if the measurement area is restricted to the area highlighted in fig. 7.14c. The area defined through the four pixels centre as illustrated by the green area of figure 7.14c is also a representative area for the full pixel because it includes collection electrodes (center) as well as pixel boundaries and corners.

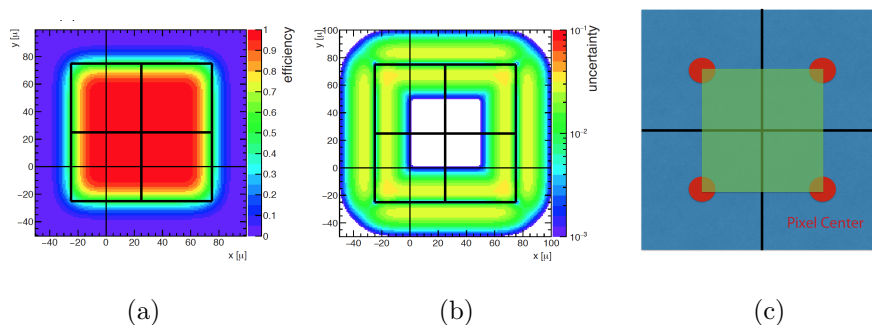
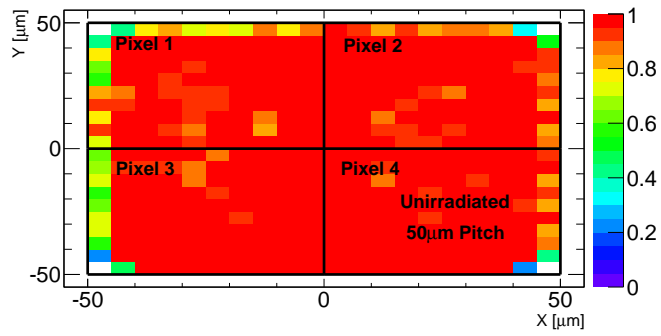


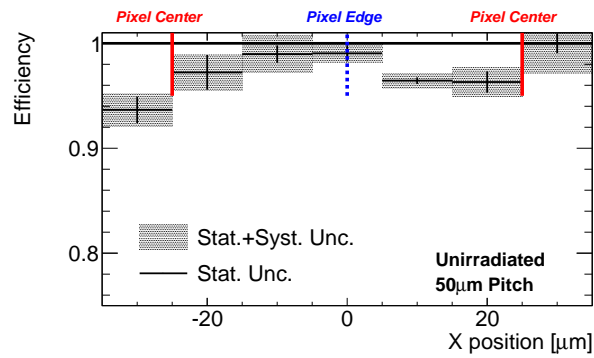
Figure 7.14: (a) Calculated detector efficiency as function of the hit position. (b) Calculated efficiency uncertainty using the telescope resolution of $\simeq 9 \mu\text{m}$. (c) Selection area for efficiency calculation.

The efficiency is calculated as a function of extrapolated hit position in x/y coordinates. This way the efficiency uniformity across the pixel can be visualised. The efficiency is defined as the ratio of the number of events with telescope tracks and a corresponding hit on the DUT to the number of all events with a telescope track. In fig. 7.15, 7.16, 7.17, 7.18 the hit efficiency is shown versus the x and y-position of the track relative to the aligned sensor position. Figure 7.15 shows the acceptance corrected efficiency as measured on an unirradiated $50 \times 50 \mu\text{m}^2$ pixel matrix with $3 \mu\text{m}$ electrode and $18.5 \mu\text{m}$ spacing. The efficiency is shown across the 4-pixel area (a) and the projection onto the X (b) and Y (c) directions.

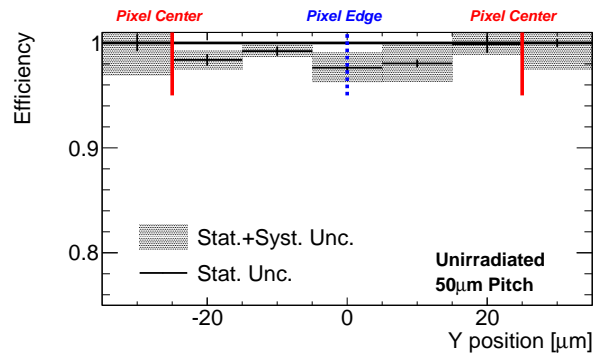
The efficiency is uniform across the pixel and it averages at $98.5\% \pm 0.5\%$ (stat) $\pm 0.5\%$ (syst) overall. The overall efficiency is limited to slightly less than 100% because of the rather high signal threshold (on this sensor), which was required to cope with high noise in the test beam setup due to common mode noise during the measurements of this sensor matrix.



(a)



(b)



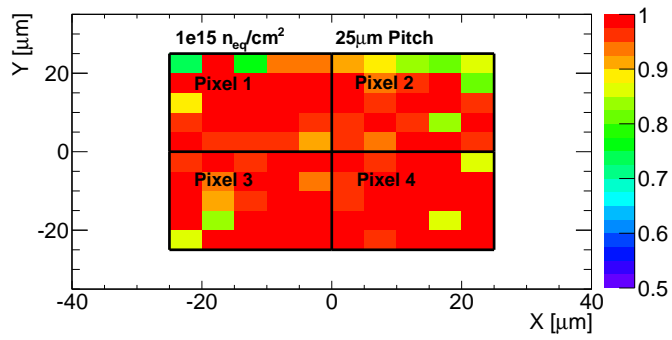
(c)

Figure 7.15: (a) 2-D detection efficiency, with projections on the (b) X and (c) Y directions of the $50 \times 50 \mu m^2$ sub-matrix of an unirradiated Investigator sample.

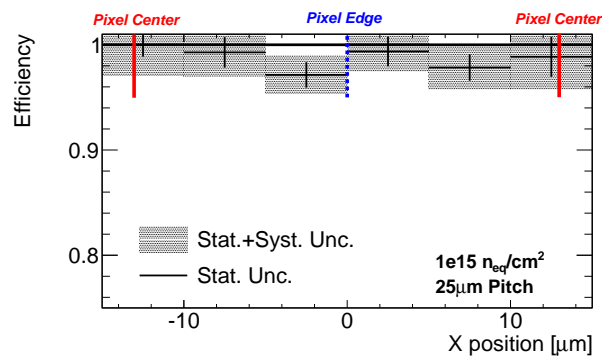
The irradiated samples with 25 and 30 μm pixel pitch and 3 μm spacing are fully efficient across the sensor. The overall efficiency integrated over the pixel cell

area was found to be $98.5\% \pm 1.5\%$ (stat) $\pm 1.2\%$ (syst) and $97.4\% \pm 1.5\%$ (stat) $\pm 0.6\%$ (syst) respectively.

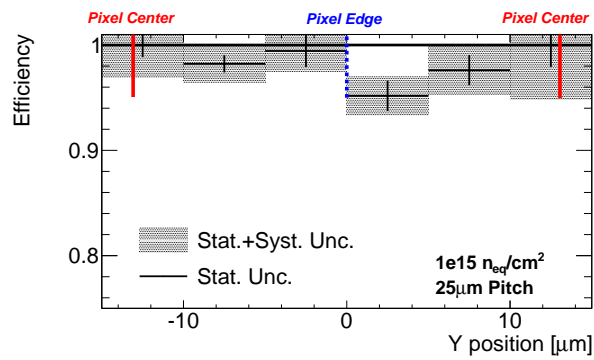
In conclusion the matrix with pixel pitch of $25 \times 25 \mu\text{m}^2$ shows the best efficiency and therefore such a pixel size is favoured in the development of a TowerJazz fully monolithic module.



(a)

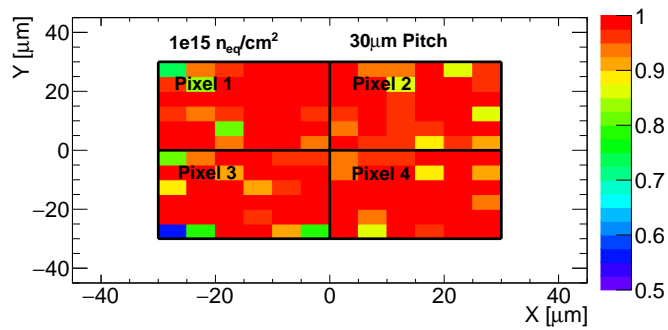


(b)

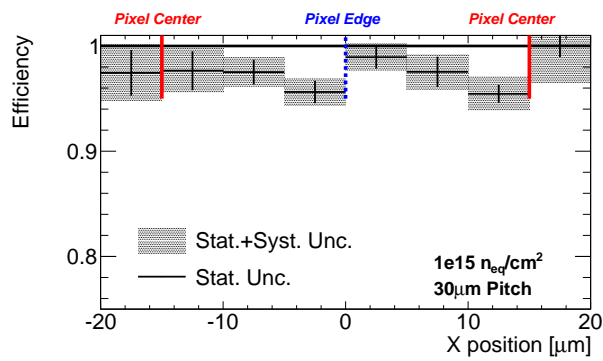


(c)

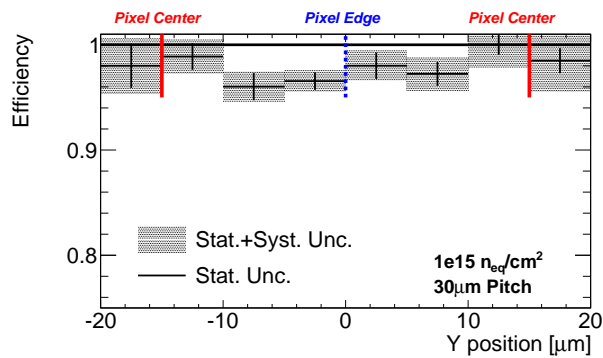
Figure 7.16: (a) 2-D detection efficiency, with projections on the (b) X and (c) Y directions of the 25x25 μm^2 sub-matrix of an irradiated Investigator sample.



(a)



(b)

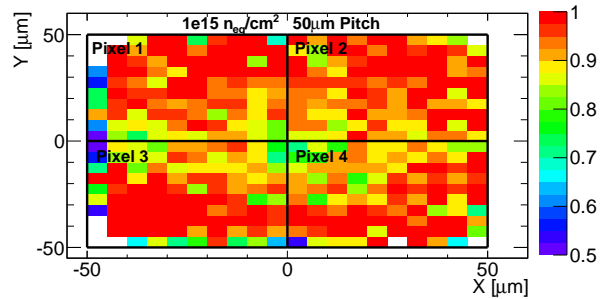


(c)

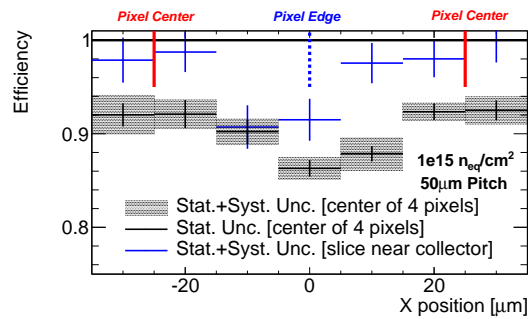
Figure 7.17: (a) 2-D detection efficiency, with projections on the (b) X and (c) Y directions of the $30 \times 30 \mu\text{m}^2$ sub-matrix of an irradiated Investigator sample.

The irradiated sample with $50 \mu\text{m}$ pixel pitch, $3 \mu\text{m}$ electrode and $18.5 \mu\text{m}$ spacing shows a non negligible decrease of efficiency at the edges of the pixel. This

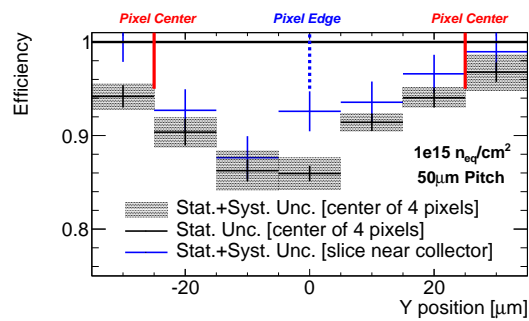
is probably due to the long rise time of the signals at the edges.



(a)



(b)



(c)

Figure 7.18: (a) 2-D detection efficiency, with projections on the (b) X and (c) Y directions of the 50x50 μm^2 sub-matrix of an irradiated Investigator sample.

7.4 Measurements with radioactive sources

Measurements in the Pixel Laboratory were done using two radioactive sources: ^{55}Fe and ^{90}Sr . The X-rays from the ^{55}Fe source are used for calibration purposes, while ^{90}Sr is used as a source of ionising particles (MIPs) similar to the ones in the test beam facilities. X-rays and MIPs generate charges in the sensor via different means: while X-rays are absorbed in point-like regions by photoelectric conversion, MIPs ionise approximately uniformly the atoms along their path generating electron-hole (e-h) pairs on their way.

The investigator was positioned inside a climate chamber at the temperature of -30°C in order to keep the leakage current of the irradiated sensor under control. The sources were positioned on top of the DUT, which had the configuration explained in the previous section. The trigger depended on the Investigator itself with self-trigger on one channel. The waveform obtained were recorded and analysed as previously described. Both the unirradiated and the $10^{15}n_{eq}/\text{cm}^2$ irradiated samples were used, considering only a matrix with $50\times 50\ \mu\text{m}^2$ pixel sensor, $3\ \mu\text{m}$ electrode and $18.5\ \mu\text{m}$ spacing.

7.4.1 ^{55}Fe source: charge calibration

A single-pixel ^{55}Fe spectrum obtained from measurements of matrices with pixel pitch of $50\times 50\ \mu\text{m}^2$ and collection electrode of $3\ \mu\text{m}$ is shown in figure 7.19. The plot shows both the spectra for an irradiated sample and a “new” one. The matrices were biased with a voltage of -6V . The peak of ^{55}Fe is clearly visible. Signals having a lower amplitude are assumed to originate from events where the charge was shared with neighbouring pixels. The comparison between the irradiated and unirradiated samples shows a significant reduction in gain after irradiation, although a clearly distinct peak can still be seen after this level of irradiation ($10^{15}n_{eq}/\text{cm}^2$).

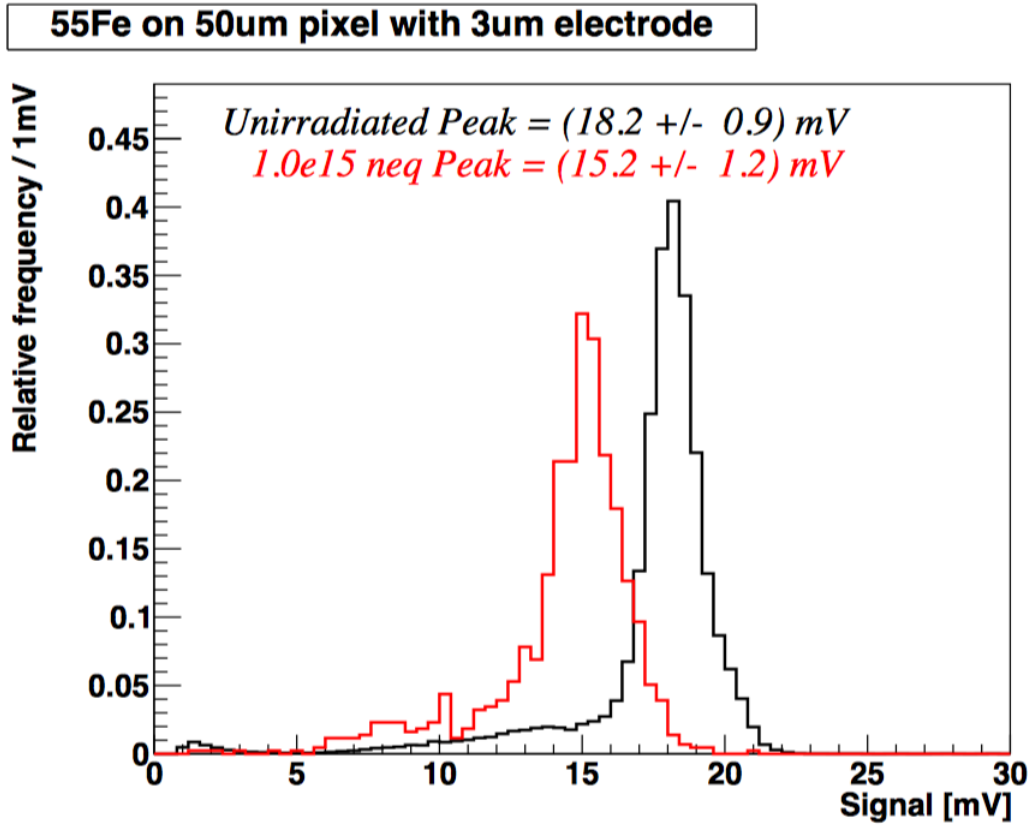


Figure 7.19: Single pixel spectra obtained from the source measurements using a ^{55}Fe source on the $50 \times 50 \mu\text{m}^2$ sub-matrix of both an irradiated and unirradiated Investigator sample.

7.4.2 ^{90}Sr source

Measurements are repeated using a ^{90}Sr source in order to obtain the spectrum of a MIP. The waveform are recorded and analysed in the same way as before. The ^{90}Sr spectra are converted from mV into number-of-electrons using the peak position of ^{55}Fe calibration, under the assumption that 1650 e^- are created in the peak. The spectra are showed in figure 7.20. The most probable values (MPVs) of the Landau distributions are lower than the expected value of 2000 e^- for a vertically fully depleted $25 \mu\text{m}$ thick epitaxial layer. This effect is probably due to imperfections in the sensor substrates and needs to be further investigated.

The MPV position of the irradiated sample is slightly higher than the one of the unirradiated sample. Behaviours like this had been observed for substrates of lower resistivity as well as substrates with resistivity in a comparable range of the TowerJazz investigator chip ($k\Omega\cdot\text{cm}$). While the detection efficiencies for the irradiated sensors are not precluded since the peak in the spectra are clearly distinguishable, a further calibration is necessary for a measure of dE/dx .

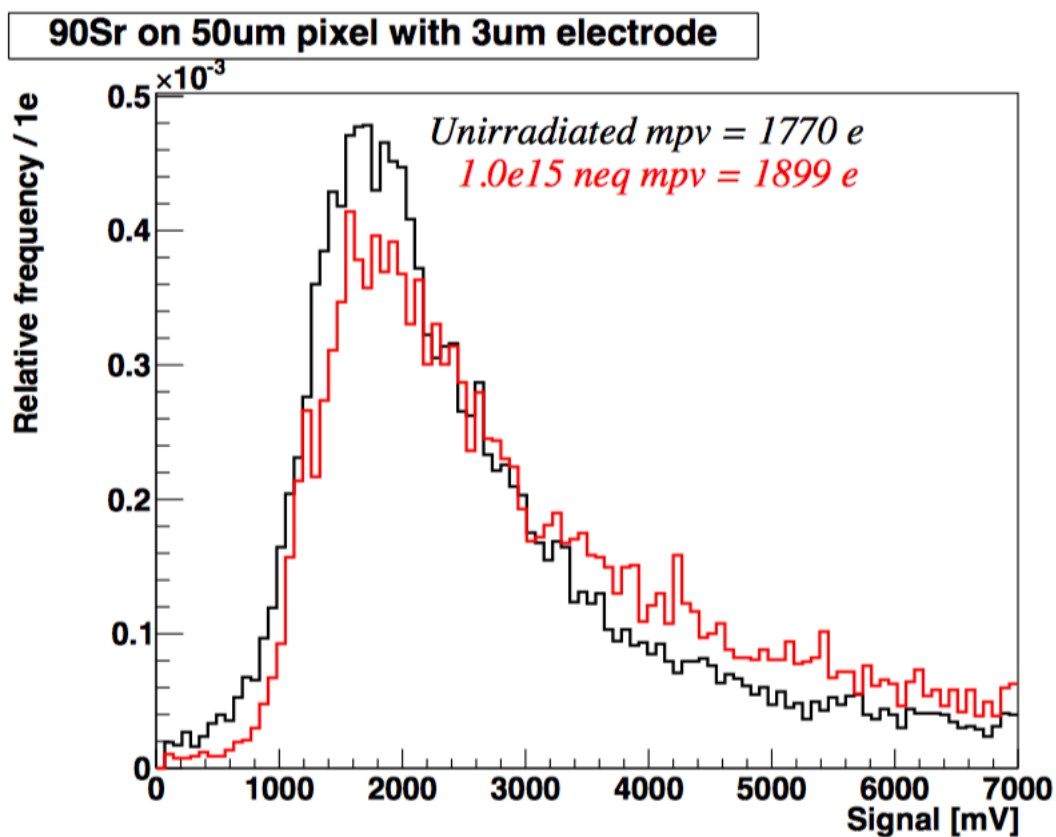


Figure 7.20: Single pixel spectra obtained for the source measurements using a ^{90}Sr source on the $50\times 50\ \mu\text{m}^2$ sub-matrix of both an irradiated and unirradiated Investigator sample.

Chapter 8

Conclusions

The measurements presented in this thesis can be used to verify the suitability of BCD8 and TowerJazz technologies for fully monolithic detectors for the outer layer of the ATLAS Inner Tracker to be implemented for HL-LHC. The BCD8 technology allows to build sensors with integrated electronics on the same substrate that can be capacitively coupled with front-end readout chips. The TowerJazz technology is certainly more interesting and promising for the future of Atlas ITk, since it allows to build a fully monolithic pixel detector that has the advantage of a reduced thickness and an easier and quicker production process, albeit further developments are needed to reach a fully functioning prototype that can withstand the radiation levels of HL-LHC.

The tests on the BCD8 KC53AB prototype passive pixels demonstrate that the pixel design can be used for particle detection. In particular the current-voltage (IV) measurements show that the reverse current is few orders of magnitude smaller than the expected signal from a MIP. The capacity-voltage (CV) measurements show that the depletion depth is in full agreement with expectations. However, measurements done on one sample irradiated with a dose approximately 3 times in excess of that expected for the outer layer of ITk, manifest the need for further investigations since the substrate showed possible damages and thus reduced performance after irradiation. New measurements on a second prototype in BCD8 technology, called KE15A, are being performed right now.

The measurements performed on the TowerJazz Investigator samples show that these prototypes are extremely efficient, collect the charge generated by ionising particles very effectively and, most important, are very fast. Thus they can be used at the very high rate of particles expected for outer layer of ATLAS ITk. These measurements will provide a useful input for the designers to choose the best geometrical parameters of the pixels as well as optimise the electronics integrated on the chip.

The results of the measurements performed in this thesis on BCD8 and TowerJazz technologies will contribute to the evolution and optimisation of tracking detectors, especially the ones that will be installed in the new tracker of ATLAS, and also show a big margin for the improvement of these technologies.

Bibliography

- [1] “A process modification for CMOS monolithic active pixel sensors for enhanced depletion, timing performance and radiation tolerance”. In: *Nuclear Instruments and Methods in Physics Research Section A: Accelerators, Spectrometers, Detectors and Associated Equipment* 871 (2017), p. 90. URL: <http://dx.doi.org/10.1016/j.nima.2017.07.046>.
- [2] A. Airapetian et al. *ATLAS detector and physics performance: Technical Design Report, 2*. Technical Design Report ATLAS. Geneva: CERN, 1999. URL: <https://cds.cern.ch/record/391177>.
- [3] I. Antcheva et al. “ROOT — A C++ framework for petabyte data storage, statistical analysis and visualization”. In: *Computer Physics Communications* 180.12 (2009). 40 YEARS OF CPC: A celebratory issue focused on quality software for high performance, grid and novel computing architectures, pp. 2499 –2512. ISSN: 0010-4655. DOI: <https://doi.org/10.1016/j.cpc.2009.08.005>. URL: <http://www.sciencedirect.com/science/article/pii/S0010465509002550>.
- [4] G Apollinari et al. *High-Luminosity Large Hadron Collider (HL-LHC): Preliminary Design Report*. CERN Yellow Reports: Monographs. Geneva: CERN, 2015. URL: <https://cds.cern.ch/record/2116337>.
- [5] Collaboration ATLAS. *Letter of Intent for the Phase-II Upgrade of the ATLAS Experiment*. Tech. rep. CERN-LHCC-2012-022. LHCC-I-023. Draft version for comments. Geneva: CERN, 2012. URL: <https://cds.cern.ch/record/1502664>.

- [6] I. Berdalovic et al. “Monolithic pixel development in TowerJazz 180 nm CMOS for the outer pixel layers in the ATLAS experiment”. In: *Journal of Instrumentation* 13.01 (2018), p. C01023. URL: <http://stacks.iop.org/1748-0221/13/i=01/a=C01023>.
- [7] Oliver S. Bruning et al. “LHC Design Report Vol.1: The LHC Main Ring”. In: (2004).
- [8] Erik Butz. “Calibration, alignment and long-term performance of the CMS silicon tracking detector”. PhD thesis. Hamburg U., 2009. DOI: 10.3204/DESY-THESIS-2009-008. URL: <http://inspirehep.net/record/818044/files/desy-thesis-09-008.pdf>.
- [9] ATLAS Collaboration. *Technical Design Report for the ATLAS Inner Tracker Strip Detector*. Tech. rep. CERN-LHCC-2017-005. ATLAS-TDR-025. Geneva: CERN, 2017. URL: <https://cds.cern.ch/record/2257755>.
- [10] The ATLAS Collaboration et al. “The ATLAS Experiment at the CERN Large Hadron Collider”. In: *Journal of Instrumentation* 3.08 (2008), S08003. URL: <http://stacks.iop.org/1748-0221/3/i=08/a=S08003>.
- [11] A Ferrari et al. *FLUKA: A multi-particle transport code (program version 2005)*. CERN Yellow Reports: Monographs. Geneva: CERN, 2005. URL: <https://cds.cern.ch/record/898301>.
- [12] M. Garcia-Sciveres et al. “The FE-I4 pixel readout integrated circuit”. In: *Nuclear Instruments and Methods in Physics Research Section A: Accelerators, Spectrometers, Detectors and Associated Equipment* 636.1 (2011), S155–S159. ISSN: 0168-9002. DOI: 10.1016/j.nima.2010.04.101. URL: <http://dx.doi.org/10.1016/j.nima.2010.04.101>.
- [13] William R. Leo. “Techniques for Nuclear and Particle Physics Experiments”. In: (1994). DOI: 10.1007/978-3-642-57920-2. URL: <http://dx.doi.org/10.1007/978-3-642-57920-2>.

- [14] Garrin McGoldrick, Matevz Cery, and Andrej Gorisek. “Synchronized analysis of testbeam data with the Judith software”. In: *Nuclear Instruments and Methods in Physics Research Section A: Accelerators, Spectrometers, Detectors and Associated Equipment* 765 (2014), pp. 140–145. ISSN: 0168-9002. DOI: <https://doi.org/10.1016/j.nima.2014.05.033>. URL: <http://www.sciencedirect.com/science/article/pii/S016890021400552X>.
- [15] Stefano Passadore. *Study of Pixel Detectors in BCD (Bipolar-CMOS-DMOS) Technology*, University of Milan, 2015.
- [16] H. Pernegger et al. “First tests of a novel radiation hard CMOS sensor process for Depleted Monolithic Active Pixel Sensors”. In: *Journal of Instrumentation* 12.06 (2017), P06008. URL: <http://stacks.iop.org/1748-0221/12/i=06/a=P06008>.
- [17] L. Rossi et al. *Pixel Detectors: From Fundamentals to Applications*. Particle Acceleration and Detection. Springer Berlin Heidelberg, 2006. ISBN: 9783540283331. URL: <https://books.google.it/books?id=AKGIXQ0m0-EC>.
- [18] S. Terzo. “The Phase-II ATLAS ITk pixel upgrade”. In: *Journal of Instrumentation* 12.07 (2017), pp. C07023–C07023. ISSN: 1748-0221. DOI: 10.1088/1748-0221/12/07/c07023. URL: <http://dx.doi.org/10.1088/1748-0221/12/07/C07023>.
- [19] Ettore Zaffaroni. *Characterisation of a Pixel Detector in BCD8 Technology*. University of Milan, 2016.